

**Dynamic Trajectory-Based Couch Motion for Improvement of
Radiation Therapy Trajectories**

by

Robert Lee MacDonald

Submitted in partial fulfilment of the requirements
for the degree of Master of Science

at

Dalhousie University
Halifax, Nova Scotia
August 2014

© Copyright by Robert Lee MacDonald, 2014

TABLE OF CONTENTS

LIST OF TABLES	iv
LIST OF FIGURES	v
LIST OF ABBREVIATIONS USED	vii
ABSTRACT	viii
ACKNOWLEDGEMENTS	ix
CHAPTER 1 INTRODUCTION	1
1.1 Preface.....	1
1.2 Radiotherapy.....	1
1.2.1 Radiotherapy Techniques.....	3
1.2.1 Stereotactic Radiosurgery.....	5
1.3 Motivation.....	6
1.4 Specific Aims.....	8
1.4 Previous Work.....	9
CHAPTER 2 RADIATION PHYSICS	11
2.1 Introduction.....	11
2.2 Interactions of Photons with Matter.....	11
2.2.2 Photoelectric Effect.....	13
2.2.1 Compton Effect.....	14
2.2.3 Pair Production.....	15
2.3 Kerma and Absorbed Dose.....	16
2.3.1 Kerma.....	17
2.3.2 Absorbed Dose.....	18
2.4 Clinical Linear Accelerator.....	20
2.5 Dose Calculation Algorithms.....	26
2.6.1 Eclipse Treatment Planning Software and AAA.....	26
2.6.2 VMAT Optimization.....	29
CHAPTER 3 METHODS AND MATERIALS	32
3.1 Importing Anatomical Information.....	32
3.2 Calculation of Overlap.....	33
3.2.1 Mutual Plotting Method.....	35

3.3 Generation of Overlap Scoring Map.....	38
3.3.1 Geometric Overlap Score Equation.....	38
3.3.2 Collision Zones.....	43
3.4 Algorithm for Trajectory Navigation.....	45
3.4.1 Parameter Entry for Smoothing.....	46
3.4.2 Output Parameters.....	51
3.4.3 Restrictions for Import into Eclipse	52
3.5 Comparison of Conventional Trajectory to Optimized Trajectory.....	54
CHAPTER 4 RESULTS AND ANALYSIS	57
4.1 Sparing of Dose to OARs	57
4.2 Dose Homogeneity and Conformity to Target Volume.....	67
4.3 VMAT Optimization Effect on Dose Sparing.....	67
CHAPTER 5 DISCUSSION.....	72
5.1 Sparing of Dose to OARs	72
5.2 Comparison of Results to Yang et al.....	73
5.3 Dose Homogeneity and Conformity to Target Volume.....	75
5.4 VMAT Optimization Effect on Dose Sparing.....	76
CHAPTER 6 CONCLUSION AND FUTURE WORK	78
6.1 Conclusion.....	78
6.2 Future Work	79
BIBLIOGRAPHY.....	82
APPENDIX A Comparison of Dose Distributions.....	85

LIST OF TABLES

Table 3.1: Dose limitations for the most common OARs in cranial cancer cases.	43
Table 4.1: p -values for each of the maximum doses to OARs as calculated by the Wilcoxon rank sum test. N=30.	65
Table 4.2: p -values for each of the mean doses to OARs as calculated by the Wilcoxon rank-sum test. N=30.	66
Table 4.3: p -values for each of the maximum dose OARs as calculated by the Wilcoxon rank-sum test. N=20.	66
Table 4.4: p -values for each of the mean dose OARs as calculated by the Wilcoxon rank-sum test. N=20.	67
Table 4.5: Values for dose homogeneity and conformity indices for the optimized trajectory with the OAR sparing objectives removed.	70
Table 5.1: Average dose values for OARs compared to those available in Yang <i>et al</i> [1]. All dose values are in percent prescription dose.	74
Table 5.2: Average dose values for OARs compared to those available in Yang <i>et al</i> [1]. All dose values are in percent prescription dose normalized to the conventional dose.	75

LIST OF FIGURES

Figure 1.1: Normal tissue control probability and tumor control probability as a function of increasing dose. [3]	7
Figure 2.1: Relative importance of three major types of photon interaction [4].....	12
Figure 2.2 Kinematics of the photoelectric effect [5].....	13
Figure 2.3: Schematic diagram of Compton scattering. An incident photon with energy $h\nu$ interacts with a loosely bound (essentially free) atomic electron. The electron is ejected from the atom as a recoil (Compton) electron with kinetic energy E_K and a scattered photon with energy $h\nu' = h\nu - E_K$ is produced [4]	15
Figure 2.4 Diagram illustrating the production of annihilation radiation [5].....	16
Figure 2.5: Collision kerma and absorbed dose as a function of depth in a medium irradiated by a high-energy photon beam [4].	19
Figure 2.6: Schematic showing the rotational directions for the couch and gantry rotation [26].....	20
Figure 2.7 Anatomy of a modern linear accelerator [4].	22
Figure 2.8 Schematic of a beamlet in the AAA [14].....	29
Figure 3. 1: Projection of a volume onto a plane at isocentre. A line is drawn from the source position, based on rotational position of the gantry through each point making up the volume. The coordinate system described in the anatomy rotation is also pictured [16]	34
Figure 3.2: Diagram discussing the adjustment of all points to a 2D grid to establish similarly drawn points as an overlap. The grid spacing was 0.32mm.	37
Figure 3.3: Displaying the area projections of the PTV and an OAR (a) and their corresponding overlap (b).....	38
Figure 3.4: Overlap map between the PTV and the left eye.....	40
Figure 3.5: An overlap map with all OARs for the patient included. The large dark red regions indicate collision zones of the CG space.....	45
Figure 3.6: An overlay of the trajectory, indicated as yellow lines, designed by identifying the patient support and gantry positions that correspond to the minimum output from Equation 3.	46
Figure 3.7: Description of the two evaluations for design and smoothing of the trajectory.....	48
Figure 3.8: A visualization of the flexible threshold evaluation of the patient support position for suitability in the trajectory. x is the coordinate being evaluated bordered in white. $d3, d2, d1$ are user-assigned parameters for the gantry distance from x that the evaluation extends. $P1, P2, P3$ are values for the width the evaluation searches for neighboring couch positions with less overlap..	49
Figure 3.9: An example of the trajectory, indicated as yellow lines, after the absolute minimum coordinates have been reduced to include only positions within the user-specified evaluation criteria.	50

Figure 3.10: Visualization of the evaluation of nearby patient support positions with an improved overlap value for interpolated gantry coordinates. The dashed rectangle represents a former interpolated point. The point to its right is an adjusted coordinate.	50
Figure 3.11: An example of a completed treatment trajectory, indicated as yellow lines, overlaying the patient-specific overlap map.	51
Figure 3.12: Simplified trajectory indicated as yellow lines, with the maximum couch motion able to comply with the Eclipse restrictions on VMAT Optimization.	54
Figure 4.1 Mean dose reduction for a cranial test patient shown for both conventional and optimized trajectories.	59
Figure 4.2 Maximum dose reduction for cranial test patient shown for both conventional and optimized trajectories.	59
Figure 4.3 Mean dose reduction for entire patient population. The lack of error bar on the pituitary data is due to the fact that only one case had a contoured pituitary.	60
Figure 4.4 Maximum dose reduction for entire patient population (N = 30). The lack of error bar on the pituitary data is due to the fact that only one case had a contoured pituitary.	60
Figure 4.5 Average maximum dose across all OARs for all the plans in the patient set.	61
Figure 4.6 Mean dose reduction for subset of cases which were immediately successful during implementation of technique. (N=20)	63
Figure 4.7 Maximum dose for test-patient population subset of patients which were immediately successful upon implementation of technique.	63
Figure 4.8: Mean dose reduction for subset of cases which were worsened improved during implementation of technique. (N = 10)	64
Figure 4.9: Maximum dose reduction for subset of cases which were worsened during implementation of technique. (N = 10)	64
Figure 4.10: DVH for the right eye. Blue curve indicates the dose according to the optimized trajectory with 30° subarcs, red curve indicates conventional trajectory, and green curve is the same as the optimized trajectory, but with all VMAT dose sparing objectives removed.	69
Figure 4.11: DVH for the left eye. Blue curve indicates the dose according to the optimized trajectory with 30° subarcs, red curve indicates conventional trajectory, and green curve is the same as the optimized blue trajectory, but with all VMAT dose sparing objectives removed.	69
Figure 4.12: DVH for the PTV. Blue curve indicates the dose according to the optimized trajectory with 30° subarcs, red curve indicates conventional trajectory, and green curve is the same as the optimized trajectory, but with all VMAT dose sparing objectives removed.	70
Figure 4.13: Maximum dose values for all OARs in the patient structure set including the removal of the VMAT optimization organ sparing objectives. This data is for the same patient as shown in Figure 4.1.	71

LIST OF ABBREVIATIONS USED

3D-CRT	3-Dimensional Conformal Radiation Therapy
AAA	Anisotropic Analytical Algorithm
APBI	Accelerated Partial Breast Irradiation
BEV	Beam's Eye View
CI	Conformity Index
CG	Couch and Gantry Position
CT	Computed Tomography
DCA	Dynamic Conformal Arc
DICOM	Digital Imaging and Communications in Medicine
FFF	Flattening Filter Free
HI	Homogeneity Index
IMRT	Intensity Modulated Radiation Therapy
KERMA	Kinetic Energy Released in Matter
LINAC	Linear Accelerator
MLC	Multi-leaf Collimator
MU	Monitor Units
MV	Megavoltage
OAR	Organ-at-risk
PRO	Progressive Resolution Optimizer
PRV	Planning Organ-at-risk Volume
PTV	Planning Treatment Volume
QUANTEC	Quantitative Assessment of Normal Tissue Effects in the Clinic
RF	Radio Frequency
SRS	Stereotactic Radiosurgery
SRT	Stereotactic Radiotherapy
SSD	Source to Surface Distance
TCPE	Transient Charged Particle Equilibrium
VMAT	Volumetric Modulated Arc Therapy
Z	Atomic Number

ABSTRACT

This work investigates potential improvement in external beam radiation therapy plan quality using an optimized dynamic gantry and patient support couch motion trajectory, which could minimize exposure to sensitive healthy tissue. Anonymized patient anatomy and treatment plans of cranial cancer patients were used to quantify the geometric overlap between planning target volumes (PTVs) and organs-at-risk (OARs) based on their two-dimensional projection from source to a plane at isocentre as a function of gantry and couch angle. Published dose constraints were then used as weighting factors for the OARs to generate a map of couch-gantry coordinate space, indicating degree of overlap at each point in space. A couch-gantry collision space was generated by direct measurement on a linear accelerator and couch using an anthropomorphic solid-water phantom. A dynamic, fully customizable algorithm was written to generate a navigable ideal trajectory for the patient specific couch-gantry space. The advanced algorithm can be used to balance the implementation of absolute minimum values of overlap with the clinical practicality of large-scale couch motion and delivery time. Optimized cranial cancer treatment trajectories were compared to conventional treatment trajectories. Comparison of optimized treatment trajectories with conventional treatment trajectories indicates an average decrease in mean dose to the OARs of 19% and an average decrease in max dose to the OARs of 12%. Our study indicates that simultaneous couch and gantry motion during radiation therapy to minimize the geometrical overlap in the beams-eye-view of target volumes and the organs-at-risk can have an appreciable dose reduction to organs-at-risk.

ACKNOWLEDGEMENTS

Firstly, I would like to sincerely thank Dr. Christopher Thomas for his innovation, motivation, guidance, and leadership throughout the entire process of this research. Your patience and helpful guidance was a constant source of encouragement that was integral to completing this work. Your door was always open to me, for which I am very grateful. Thanks for all of your advice and many discussions on everything from heavy charged particles to heavy metal.

I would like to thank Dr. James Robar for the tremendous opportunity that he has provided me with in performing this research and for all of the experiences that it has encompassed. You have been a vital source of knowledge and expertise throughout this work.

Additionally I would like to thank everyone at the Nova Scotia Cancer Centre for all of your help and friendship over the last two years. I would especially like to thank Dr. Mike Sattarivand for all of his help with the completion of this thesis.

I would like to thank my fellow classmates: Cathryn Parsons, Shiqin Su and David Parsons. It's been a pleasure studying with you and I wish you all the very best. In particular I would like to thank Dave for the code to assist with volumetric projection.

I would like to thank all of my friends and family who are always supportive and caring. Lastly, and most importantly, thank you to Hannah.

CHAPTER 1 INTRODUCTION

1.1 Preface

In 2011, cancer caused 29.9% of deaths in Canada. It is the largest contributing factor to human death in Canada and it continues to rise. In 2014, it is estimated that there will be 191,300 new cases and 76,600 deaths caused by cancer [7]. As the incidence of cancers continues to rise, so too do the efforts designed to treat and cure disease. New techniques can provide added efficacy of treatments in both local and systemic treatment of cancer. Systemic treatments, like chemotherapy, involve the introduction of disease killing substances, focussing on uptake primarily in disease site. Local treatments include surgery, brachytherapy and external beam radiotherapy. Internal radiation therapy (brachytherapy) involves the insertion or implantation of radiation sources at or near to the target volume while external beam radiation therapy involves the delivery of radiation from an external source, which tailors the dose delivery to accumulate in the site of disease. The effective treatment of cancerous tissue with the protection of healthy tissue allows for a decrease in the probability of recurrence of disease and increased probability of maintaining normal function of any surrounding sensitive organs.

1.2 History of Radiotherapy

German physics professor Wilhelm Roentgen discovered X-rays in 1895. His lecture “Concerning a New Type of Ray” was the first indication of an entire new field of study. When it was discovered that these X-rays were capable of damaging tissue, Emil Grubbe, a physician in Chicago, became the first to use radiation to treat cancer in 1896 [17]. Grubbe used this new technique to treat a patient with recurrent carcinoma of the breast. Within three years, doctors in Sweden were using radiotherapy to treat multiple

cases of cancer in the head and neck region. In 1901, Roentgen was awarded the Nobel Prize in Physics for his discovery [17].

In 1922, the concept of the delivery of smaller doses of ‘fractionated’ radiotherapy to achieve a more effective treatment with fewer side effects was shown by Cladius Regaud. Also in the 1920s, radiography emerged and radiotherapy was largely used to treat symptoms in a palliative way, rather than a curative method. At this time the X-ray generators were only capable of produced approximately 200 kV beams [17].

The development of the ^{60}Co teletherapy unit by H.E. Johns in 1949 at the University of Saskatchewan in Canada was a milestone in treatment using high-energy photon beams (average energy 1.25 MeV). The first patient was treated in 1951 at the Victoria Hospital in London, Ontario. By 1961, cobalt therapy was widely implemented and the cobalt unit remained in use for a number of years until it was superseded following the development of versatile and compact modern linear accelerators which have the ability to treat with both electrons and megavoltage photons.

Medical linear accelerators (linacs) accelerate electrons to kinetic energies from 4 to 25 MeV using non-conservative microwave RF fields. Linacs have gone through five distinct generations [4]:

- Low energy photons (4-8 MV): straight through beam; fixed flattening filter; external wedges; symmetric jaws; single transmission ionization chamber; isocentric mounting; magnetrons as microwave power sources [27]
- Medium energy photons (10-15 MV) and electrons: bent beam; movable target and flattening filter, scattering foils; dual transmission ionization

chamber; electron cones; klystrons as microwave power sources; standing waveguide [27].

- High-energy photons (18-25 MV) and electrons: dual photon energy and multiple electron energies; achromatic bending magnet; dual scattering foils or scanned electron pencil beam; motorized wedge; asymmetric or independent collimator jaws.
- High-energy photons and electrons: computer controlled operation; dynamic wedge; electronic portal imaging device (EPID); multileaf collimator (MLC).
- High-energy photons and electrons: photon beam intensity modulation with MLC; full dynamic conformal dose delivery with intensity modulated beams produced with an MLC. Additionally, synchrony is introduced between the dose rate, gantry angle, and MLC aperture [4].

Modern linear accelerators offer a wide variety of treatment energies and mechanical collimation devices capable of treating a variety of flexible dynamic plans which can be custom-tailored according to each patient. The current objectives of radiotherapy are to ensure coverage of the target volume to a high dose of radiation, while limiting the dose to healthy normal tissues, sparing any sensitive structures from radiation exposure. The aim is to damage cancerous cells and prevent their regrowth.

1.2.1 Radiotherapy Techniques

Several different radiotherapy techniques currently exist for treatment, each with varying strengths to treat all varieties of cancer diagnosis. These techniques differ with the degree of complexity associated with their design and capacity to deposit dose. One

of the most common types of external beam radiation therapy is three-dimensional conformal radiation therapy (3D-CRT) which uses computer software and advanced treatment machines to deliver precisely shaped target areas. 3D-CRT involves multiple static beam delivery.

An additional method is intensity modulated radiation therapy (IMRT) which uses discrete beams at fixed gantry positions with hundreds of small beam shaping leaves called multi-leaf collimators (MLC) defining the aperture for each beam. IMRT uses inverse planning in which the radiation doses to tumors and surrounding tissues are defined and then treatment is planned around delivering these doses. IMRT aims to increase the dose to target areas and reduce exposure to sensitive areas of healthy tissue. IMRT reduces the risk of dose to sensitive normal tissues in complex planning cases such as head-and-neck and cranial cancer patients as compared to 3D-CRT [25].

Volumetric modulated arc therapy (VMAT) is the delivery of hundreds of IMRT apertures dynamically in a continuous motion (*See section 2.6.2*). An entire treatment composed of independent IMRT fields can be condensed to be delivered in a single gantry rotation. However, frequently the treatment is delivered in two to four continuous gantry motions, or arcs. VMAT uses a unique optimization in order to define the doses to normal tissues in addition to the criteria for target coverage. This optimization produces the MLC configuration for each position within the delivered plan, the gantry rotation speed and the dose modulation based on the objectives established by the user prior to optimization. The couch position for standard VMAT treatments is usually fixed throughout treatment at 0° . This is defined as coplanar VMAT delivery. Some specialization of VMAT includes stereotactic radiosurgery (SRS).

1.2.2 Stereotactic Radiosurgery

The first implementation of SRS was with the development of the gamma knife by surgeon Lars Leksell of Sweden. The gamma knife is a radiotherapy treatment device that administers high-intensity cobalt radiation to concentrate dose to a small region [18]. This was the first effort to treat intracranial lesions noninvasively. His goal was to develop a method for the “intracranial lesions that may be inaccessible or unsuitable for open surgery”[18]. The term stereotactic indicates the use of a three-dimensional coordinate system to arrange the target seen in patient images and the anatomical location of the target.

SRS is a radiation therapy procedure delivered in one fraction for treating sites such as the brain, spine, lung, liver, and pancreas using a combination of a stereotactic apparatus and narrow multiple beams delivered through isocentric arcs or over a number of fixed beams [6]. SRS techniques are most commonly implemented to treat metastases, gliomas, meningiomas, schwannomas, neuromas, pituitary tumors, and pediatric tumors among others [18].

By about 1990, several groups began to consider the potential biological advantages of fractionated SRS, a multi-fraction delivery method called stereotactic radiotherapy (SRT). This type of treatment has increased steadily over the past 15 years and is the principle method for treating malignant tumors, benign tumors and vascular disorders [18]. A high radiation dose conformity is one characteristic of SRT and SRS and this is achieved by using small beams of radiation fit to the shape of the lesion, either with stereotactic cones or high-definition MLCs, optimized arc angles and weights, or the use of multiple isocentres. A stereotactic apparatus, called a frame, is sometimes used

during imaging, target localization, head immobilization, and treatment setup, although frameless SRT/SRS is becoming more widely used. Frame-based SRS uses a frame which is affixed to the patient's skull using pins and provides a rigid coordinate system for targeting of the tumor, while frameless SRS/SRT forgoes the frame and relies on image-guidance during treatment to confirm the location of the tumor.

1.3 Motivation

Nova Scotia Cancer Centre (NSCC) has access to some of the most advanced radiotherapy systems available in a clinical setting. One of these systems is a software package which allows for the experimental implementation of unconventional treatment trajectories, one of which includes simultaneous rotation of couch and gantry. In conventional treatment the couch always remains in a fixed position for the duration of gantry motion.

To further advance currently available radiotherapy techniques means to improve upon the objectives with which they were designed. Some of these objectives include ensuring the target volume is receiving the proper coverage, and that the healthy tissue within the region of delivery is not harmed. Normal tissue complications hold a well-defined relationship with the absorbed dose of radiation. With increasing radiation dose, radiation effects in normal tissues increase in severity, frequency, or both. The dose response curve for normal tissue has a sigmoid shape (See *Figure 1.1*), indicating a tendency towards zero for a dose of zero, and nearing 100% for very large doses. The radiosensitivity of a tissue is dependent on the kinetics of the tissue, the cell population and the way cells are organized within the tissue [3]. Not all healthy tissue structures have set limits of a maximum threshold value of dose to the structure. Some sensitive

organs are assigned a constraining mean absorbed dose limit to the entire structure and/or a dose volume constraint as their symptomatic probability of occurrence. TD5/5 is a probability of the dose that is likely to cause the radiation exposure effect in 5% of the population, five years after treatment. Effects such as this seen in a time frame after six months of treatment are late reactions (spinal cord injury, fibrosis, fistulas etc.) while effects seen within three months of treatment are acute reactions (erythema, nausea, vomiting etc.). It is important to note that tumor control probability also has a sigmoid shape (see *Figure 1.1*) and there is always a trade-off between tumor control and normal tissue sparing.

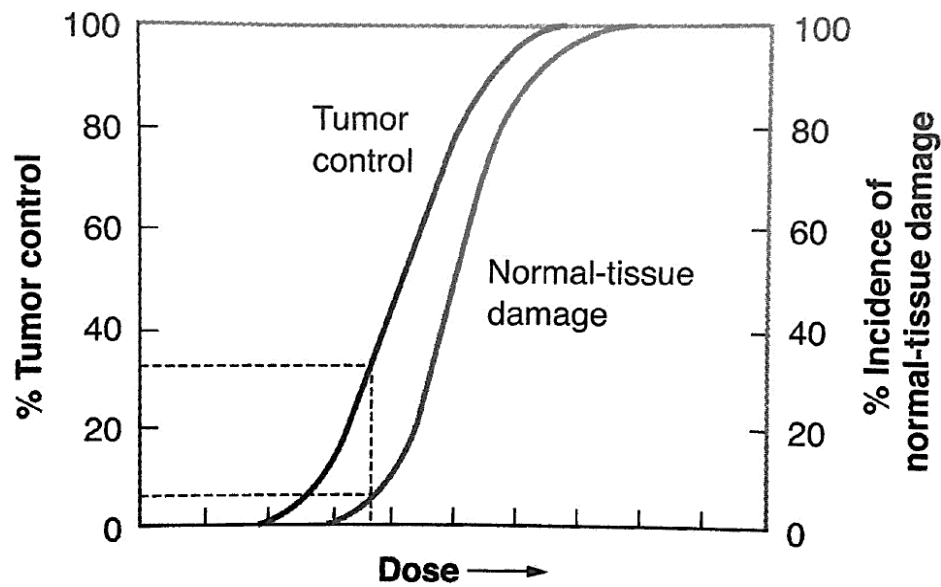


Figure 1.1: Normal tissue control probability and tumor control probability as a function of increasing dose [3].

Additionally, the effects in some sensitive tissues are responsive to different types of damage. Serial organs, such as the spine, are arranged such that they are dependent on the function of subsections within the organ. In these organs, even a small volume irradiated over a threshold can lead to full organ failure. Contrarily, parallel organs, like lungs, can lose subsections of the organ and still retain full organ function.

With the advanced technologies at our disposal at the NSCC, a novel technique is needed which can further reduce doses to healthy tissues while maintaining treatment of disease in SRT cranial treatments. Previous studies [1, 8, 10] have shown promising effects in normal tissue sparing with the implementation of added couch motion. This improvement is introduced through the added ability to treat in dynamic planes (non-coplanar) to allow for geometric avoidance of critical structures.

1.4 Specific Aims

Our research is an investigation of rotational patient support motion, without motion along the longitudinal axis, with the aim of improving the efficacy of radiotherapy, specifically for SRT treatment of intracranial lesions, by minimizing dose to critical structures surrounding the target volume via design of treatment trajectories (defined by simultaneous gantry and couch motion). A key requirement for a technique to be implemented clinically is to be complimentary to the existing established treatment planning process and to this end should interface with the current treatment planning software widely used clinically. Newly developed software capabilities of the linear accelerators, which promote the investigation of novel treatment techniques, enable the ability to treat with simultaneous couch and gantry motion. To create utilization for this new capability, we aim to develop an algorithm capable of designing a patient-specific couch trajectory to minimize dose to OARs without affecting the delivery of the prescribed dose to the PTV.

SRT is chosen because the conventional treatment technique already involves the use of non-coplanar arcs and maximizes the range of motion for full 4π approach of treatment beams. The position of the patient support couch and gantry is identified by a procedure initially proposed by Yang *et al* [1] for use in conjunction with their in-house

VMAT optimization algorithm. Regions of minimum overlap between the planned target volume and all of the radiosensitive organs potentially at risk of exposure are identified. Using overlap maps that are unique to each calculated test patient gives an indication of the amount of overlap present in each valid coordinate represented by a gantry and couch position (CG coordinate). Our novel algorithm is then designed to find the most efficient path to traverse the overlap map in one full (360°) gantry rotation. Algorithms are vital to the process of designing a trajectory as smooth pathways which minimize overlap and generate dynamic flexible paths cannot be feasibly produced manually for treatment planning. The algorithm takes into account clinical priorities including time of delivery and range of motion for the patient support system. The end result being couch-gantry trajectories for radiotherapy plans.

These plans are then VMAT optimized and compared to the previously clinically delivered conventional trajectory VMAT plans. The dose calculation and VMAT optimization are performed by Eclipse Treatment Planning Software (Varian Medical Systems, Inc., Palo Alto, USA). In addition to sensitive tissue dose sparing, the plans are evaluated for homogeneity and conformity of dose to the intended target volume (PTV).

The aim is to produce radiotherapy treatment plans which are clinically viable, adaptable to the priorities of the planner, and optimized to protect the patient from unneeded dose to sensitive healthy tissue, while maintaining coverage of the target for successful treatment of the disease.

1.5 Previous Work

The investigation of simultaneous couch and gantry radiotherapy is currently a very active field of research. Several recent publications have illustrated principles and

methods. Yang *et al* [1] have supplied the motivation for this research in the creation of a cost function analysis of the patient anatomy, which produces an overlap map as a guide for designing a patient support system and gantry trajectory. However, they calculated their trajectories for use with their in-house dose treatment planning system. Similarly, Smyth *et al* [8] rely on different trajectory optimization algorithms and their own in-house treatment planning software that is not widely available. Additionally, their cost function relies on the depth of healthy tissue between the source and the target volume. Shatelman *et al* [12] and Fahimian *et al* [10] have presented work on accelerated partial breast irradiation (APBI) therapy with significant success in dose sparing. These studies rely on different trajectory optimization algorithms, and do not consider organs-at-risk in their optimization. Shatelman *et al* [12] presents a rotating couch for partial-breast irradiation, however, the gantry remains in a fixed position throughout treatment. Popescu *et al* [11] also presents a method for partial-breast irradiation with two subarcs of simultaneous couch and gantry motion that was selected based on trial-and-error. Rodrigues *et al* [9] have presented an electron arc radiotherapy combining gantry and couch motion. A previous patent by Van Heteran *et al* [13] involves the rotation of the couch along a longitudinal axis, which includes no means for selection of couch position.

CHAPTER 2 RADIATION PHYSICS

2.1 Introduction

This chapter introduces the physics concepts necessary for understanding the methods conducted throughout the rest of the work. All treatment plans analyzed in this work were designed with a beam of photons delivered via a linear accelerator. The interactions for photon beams are described in *Section 2.2* to assist in the comprehension of how the energy from this beam of photons is transferred to directly ionizing charged radiation. *Section 2.3* is included to show how the metrics are established to define the transfer of energy from indirectly ionizing radiation to directly ionizing radiation and for dose deposited to tissues. *Section 2.4* is designed to outline the physical construction and function of the linear accelerator to provide clarity on beam production and mechanisms of beam delivery. *Section 2.5* describes the software models used to predict dose delivered during the design and calculation of radiotherapy patient plans.

2.2 Interactions of Photons with Matter

Ionizing photons can be divided into four categories based on their origin [4]:

- Bremsstrahlung photons that are continuously produced X-rays emitted through electron-nucleus interactions.
- Characteristic X-rays discretely produced in transitions of orbital electrons from one orbit to a vacancy in another orbit.
- γ -rays discretely emitted through nuclear transitions in radioactive decay.
- Annihilation radiation emitted through positron-electron annihilation.

As photons pass through a medium, they have a certain probability of interactions with the atoms inside the medium. The most probable types of interactions in the

megavoltage range in tissues of the human body are the Compton effect, photoelectric effect and pair production. The relative importance of each of these interactions as a function of energy is displayed in *Figure 2.1*. Other forms of less-probable interaction include Rayleigh scattering, Thomson scattering, and photonuclear interaction, which play a much lesser role in the contribution of dose deposition in the megavoltage range.

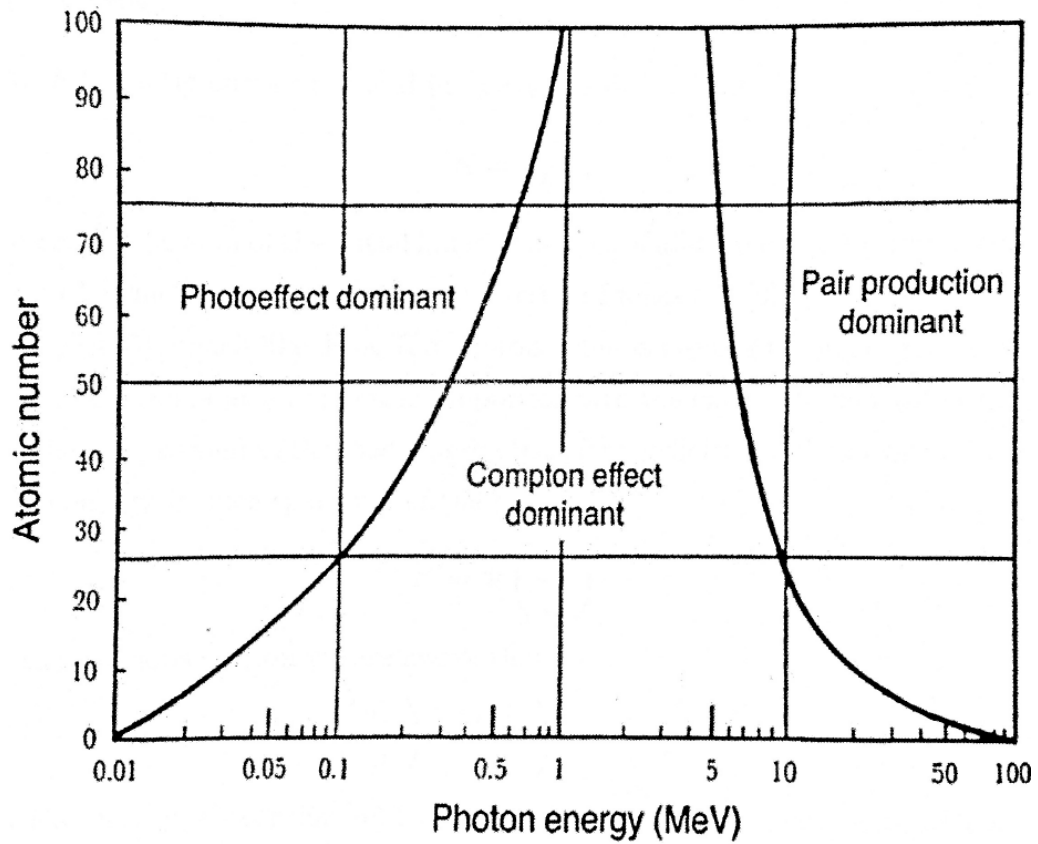


Figure 2.1: Relative importance of three major types of photon interaction [4].

2.2.2 Photoelectric Effect

The photoelectric effect is a phenomenon in which a photon interacts with an atom and ejects one of the orbital electrons from the atom (see *Figure 2.2*). In this process, the entire energy, $h\nu$, of the photon is transferred to the atomic electron. The orbital electron that is ejected from the atom as a photoelectron has a kinetic energy, $k.e.$, that is given as:

$$k.e. = h\nu - E_b \quad (2.1)$$

where E_b is the binding energy of the electron [4].

The interaction cross section per atom for photoelectric effect, integrated over all angles of photoelectron emission, can be written as:

$$a\tau \cong \frac{Z^n}{(h\nu)^m} \quad (2.2)$$

where Z is atomic number, with units of (cm^2/atom); $n = 4$ at $h\nu = 0.1$ MeV, gradually rising to about 4.6 at 3 MeV; $m = 3$ at $h\nu = 0.1$ MeV, gradually decreasing to about 1 at 5 MeV [5]. At an energy corresponding to the binding shell energy of the attenuating medium there is a discontinuity called an absorption edge. Photons of less than that of the absorption edge are unable to undergo the photoelectric effect with an electron in the orbital corresponding to that energy.

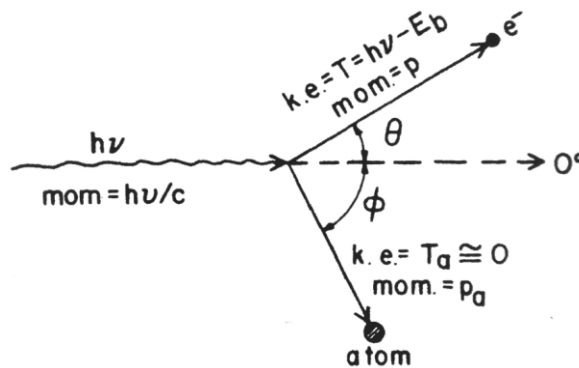


Figure 2.2: Kinematics of the photoelectric effect [5].

2.2.1 Compton Effect

In the Compton process, the photon interacts with an atomic electron as though it were a “free” electron. The term “free” means that the binding energy of the electron is much less than the energy of the incident photon with energy $h\nu$. The photon loses part of its energy to the recoil electron and is scattered as a photon with energy $h\nu'$ through a scattering angle of θ (refer to *Figure 2.3*) [4]. The electron is scattered at an angle of ϕ [6]. The change in photon wavelength is given by:

$$\Delta\lambda = \lambda_C(1 - \cos\theta) \quad (2.3)$$

where λ_C is the Compton wavelength of the electron, which can be expressed as:

$$\lambda_C = \frac{h}{m_e c} = 0.024\text{\AA} \quad (2.4)$$

The photon scattering angle, θ , and the recoil electron angle, ϕ , are then related by the equation:

$$\cot\phi = \left(1 + \frac{h\nu}{m_e c^2}\right) \tan\left(\frac{\theta}{2}\right) \quad (2.5)$$

From this equation, it is clear that the range of the angle ϕ is between 0 (at $\theta = \pi$) and $\pi/2$ (at $\theta=0$) for any arbitrary photon energy. For a given θ , the higher the incident photon energy, the smaller is the recoil electron angle, ϕ [4].

Since Compton interactions involve essentially free and stationary electrons ($h\nu \gg E_B$) the attenuation depends linearly on the atomic number, Z , of the attenuator. The

coefficient for atomic attenuation, ${}_a\sigma_C$, has a strict Z dependence while the electronic, ${}_e\sigma_C$, and mass Compton attenuation coefficients, σ_C/ρ , are independent of Z .

The energies of both the scattered photon, $h\nu'$, and the kinetic energy of the Compton electron, E_K , are given below:

$$h\nu' = h\nu \frac{1}{1 + \varepsilon(1 - \cos\theta)} \quad \text{and} \quad E_K = h\nu \frac{\varepsilon(1 - \cos\theta)}{1 + \varepsilon(1 - \cos\theta)} \quad (2.6)$$

where ε is $\frac{h\nu}{m_e c^2}$.

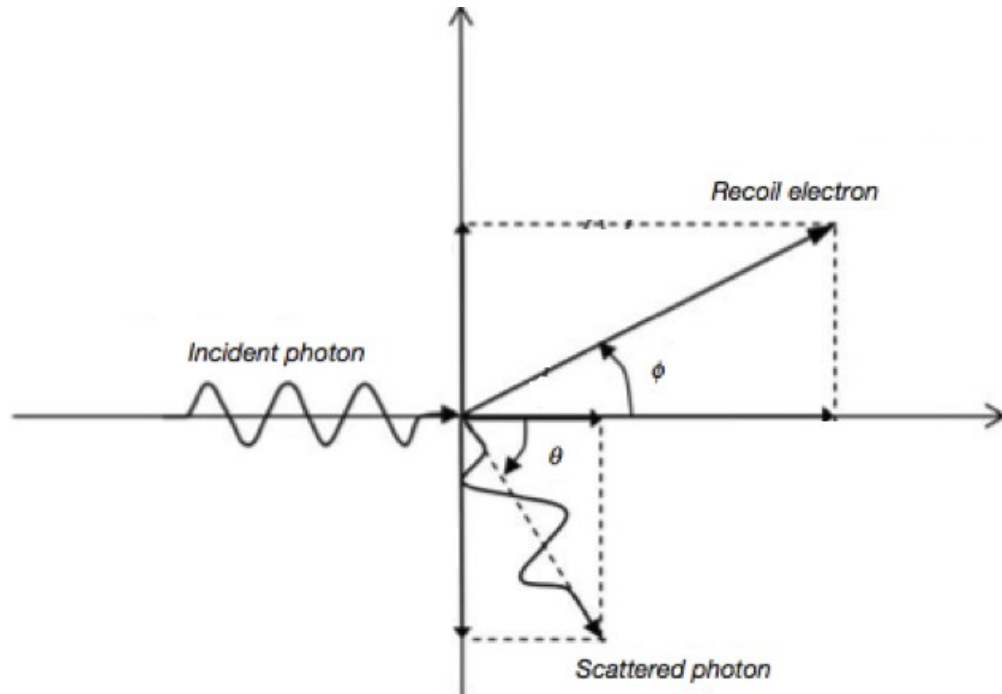


Figure 2.3: Schematic diagram of Compton scattering. An incident photon with energy $h\nu$ interacts with a loosely bound (essentially free) atomic electron. The electron is ejected from the atom as a recoil (Compton) electron with kinetic energy E_K and a scattered photon with energy $h\nu' = h\nu - E_K$ is produced. [4]

2.2.3 Pair Production

If the energy of the photon is greater than 1.02 MeV, the photon may interact with matter through the mechanism of pair production. In this process, the photon interacts

strongly with the electromagnetic field of an atomic nucleus and gives up all its energy in the process of creating a negative electron and positive electron (positron) (see *Figure 2.4*). Since the rest mass energy of the electron is equivalent to 0.51 MeV, a minimum energy of twice that is required to create the pair of particles. Thus the threshold energy for the pair production is 1.02 MeV. The photon energy in excess of this threshold is shared between the particles as kinetic energy. The total kinetic energy available for the electron-positron pair is given by $(h\nu - 1.02)$ MeV [6]. The positron then goes on to interact with a free electron in a process known as annihilation which yields photons equal to the value of the rest mass of each of the particles (see *Figure 2.4*). The atomic attenuation coefficient for pair production, ${}_a\kappa$, and the mass attenuation coefficient for pair production, κ/ρ , vary approximately as Z^2 and Z , respectively.

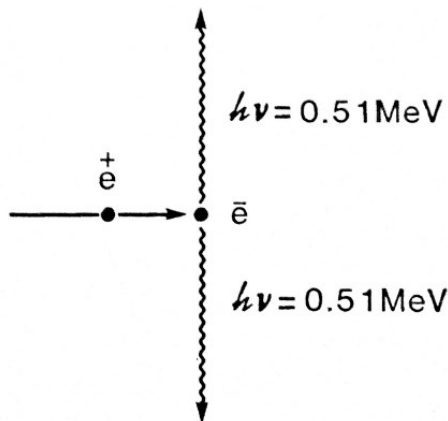


Figure 2.4 Diagram illustrating the production of annihilation radiation [5].

2.3 Kerma and Absorbed Dose

The above photon interactions results in a transfer of energy to the medium (Kerma) and a release of secondary charged particles. Eventually, these charged particles

will deposit their energy within the medium through excitations and ionizations (absorbed dose).

2.3.1 Kerma

Kerma is defined in terms of the related stochastic quantity energy transferred, ε_{tr} , and the radiant energy, R . Energy transferred can be calculated by:

$$\varepsilon_{tr} = (R_{in})_u - (R_{out})_u^{nonr} + \Sigma Q \quad (2.7)$$

where $(R_{in})_u$ = radiant energy of uncharged particles entering a small volume, V , $(R_{out})_u^{nonr}$ = radiant energy of uncharged particles leaving V , except that which originated from radiative losses of kinetic energy by charged particles in V , and ΣQ = net energy derived from rest mass in V . Kerma is an acronym for kinetic energy released in matter.

Radiative losses are conversions of charged particles kinetic energy to photon energy through bremsstrahlung X-rays or in-flight annihilation of positrons. In the circumstance of annihilation, only the kinetic energy carried by the positron at annihilation is classified as radiative energy loss. Radiant energy is defined as the energy of particles emitted, transferred, or received [28].

Kerma is defined by the energy transferred via the following:

$$K = \frac{d(\varepsilon_{tr})_e}{dm} \equiv \frac{d\varepsilon_{tr}}{dm} \quad (2.8)$$

where $(\varepsilon_{tr})_e$ is the expectation value of the energy transferred in the finite volume V during some time interval, $d(\varepsilon_{tr})_e$ is that for an infinitesimal volume dV at a point P , and dm is the mass in dV . [5]. Kerma is expressed in units of J/kg, also known as gray (Gy).

For monoenergetic photons, the total kerma at a point in a medium is related to the energy fluence, Ψ (in units of MeV/cm²), in the medium by the following:

$$K = \Psi \left(\frac{\mu_{tr}}{\rho} \right) \quad (2.9)$$

where $\left(\frac{\mu_{tr}}{\rho} \right)$ is the mass-energy transfer coefficient of the medium for the given monoenergetic photon beam [4].

Kerma can also be separated into two separate components: the collision kerma and the radiative kerma. The collision kerma, K_{col} , is the part of the kerma that leads to the production of electrons that dissipate their energy via ionization in or near the electron tracks in the medium resulting from Coulomb force interactions with atomic electrons. The radiative kerma, K_{rad} , is the part of the kerma that leads to the production of radiative photons as the secondary charged particles slow down and interact in the medium. These result from bremsstrahlung interactions, but can also result from annihilation-in-flight.

2.3.2 Absorbed Dose

The absorbed dose is relevant to all types of ionizing radiation. Absorbed dose is defined in terms of energy imparted, ε , a related stochastic quantity. The energy imparted by ionizing radiation to matter of mass m in a finite volume V is defined as:

$$\varepsilon = (R_{in})_u - (R_{out})_u + (R_{in})_c - (R_{out})_c + \sum Q \quad (2.10)$$

where $(R_{in})_u$ = radiant energy of uncharged particles entering a volume, V ,

$(R_{out})_u$ = radiant energy of all the uncharged radiation leaving V ,

$(R_{in})_c$ = radiant energy of the charged particles entering V ,

$(R_{out})_c$ = radiant energy of the charged particles leaving V ,

$\sum Q$ = net energy derived from rest mass in V .

Absorbed dose is defined as related to energy imparted via:

$$D = \frac{d\varepsilon}{dm} \quad (2.11)$$

where ε is now the expectation value of the energy imparted in V during some time interval, $d\varepsilon$ is that for an infinitesimal volume dV at a point P , and dm is the mass in dV . The absorbed dose, D , is the expectation value of the energy imparted to matter per unit mass at a point. The units of dose are J/kg or Gy.

As a high-energy photon beam penetrates a medium, collision kerma is at a maximum at the surface, as fluence is greatest at the surface (see *Figure 2.5*). The absorbed dose, increases as a function of depth until the value of depth of dose maximum, z_{\max} , is established. Due to photon attenuation and scattering in the medium, a region of transient charged particle equilibrium (TCPE) then occurs where a constant relation between collision kerma and absorbed dose exists [4]. The ratio of dose and collision kerma is denoted as: $\beta = D/K_{col}$, β where is a constant.

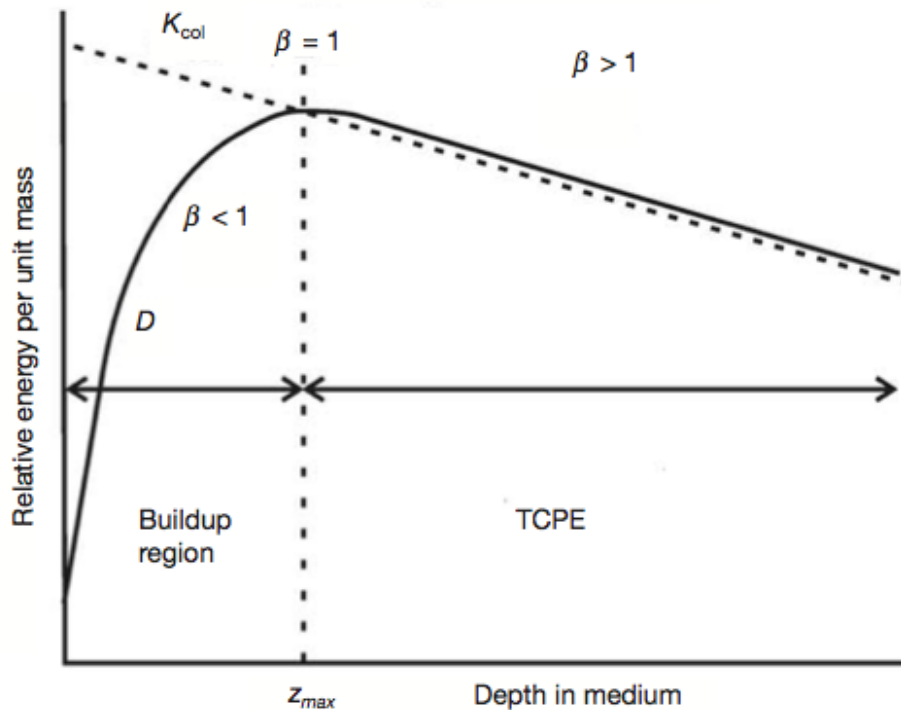


Figure 2.5: Collision kerma and absorbed dose as a function of depth in a medium irradiated by a high-energy photon beam [4].

2.4 The Clinical Linear Accelerator

External beam radiotherapy treatment is predominantly delivered by a clinical linear accelerator (linac). These devices accelerate electrons to kinetic energies from 4 to 25 MeV using microwave radiofrequency fields in the S-band frequency range, most of which are around 3000 MHz. For the cranial cases examined in this study, all treatment beams consist of 6 MV photons [4].

Linear accelerators are mounted isocentrically and the operational systems are distributed over five major sections of the machine: gantry, gantry stand or support, modulator cabinet, patient support assembly, and control console [4]. The patient support assembly as illustrated in *Figure 2.6* has the ability to rotate about a vertical axis as illustrated. The gantry is free to rotate about a perpendicular horizontal axis.

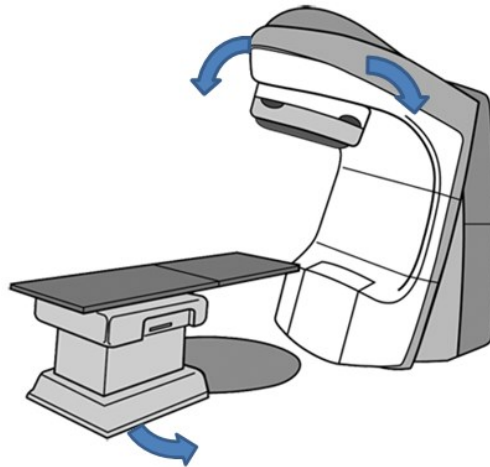


Figure 2.6: Schematic showing the rotational directions for the couch and gantry rotation [26].

The patient support assembly (couch) and gantry rotate about a fixed point in space referred to as the isocenter. In actuality, the isocenter is within a sphere of less than one to two millimeters diameter due to mechanical tolerances. The patient receiving

radiation treatment is located on the couch while treatment angles are modified by rotating the gantry and/or couch about the isocenter. The standard distance from the radiation source in the head of the linac gantry to isocenter is 100 cm and is referred to as the source-to-axis distance (SAD).

The general layout of the linac components is shown in *Figure 2.6* and the main linac beam forming components are comprised of:

- Injection system,
- RF power generation system,
- Accelerating waveguide,
- Auxiliary system,
- Beam transport system,
- Beam collimation and beam monitoring system [4].

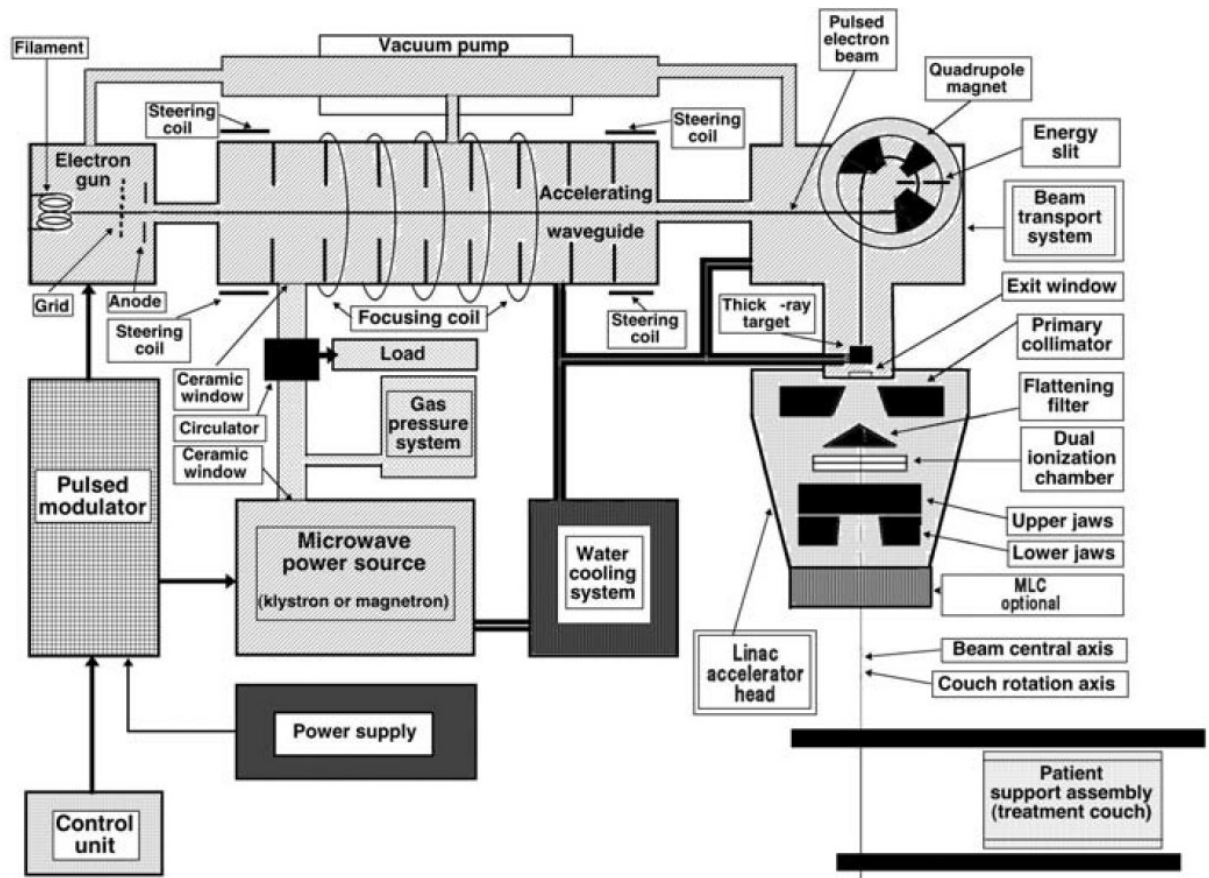


Figure 2.7 Anatomy of a modern linear accelerator [4].

The electrons are injected into the system by an electron gun which contains a heated filament cathode and a grounded anode. The electrons are emitted from the heated cathode after which they are focused into a tight pencil beam by the focusing electrode and accelerate toward the anode before entering the accelerating waveguide [4].

An RF power generation system supplies the microwave radiation, which accelerates the electrons in the waveguide. This consists of an RF power source (klystron in a high energy linac) and a pulsed modulator. The accelerating waveguide is an evacuated device that transmits microwaves. The electrons are accelerated by means of an energy transfer from RF fields produced by the power generators. The accelerating waveguide is divided into a series of cylindrical cavities by discs with circular holes at

the centre. These cavities serve to couple and distribute microwave power and to provide a suitable electric field pattern for the acceleration of electrons. Microwave power that is supplied by the RF generator is transmitted to the accelerating waveguide through another evacuated waveguide filled with a dielectric gas and pressurized to twice atmospheric pressure. Between the RF generator and the accelerating waveguide there is a circulator that transmits RF power and is unreceptive to the reflected radiation moving in the opposite direction, thereby protecting the RF source [4].

The auxiliary system serves several functions, which do not contribute to the acceleration of electrons, but are essential in the operation of the linac. These include a vacuum pumping system that produces a vacuum in the accelerating waveguide and RF generator, a cooling system to cool components (the accelerating guide, target, circulator, and RF generator), a pneumatic target motion system, and shielding against leakage radiation.

In systems where the beam must be bent to make it strike the X-ray target or be able to exit through a beam exit window, bending magnets are employed. Three systems for electron bending have been developed: 90° bending, 270° bending (achromatic) and 112.5° bending magnet (slalom). In the high energy (> 6MV) Varian systems used for treatment at the Nova Scotia Cancer Centre, it is a 270° bending magnet (as is illustrated in *Figure 2.6*). In lower energy systems, bending magnets are not needed as the accelerating waveguide is couple directly to the X-ray target. In high-energy linac systems, drift tubes and bending magnets transport the electron beam from the waveguide to the X-ray target. Additional steering and focusing coils are used to steer the beam down the accelerating waveguide [4].

The linac head is a combination of components to influence the production, shaping, localization, and monitoring of the clinical photon and electron beams. The linac head produces the desired treatment beam from the high-energy electrons exiting the waveguide. The most important components of the linac head include:

- Retractable X-ray targets,
- Flattening filters and scattering foils,
- Primary and secondary collimators,
- Dual transmission ionization chambers,
- Field light and range finder,
- Multi-leaf collimator (MLC) [4].

Conventional photon beams are produced with a combination target and flattening filter. The target and flattening filter are mounted in such a way that can be taken in and out of position depending on the application. In a Varian C-series linac, the target is in a vacuum, while in a Varian TrueBeam unit it is located in air. X-ray production is by means of bremsstrahlung reactions in the X-ray target. The photon beam produced is primarily forward peaked. The flattening filter attenuates the forward-peaked X-ray beam so as the beam is flat at a defined depth in a water phantom (usually 10 cm). In SRS cases, the flattening filter is frequently removed to produce a flattening filter free (FFF) photon beam with a higher dose rate.

The primary collimator shapes the beam to a maximum circular field and is a conical opening machined into a tungsten-shielding block. The side thickness is designed to attenuate the average primary X-ray beam intensity to less than 0.1% of the initial

value in order to minimize leakage. Maximum leakage for the primary collimator cannot exceed 0.2% based on IEC recommendations.

Secondary collimation is generated from two sets of two independent perpendicular jaws, which produce a maximum dimension of 40 x 40 cm² on a Varian TrueBeam STx linac [29]. The field defining light allows the user a visual method for verifying jaw positioning as well as beam shape. The field light illuminates the radiation beam path and the range finder indicates the source-to-surface distance (SSD) [4].

A multi-leaf collimator is a tertiary collimation system with a number of leaves covering the maximum opening defined by the secondary collimation system. These leaves are each individually computer controlled by motors and control circuits. These leaves micro-adjust the aperture of the radiation beam to fit the desired field of treatment [4].

The radiation from the linac is monitored by transmission ionization chambers embedded in the beam path to monitor output during treatment. Once the preset number of monitor units (MU) matches that measured on the primary ionization chamber, circuitry shuts the beam off and terminates the delivery of radiation. The dosimetry system is comprised of two separate ionization chambers with independent readouts. The second chamber acts as a system failsafe so that if the primary chamber fails during patient treatment, the second will terminate the irradiation. In the event both chambers fail, the linac timer will shut the machine down with a minimal overdose to the patient. If the linac is calibrated according to TG-51 [24], the chambers are calibrated such that 100 cGy (1 Gy) corresponds to 1 MU in a water phantom at the specified reference depth on

the central beam axis when irradiated with a 10x10 cm² field at a source to surface distance (SSD) of 100 cm. This system also monitors beam flatness and dose rate [4].

2.5 Dose Calculation Algorithms

The current method of calculating the dose delivered to a patient for a radiation therapy plan with treatment planning software is a combination of calculation algorithms that use analytic algorithms procedures. These algorithms use the information generated from the CT slices during patient imaging to estimate electron density within the patient. Treatment beam energies, treatment beam orientation and weights, treatment prescriptions, and dose delivery objectives are defined in order to define and model an effective treatment.

2.6.1 Eclipse Treatment Planning Software and AAA

The treatment planning software currently used at the Nova Scotia Cancer Centre in Halifax is the External Beam Planning component of Varian's Eclipse Treatment Planning Software v.11 (Varian Medical Systems, Inc., Palo Alto, USA). Eclipse is a treatment planning software that is capable of planning for 3D-CRT, IMRT, VMAT, electron, proton, and brachytherapy. Eclipse uses CT image data and the Hounsfield Unit (HU) values and converts them to electron density according to a predefined calibration curve. The Analytic Anisotropic Algorithm (AAA) is the algorithm used for photon dose calculation within Eclipse for the case studies examined here. AAA, originally conceived by Dr Waldemar Ulmer and Dr. Wolfgang Kaiss [14], is a 3D pencil beam convolution/superposition algorithm that uses separate Monte Carlo derived modeling for primary photons, scattered extra-focal photons, and electrons scattered from the beam limiting devices [14]. Generally, the lateral dose deposition characteristics are modeled

with six exponential curves. Specifically, AAA accounts for tissue heterogeneity by using photon scatter kernels in multiple lateral directions. The final dose distribution is obtained by the superposition of the dose calculated with photon and electron convolutions [14].

A patient scatter model is used for dose inside of the patient while phase spaces model the dose upstream. The beam entering the patient is broken into beamlets, which are modeled using scatter kernels (as mentioned above). These scatter kernels are generated via EGSnrc Monte Carlo [19] with a modeled pencil beam in water. These scatter kernels are scaled to the densities as converted from the CT images. The beamlets are sized according to the resolution of the calculation grid at the isocenter plane. The dose calculation is based on the convolutions over the beamlet cross-sections separately for the primary photons, extra-focal photons, scatter from wedges, and for electrons contaminating the primary beam. All depth-dependent functions using the beamlet convolutions are computed along the central fan line of the beamlet. AAA makes the assumption that the doses resulting from photon and electron scatter can be calculated by a division into two main directions, lateral and depth scatter.

The result of the convolution in AAA is in terms of energy. This energy convolution allows the energy to be conserved more accurately in complex heterogeneous circumstances. The energy is converted to dose using the scaled-water approximation. The energy distribution resulting from an arbitrary beamlet, β , in a sufficiently large homogeneous neighborhood is calculated by the following formula:

$$E_{ph,\beta}(\tilde{X}, \tilde{Y}, \tilde{Z}) = \Phi_{\beta} \times I_{\beta}(z, \rho) \times K_{\beta}(X, Y, Z) \quad (2.12)$$

where the calculation point $(\tilde{X}, \tilde{Y}, \tilde{Z})$ is represented by (X, Y, Z) relative to the origin of the beamlet coordinate system as illustrated in *Figure 2.4*. The fluence, Φ_β , is assumed to be uniform over the small cross section of the beamlet. $K_\beta(X, Y, Z)$ is the photon scatter kernel that defines the lateral energy scattering. The energy deposition function, $I_\beta(z, \rho)$, denotes the area integral of the deposited energy over the surface of the pencil beam at depth z :

$$I_\beta(z, \rho) = \iint h_\beta(t, v, z) dt dv \quad (2.13)$$

where h_β is the poly-energetic pencil beam kernel derived from Monte Carlo simulations.

This energy is converted to dose via the assumption that the different heterogeneities can be modeled as scaled water. Electron densities are used to convert the energy to dose instead of mass density. The final dose is given by:

$$D(\tilde{X}, \tilde{Y}, \tilde{Z}) = c E_{ph, \beta}(\tilde{X}, \tilde{Y}, \tilde{Z}) \cdot \frac{\rho_{water}}{\rho(\tilde{x}, \tilde{y}, \tilde{z})} \quad (2.14)$$

where c is a unitless coefficient handles the unit conversion from J/m^3 to Gy and ρ is electron density in units of number of electrons/cm³ [14].

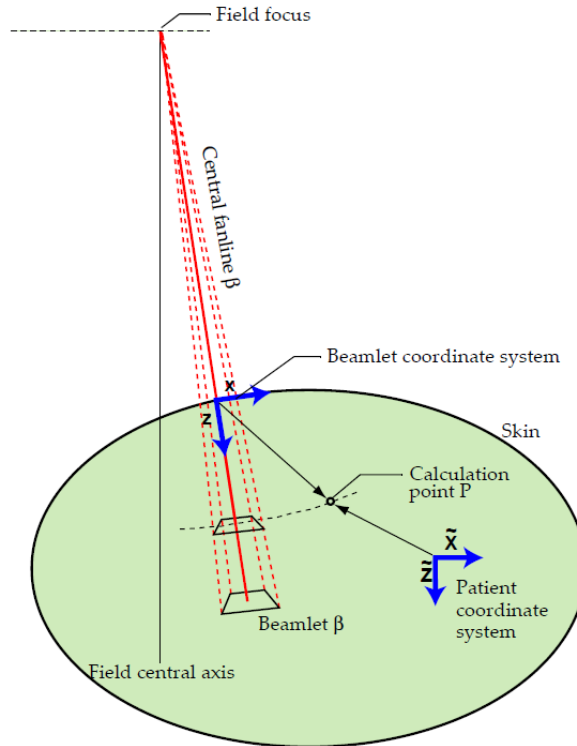


Figure 2.8: Schematic of a beamlet in the AAA [14].

2.6.2 VMAT Optimization

VMAT [15] is a radiotherapy delivery technique that modulates dose and preferentially shields healthy tissue dynamically during beam delivery. VMAT is an arc-based radiotherapy method that uses gantry arcs to deliver multiple shaped MLC apertures. The dose modulation occurs by creating a unique MLC pattern at each control point (gantry angle), varying the dose rate, and, if required, varying the gantry rotation speed. VMAT optimizes a two-dimensional fluence map and arranges MLC patterns in multiple, unique and independent apertures to create a treatment plan that passes a threshold of clinical acceptability. The process for pre-optimization includes defining the target for the radiotherapy treatment, as well as defining the healthy tissue structures nearby. Each of these structures then has set dose objectives input to the optimization

process. The optimization aims to meet the prescription dose objectives to the target volume while simultaneously limiting dose to healthy structures at the user-specified dose objectives. Beam's eye view (BEV) aperture shapes are defined based on Boolean operations of target and healthy tissue structures. The number of MU for each aperture is then optimized based on a dose-volume cost function. The cost function is based on specified minimum and maximum dose constraints for each volume. For each constraint, a relative priority value is assigned and a cost is calculated using a standard quadratic dose difference multiplied by priority value. The total cost is the sum of all total individual constraint cost values. Each iteration of the optimization randomly selects an available gantry sample then changes the MU weight or MLC leaf position for that sample. If a change doesn't violate a mechanical or efficiency constraint the dose distribution and cost function are calculated. If the cost is reduced, the change is accepted, otherwise it is rejected.

Constraints are also placed on MLC leaf motion and MU variation to preserve continuous delivery. These are defined by gantry rotation angle as:

$$\frac{\Delta x}{\Delta \theta} \leq \left(\frac{dx}{d\theta} \right)_{max}, \quad \frac{\Delta MU}{\Delta \theta} \leq \left(\frac{dMU}{d\theta} \right)_{max} \quad (2.15)$$

where x , MU , and θ are MLC leaf positions, MU weight, and gantry angle, respectively. $\left(\frac{dx}{d\theta} \right)_{max}$ and $\left(\frac{dMU}{d\theta} \right)_{max}$ are user-specified upper bounds for maximum speed of motion for MLC and MU weight, respectively. The continuous nature of the aperture sampling allows a very fast treatment as compared to other forms of radiation therapy, while matching or improving upon the quality of techniques like IMRT [15].

Eclipse uses the Progressive Resolution Optimizer (PRO) algorithm to create VMAT plans. The PRO generates a sequence of control points, which define MLC leaf

positions and MU/deg as a function of gantry angle. Control points are sampled locations of all components of the linear accelerator that are in motion. The unit must meet the positions dictated in these control points and interpolate the regions between control points to provide a smooth delivery. The algorithm uses a multi-resolution approach to optimize plans by modelling the dose using first a low number of dose calculation segments. Intermediate points between these initially established points are then generated which subdivide the distance between the control points. The motion of components is linearly interpolated between sampled control points. As the algorithm continues, it samples at increasingly fine resolution, minimizing the distance of segments between samples. The dose in a segment is calculated from the combined fluence through the MLC apertures and the control points located within a certain sector of the arc. At the beginning of the optimization, the initial MLC shapes are conformed to the targets and the initial dose rates are equal for all dose calculation segments. The MLC shapes and dose rates of the different control points in the VMAT field are optimized, with large adjustments being made in initial phases and slowly decreasing the size of adjustment [14]. The result is a plan which has been optimized to effectively treat the target volume with the defined prescription dose, yet limits as much of the dose to normal tissues as possible.

CHAPTER 3 METHODS AND MATERIALS

As this research aims to create a general approach to permit the assessment of any patient, it must comply with the current procedural workflow to be feasible to implement in the treatment planning process. This procedure must be a compatible step in the planning process. From the time the radiotherapy patient arrives at the hospital for the first time until delivery, there is a well-established planning process to which this research seeks to be a potential addition. As such, it utilizes the same initial information as the treatment planner to make decisions based on ensuring the delivery of the prescription dose to the target while limiting the dose to normal tissue.

3.1 Importing Anatomical Information

The patient's anatomical information is taken from the computed tomography (CT) images from the patient's initial CT scan. This is the vital source of information for patient treatment planning, as it is a representation of the internal anatomy of the patient. These CT slices are transverse cross-sections of the patient taken at equal spacing across the portion of the patient relevant for treatment. These cross-sections allow treatment planners to see into the patient and examine the arrangement of internal structures. To identify these structures, the outline of the shape of the structure is drawn, or contoured, in each CT slice in which it is present. These two-dimensional contours are then interpolated between each slice in which they are drawn to create a three-dimensional structure showing the outline of the volume. This effectively gives the treatment planner the ability to clearly visualize the outline of all the important volumes within the patient anatomy.

This patient anatomical information can be exported from Eclipse (Varian Medical Systems, Inc., Palo Alto, USA), the treatment planning software at the Nova Scotia Cancer Centre, in a series of Digital Imaging and Communications in Medicine (DICOM)-format files. These files contain CT slices and the contouring information designed by the treatment planner. These DICOM files also contain reference points, which allow the treatment planner to design and align the treatment according to known locations within the treatment delivery room, as well as all the treatment planning beams. Using the information in the file containing the contoured structures, projections of these three-dimensional contoured volumes can be calculated after importing them into MATLAB (The MathWorks, Inc., Natick, Massachusetts, U.S.A.).

3.2 Calculation of Overlap

As the gantry and couch position changes, the X-ray source position is altered with respect to the patient. This means that the radiation beam's path has now been modified to approach the patient on a new incident trajectory and requires a new assessment of structures along the path length of the beam. As we are trying to assess the amount of overlapping sensitive organs-at-risk (OAR) with our target volume (or Planning Target Volume, PTV, used interchangeably throughout), it is important to accurately model the changes made to the arrangement of the anatomical structures as we alter the orientation of the patient with respect to the source. A plane is located at the machine isocentre, a fixed location within the treatment planning room, which is a static defining feature of radiotherapy planning. Projecting structures accurately to this two dimensional plane generates what is equivalent to the radiation BEV (see *Figure 3.1*).

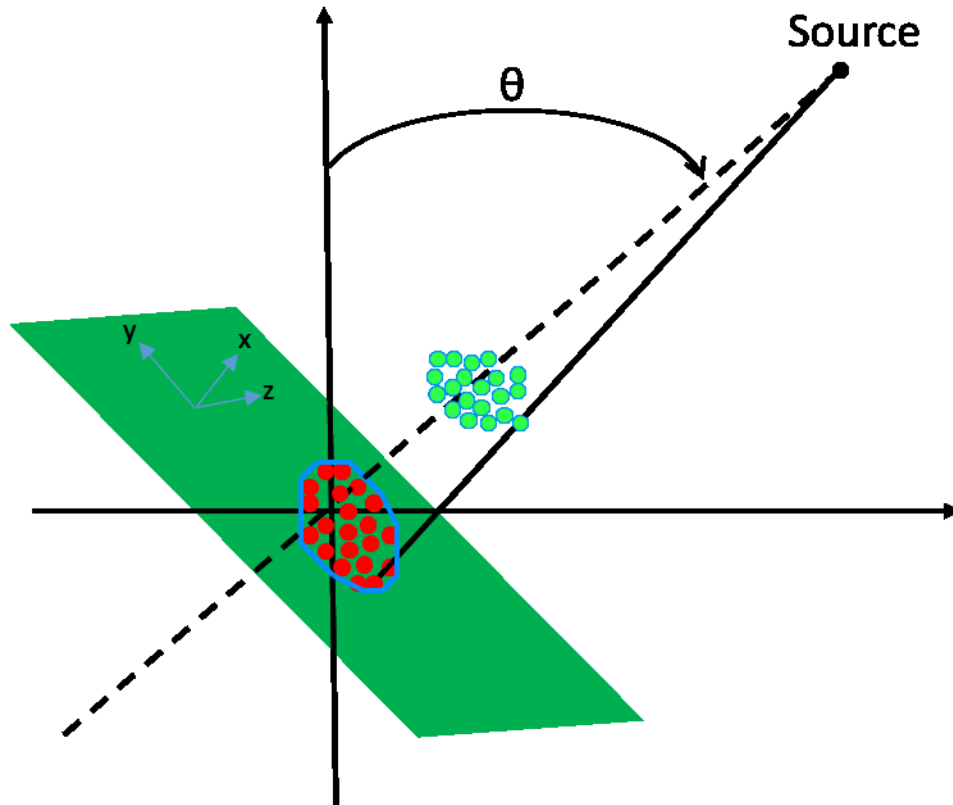


Figure 3.1: Projection of a volume onto a plane at isocentre. A line is drawn from the source position, based on rotational position of the gantry through each point making up the volume. The coordinate system described in the anatomy rotation is also pictured [16].

The position of the gantry and the patient couch alters the constituents of the BEV and the arrangement of the anatomy. Each unique BEV will correspond to different values of overlap for each OAR and target (PTV).

Since the DICOM structure file contains the information we need regarding the relative positioning of the three-dimensional volumes contoured, we can extract from this the arrangement of the patient. The assessment of the overlap between any OAR and the designated PTV must be evaluated individually. The desired OAR for comparison is chosen from a list of volumes and each volume is projected onto a two-dimensional isocentric plane with the PTV by drawing a line from the source position, based on the

rotational position of the gantry, through each point that makes up the volume (see *Figure 3.1*). This effectively draws the structure as it would be viewed from the source position and each point is a representation of a projection line drawn from the source, through the volume, onto the plane at isocentre.

3.2.1 Mutual Plotting Method

The two-dimensional coordinate points that compose each of the structures (OAR and PTV) being evaluated are drawn and the coordinates are filed into an xy-coordinate system based (See *Figure 3.1*) on the vertical and horizontal location of the points on the plane. The code simultaneously projects multiple volumes onto the same plane, inside of the same visualization window in MATLAB.

The angles over which the code is being analyzed are supplied by the user for both the rotation of the couch, and the rotation of the gantry, along with the interval at which each are being iterated. Along with these, the PTV and OAR indices and the isocentre location are extracted from the DICOM file and input into the projection program in order to accurately represent the structures with reference to a central point of rotation (the isocentre). A coordinate space is established and defined in which the plane viewed from the X-ray source position is the yz-plane and a rotation about the y-axis indicates a patient support system rotation. The initial vectors for the yz-plane are found for a gantry and couch angle of zero and the source location is established 100.0 cm away in the x-direction (for gantry and couch angle zero). Rotational matrices are then established for both couch and gantry rotations in order to properly apply these rotations to the yz-plane. The three-dimensional rotation matrix for the couch is a rotation about the y-axis given as:

$$\begin{pmatrix} \cos\theta_C & 0 & \sin\theta_C \\ 0 & 1 & 0 \\ -\sin\theta_C & 0 & \cos\theta_C \end{pmatrix} \quad (3.1)$$

where θ_C is the current value for the couch rotation. The rotation of the gantry is a rotation about the z-axis, which can be represented by the three-dimensional rotation matrix as:

$$\begin{pmatrix} \cos\theta_G & -\sin\theta_G & 0 \\ \sin\theta_G & \cos\theta_G & 0 \\ 0 & 0 & 1 \end{pmatrix} \quad (3.2)$$

where θ_G is the current value for the gantry rotation. These rotations are then applied to the source position, and the initial vectors, which establish the plane, are also adjusted to represent the structures as currently visible between source and new isocentric plane. This process is iterated from first to final gantry angle and from first to final couch angle at their respective specified intervals.

At each CG-coordinate position, the coordinates of the structures, which have been reduced to their two-dimensional projections, are each drawn and a profile is drawn around the exterior of each. The area of the profile of each the structure is drawn using the *convhull* MATLAB function that returns the 2D convex hull of the projection areas. This area is measured and registered using the *trapz* MATLAB function for trapezoidal numeric integration. This area is filed according to the current CG-position for later calculation.

The two-dimensional coordinates that constitute a projected volume are then adjusted to adhere to a fixed grid (See *Figure 3.2*). This grid is established with the purpose of finding similarly drawn points between both structures and establishes them as coordinates, which belong to a volume representing the geometric overlap between the two structures. When each structure currently being registered for overlap is plotted, the

coordinate points, which constitute the area in which these overlap, are not always aligned. This means that if a coordinate is tested within an overlapping area of one of the structures to see if it is present in the other structure, while the two may be very close, the points will not mutually be found. However, if we correct these points to adhere strictly to a two-dimensional grid, the points that are in close proximity in both volumes can be correctly established as mutual. The grid spacing that was most accurate was empirically established as mutual. The grid spacing that was most accurate was empirically established of having a spacing of 0.32 mm, and this was determined by using two spheres of known areas of projection with a known area of overlap between the two.

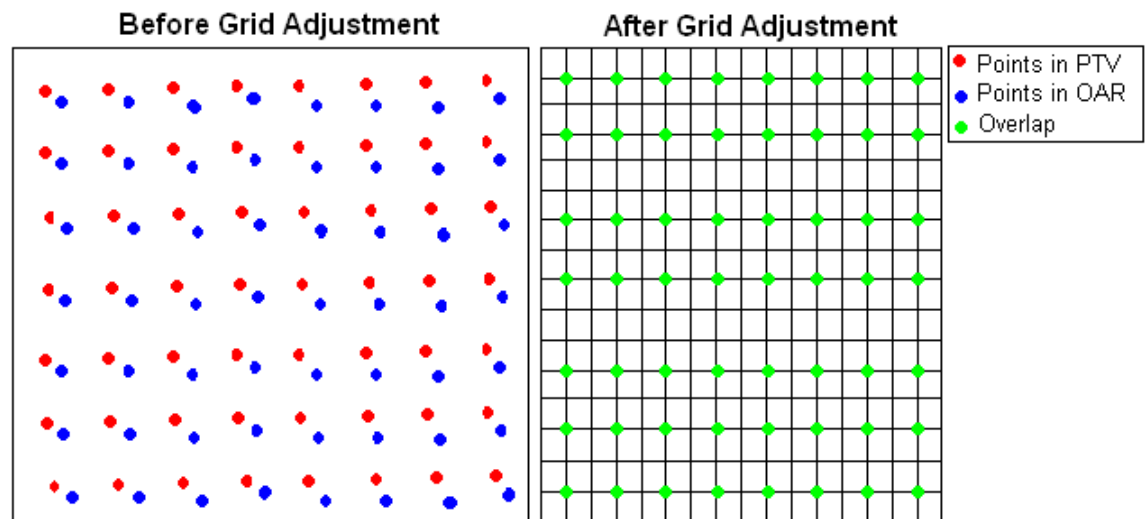


Figure 3.2: Diagram showing the adjustment of all points to a 2D grid to establish similarly drawn points as an overlap. The grid spacing was 0.32mm.

All points within one volume are tested to see if they can be found mutually in both volumes. The points that do have mutual points in each volume are understood to be overlapping coordinates and are filed according to their index within the evaluated structure. These points are then registered based on their location *before* the adjustment to the grid had occurred. While the grid has only marginally adjusted them, the true location of these points was as they were drawn initially in the structure. These points represent

the overlap area between the two volumes, using the coordinates of one of the evaluated structures. This overlap area then undergoes the same assessment as the two initial volumes for establishing the area of the plotted coordinates by using the convex hull (*convhull* function) and trapezoidal numerical integration (*trapz* function) procedures.

3.3 Generation of Overlap Scoring Map

3.3.1 Geometric Overlap Score Equation and Map

Section 3.2 describes the method for calculating the overlap found between a PTV and a single chosen OAR at a specific couch/gantry positioning. This process is conducted iteratively for every CG-coordinate that is a valid combination of couch and gantry positioning for treatment.

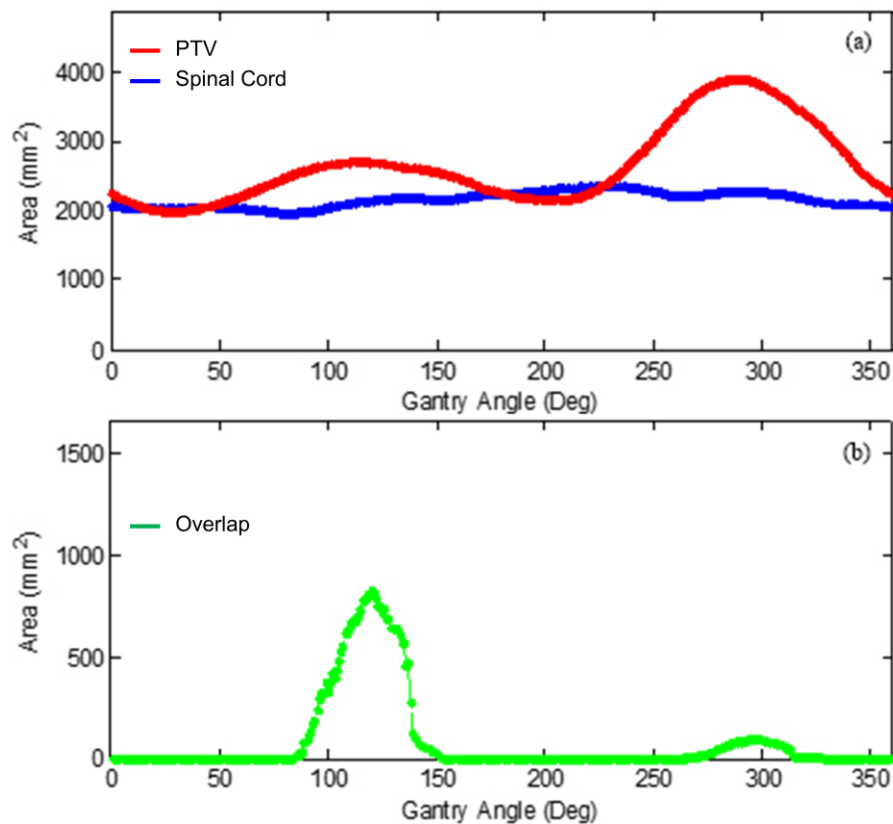


Figure 3.3 (a), the area of the PTV is drawn in red, the area of the OAR in blue and the overlap is drawn in green in (b). For the measured data in this plot, the couch was fixed at a 0° position while the gantry rotated.

The evaluation proceeds with the couch in a fixed position and the gantry is allowed to rotate in a full rotation as specified by the user. The result is a set of overlap calculation values for all the gantry positions at this specific couch angle. *Figure 3.2(a)* shows the plotting of this data for an evaluation of two volumes: a PTV shown in red and the spinal cord shown in blue. *Figure 3.2 (b)* shows the values for the overlap between the two structures at a fixed couch position while the gantry is rotated in a full 360° rotation. The largest peak, which is centred at approximately 120°, is the BEV in which the spinal cord is between the source and the PTV and a large area of the spinal cord overlaps with that of the PTV, a foreground overlap. The second slightly smaller peak, which centres at approximately 295°, corresponds to the OAR being in a background overlap in which the PTV is between the OAR and the source. These overlap scenarios do not correspond to equivalent risk and are not equivalently compared, as the scenario in which the OAR must be traversed in order to deliver sufficient dose to the PTV is a much less desirable arrangement for radiotherapy treatment. How this is dealt with will be explained shortly.

The ranking of every valid gantry and patient support combination is conducted via a method proposed by Yang *et al* [1], which evaluates the amount of geometric overlap between the radiotherapy PTV and every OAR of radiation exposure within the patient anatomy. This overlap, $E(c,g)$, is evaluated for each gantry (g) and patient support rotational angle (c) via *Equation 3.1*, where w_i is a relative weighting factor for the i^{th} OAR, $L_i(c, g)$ is the overlap area between the PTV and the i^{th} OAR, $A_i(c, g)$ is the area of the i^{th} OAR, and $A_P(c,g)$ is the area of the PTV. These areas are based on the projections of the PTV and OARs onto a plane as defined at the distance of the rotational axis of the

gantry from the radiation source position. The normalization to the projection area of the PTV and OAR compensates for variations in sizes of these volumes.

$$E(c, g) = \sum_i w_i \times \left[\frac{L_i(c, g)}{A_t(c, g)} \times \frac{L_i(c, g)}{A_i(c, g)} \right] \quad (3.3)$$

In order to analyze the entire couch/gantry space, these measurements must be taken at each couch angle in addition to every gantry angle.

Once we have a measurement such as that shown in *Figure 3.2 (b)*, we file this information along the y-axis (gantry angle) for a specified couch angle θ_C , which is along the x-axis. The amplitudes of the values are indicated via a colour map in which dark red indicates the most overlap present and dark blue indicates the least amount of overlap. (See *Figure 3.3* for an example of a completely mapped CG-coordinate overlap space for one OAR).

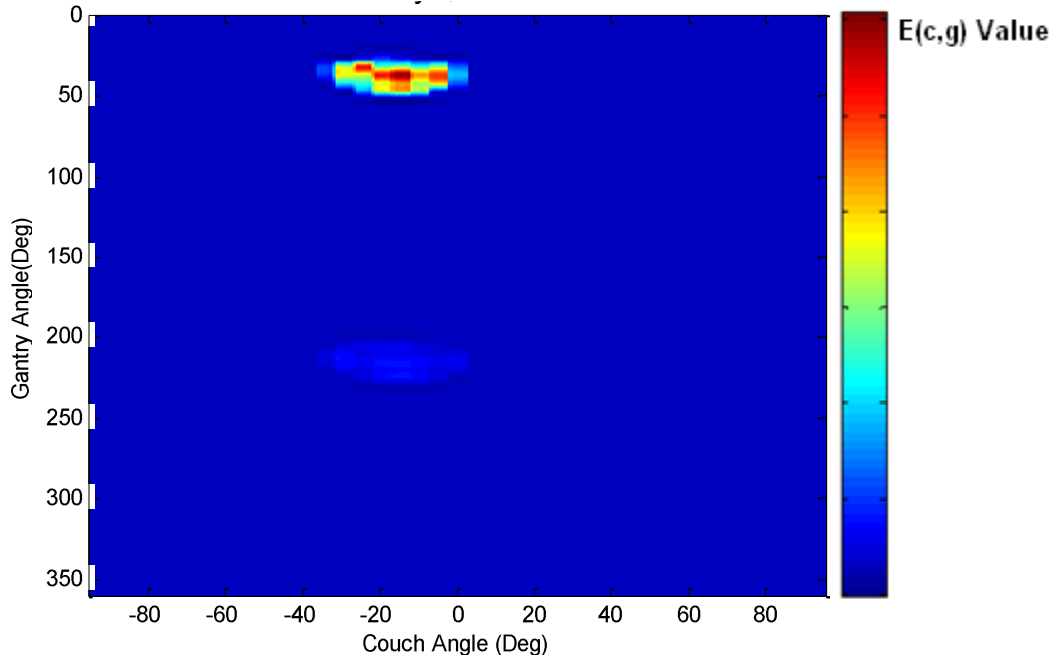


Figure 3.4: Overlap map between the PTV and the left eye.

Any coordinate within this plot represents its couch/gantry position and the amount of overlap present in that coordinate is given by its color in reference to the color scale shown above.

We have introduced an additional factor, F , to *Equation 3.3* in order to account for the possibility that the overlap can occur in the space between the PTV and the source (a foreground overlap), or can occur behind the PTV (a background overlap). This is a coefficient that reduces the overlap value by a factor of ten (arbitrarily set) in the case of a background overlap. *Equation 3.3* with the added factor F is *Equation 3.4*:

$$E(\mathbf{c}, \mathbf{g}) = \sum_i w_i \times F \times \left[\frac{L_i(\mathbf{c}, \mathbf{g})}{A_t(\mathbf{c}, \mathbf{g})} \times \frac{L_i(\mathbf{c}, \mathbf{g})}{A_i(\mathbf{c}, \mathbf{g})} \right] \quad (3.4)$$

Another additional weighting factor is w_i , which relates the importance of these OARs relative to one another. All exposure to organs cannot be evaluated equivalently as all OARs cannot tolerate the same quantity of dose. As such, the overlap of these OARs must be weighted according to this sensitivity, which is done within the algorithm.

One of the clinical references for the sensitivity of an organ-at-risk is the Quantitative Analysis of Normal Tissue Effects in the Clinic (QUANTEC) [2]. With the assistance of QUANTEC, the algorithm can appropriately incorporate a hierarchal system to rank the OARs according to their need for limiting the exposure to radiation dose. Additionally, Hall *et al* [3] was consulted for clinical radiation dose constraints. If the constraining value found in Hall *et al* was more conservative than that found in QUANTEC, the value from Hall *et al* was used. The radiation dose limitations, D_{tol} , to these organs given by QUANTEC [2] and Hall *et al* [3] are listed in *Table 3.1*. We define w_i as $1/D_{tol}$ where D_{tol} is the tolerance limit in Gy for that particular OAR. This unit is not kept for the output value $E(\mathbf{c}, \mathbf{g})$. This factor is used solely for the relative comparison

of OAR risk weighting. Exceeding the tolerance limit for an OAR results in an increased probability of toxicities or complications in that OAR. This tolerance limit can either be a maximum dose to any part of the organ or a mean dose, depending on the OAR in question. The overlap score for an individual coordinate is thus more expansively represented as:

$$E(\mathbf{c}, \mathbf{g}) = \sum_i \frac{1}{D_{tol_i}} \times F \times \left[\frac{L_i(\mathbf{c}, \mathbf{g})}{A_t(\mathbf{c}, \mathbf{g})} \times \frac{L_i(\mathbf{c}, \mathbf{g})}{A_i(\mathbf{c}, \mathbf{g})} \right] \quad (3.5)$$

While there is variability between anatomical positioning throughout the cranial cases analyzed, the surrounding OARs are common throughout the patients. A cranial cancer case is very proximal to the ocular structures such as the eyes, optic chiasm, optical nerves, optical tracts, and lenses, as well as the brainstem and healthy brain tissues.

The weighting factors w_i and F will further modify the geometric overlap map for each OAR. Once a weighted geometric overlap map for each OAR has been calculated, all maps are summed to produce a total geometric overlap map for all OARs.

Table 3.1: Dose limitations for the most common OARs in cranial cancer cases.

Organ at risk of exposure	Dose Constraint (Gy)	Limit Definition	Risk of Exceeding	Reference
Brainstem	54	Maximum dose (< 5% Rate)	Cranial Neuropathy or Necrosis	QUANTEC
Chiasm	55	Maximum dose (< 3 % Rate)	Optic Neuropathy	QUANTEC
Lens	10	Maximum dose (TD 5/5)	Cataract	Hall <i>et al</i>
Eye	45	Maximum dose (TD 5/5)	Blindness	Hall <i>et al</i>
Optic Nerve	55	Maximum dose (< 3 % Rate)	Optic Neuropathy	QUANTEC
Optic Tract	55	Maximum dose (< 3 % Rate)	Optic Neuropathy	QUANTEC
Normal Brain	45	Maximum dose (TD 5/5)	Infarction, necrosis	Hall <i>et al</i>
Cochlea	45	Mean dose (< 30 % Rate)	Hearing Loss	QUANTEC
Pituitary	45	Maximum (TD 5/5)	Hypopituitarism	Hall <i>et al</i>

3.3.3 Collision Zones

Due to the physical configuration of the gantry and patient support system, there are certain CG-coordinates, which are not valid for entry in the geometric overlap map. These values account for the positioning of the gantry and couch in which the two occupy the same space inside the treatment room. If these CG-coordinates were included in the trajectory and delivered at the machine for treatment, the gantry and couch would collide in attempting to reach these positions. These positions are aptly named collision zones. These collision zones also include regions in which the gantry would collide with the space that the patient would occupy.

These collision zones were measured on a Varian TrueBeam STx (Varian Medical Systems, Inc., Palo Alto, USA) Linear Accelerator at the NSCC. An anthropomorphic phantom was positioned in a typical treatment arrangement for cranial cancer patients. The treatment couch was positioned at a longitudinal position of 90.85 cm, a vertical position of 15.00 cm and a lateral position of 0.00 cm. The couch was positioned at the one extreme of its rotation travel and moved in one-degree increments across its total range. A point in a collision zone was recorded for which the couch position and gantry position were such that: (i) the collision avoidance system of the TrueBeam was triggered or (ii) the gantry was within a 5 cm buffer to either the treatment bed or the anthropomorphic phantom. The CG-coordinates within these zones were assigned a value higher than the normalized maximum of whatever value was measured for overlap within a map, in order that a coordinate within a collision zone could never be included in the optimized trajectory (see *Figure 3.4* for an example.)

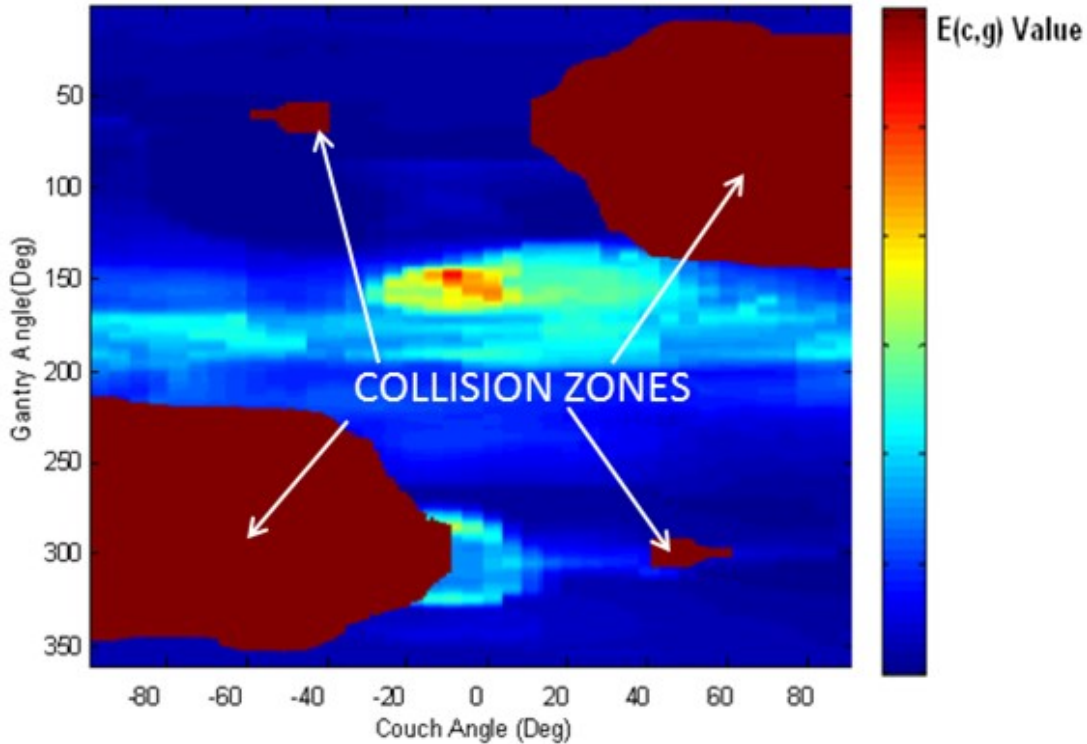


Figure 3.5: An overlap map with all OARs for the patient included. The large dark red regions indicate collision zones of the CG space.

These collision zones are much less conservative than those found in Yang *et al* which occupy almost the entire quadrant of the overlap map.

3.4 Algorithm for Trajectory Navigation

The weighted overlap map is used by the trajectory design algorithm, which then determines a navigable path through this overlap map in the most effective and efficient means possible. The first step in this process is identifying, for each independent gantry angle, the patient support angle that has the lowest value of $E(c,g)$ from Equation 3.5. For each gantry angle, these coordinates are indications of the position of the patient support system corresponding to the lowest possible amount of overlap. Radiation delivery at these coordinates would be the trajectory that corresponds to the least amount of radiation exposure to OARs by the primary radiation beam. However, the trajectory output by

identifying the minimum values from *Equation 3.5* (example as shown in *Figure 3.4*) is not useful clinically due to the extreme discontinuity of the patient support motion. There are far too many discrete movements in couch and gantry positioning to be realistic in terms of time of delivery within a clinical setting. The algorithm must now seek to create a smooth patient support trajectory, which will increase delivery time, while simultaneously working to minimize the values of the overlap within the optimized trajectory.

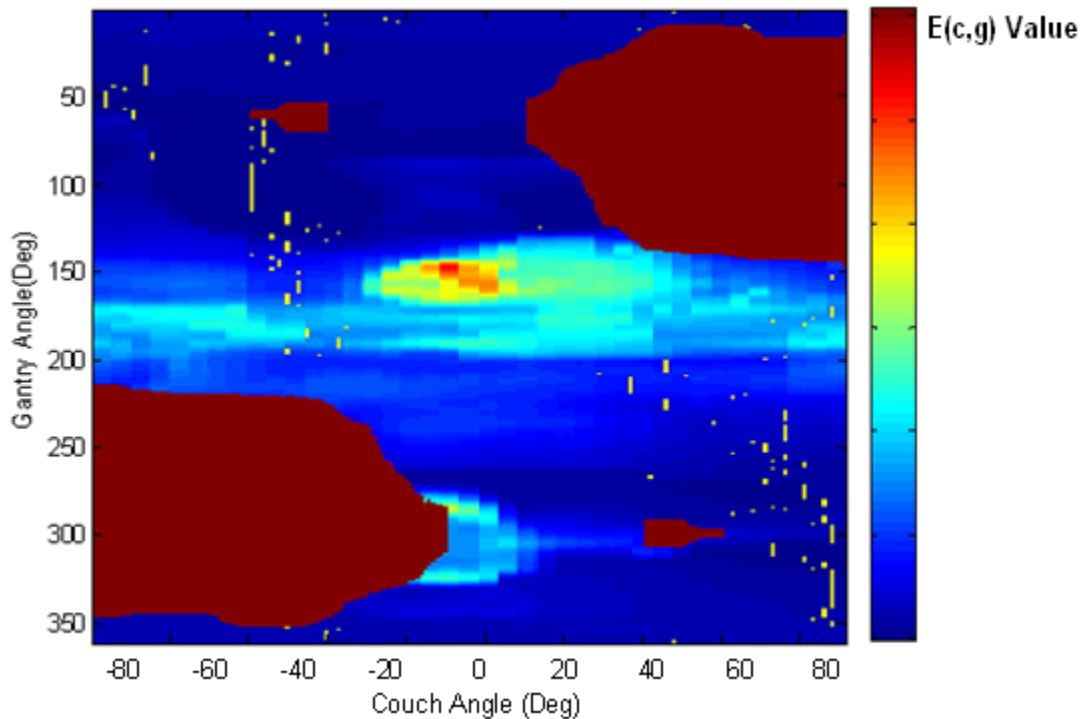


Figure 3.6: An overlay of the trajectory, indicated as yellow lines, designed by identifying the patient support and gantry positions that correspond to the minimum output from *Equation 3.5*.

3.4.1 Parameter Entry for Smoothing

Any patient support position that is an absolute minimum for a particular gantry position is a desirable component for building the treatment trajectory. The ability to use these absolute minima depends on the absolute minima at nearby gantry positions. If

these minima can be delivered without patient support motion or with little motion to connect these points, they are suitable for use in the trajectory.

The evaluation of the suitability of absolute minimum coordinates can be conducted using an originally designed threshold method, which examines the stability of existing nearby coordinates at every coordinate within the trajectory. At six customizable gantry positions before $(x - d3, x - d2, x - d1)$ and after $(x + d3, x + d2, x + d1)$ the location being evaluated, x , customizable parameters are established $(P1, P2, P3)$, respectively, as depicted in *Figure 3.6*. At each of these locations, the parameters $(P1, P2, P3)$ are respectively used as a threshold to see if the couch positions fall within this distance from the evaluated point. According to the number of evaluations that successfully pass, a ranking is established as an indication of how suitable this absolute coordinate point would be for inclusion in a treatment trajectory. The higher the number of desirable points, the higher the ranking. Only the points which receive the highest ranking (i.e. passed all three parameters) are kept in the trajectory, while all other lower ranking coordinates are removed as they contribute to the discontinuity of the initially constructed trajectory. The optimized trajectory now includes only absolute minimum positions, which have been evaluated as above.

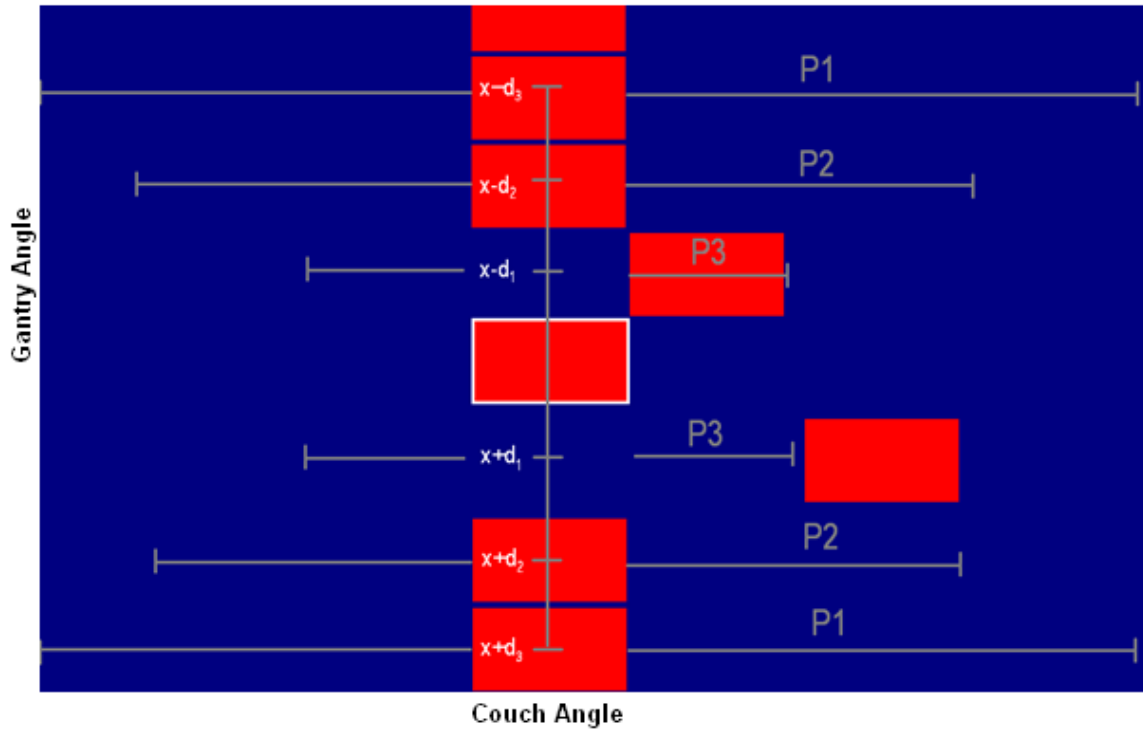


Figure 3.7: A visualization of the flexible threshold evaluation of the patient support position for suitability in the trajectory. x is the coordinate being evaluated bordered in white. $d3$, $d2$, $d1$ are user-assigned parameters for the gantry distance from x that the evaluation extends. $P1$, $P2$, $P3$ are values for the width the evaluation searches for neighboring couch positions with less overlap.

The result is a number of short sub-arcs, as displayed in the example shown in *Figure 3.7*. The next step is to connect these sub-arcs in a smooth path while maintaining minimal overlap of OARs within the trajectory. Simply joining the end-points of the existing sub-arcs previously established can temporarily fill in the gantry positions that have yet to have assigned patient support positions in the trajectory and this is conducted by simple linear interpolation within the gaps.

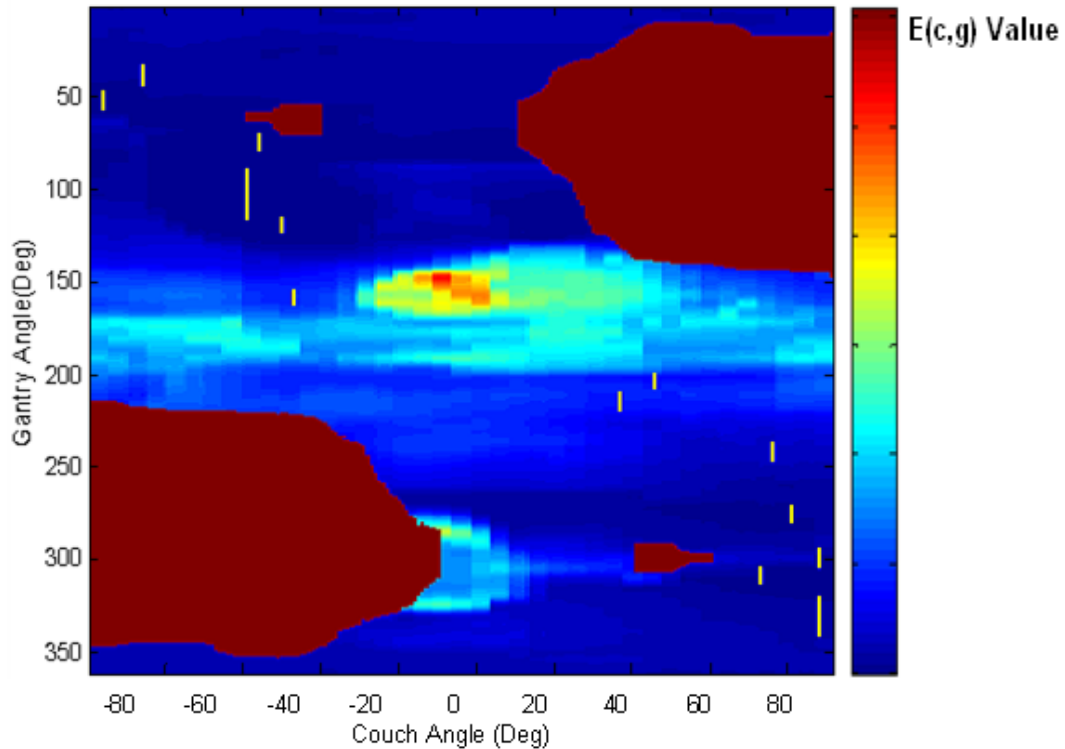


Figure 3.8: An example of the trajectory, indicated as yellow lines, after the absolute minimum coordinates have been reduced to include only positions within the user-specified evaluation criteria.

As previously stated, the objectives for the algorithm are two-fold: to ensure the smooth and quick delivery of the treatment, and minimize the overlap throughout the trajectory. This simple interpolation is in line with the former, but it does not take into account the minimization of overlap. Dose will be delivered at every coordinate within the trajectory so this interpolation must be chosen with minimal overlap. An additional evaluation is conducted on each point within the interpolation to ensure that these portions of the trajectory do not contribute to significant addition of overlap. At each interpolated point, the algorithm examines the nearby patient support positions at a customizable distance k away from the existing point for a smaller value of overlap (see *Figure 3.8*). If a patient support position within the specified distance away has a smaller overlap value, the algorithm will change the patient support coordinate to this value. A

complete trajectory is displayed in *Figure 3.10*. The discontinuities in the trajectories indicate regions where the gantry motion would be paused while the couch repositions. A flowchart outlining this entire optimizing procedure is shown in *Figure 3.9*.

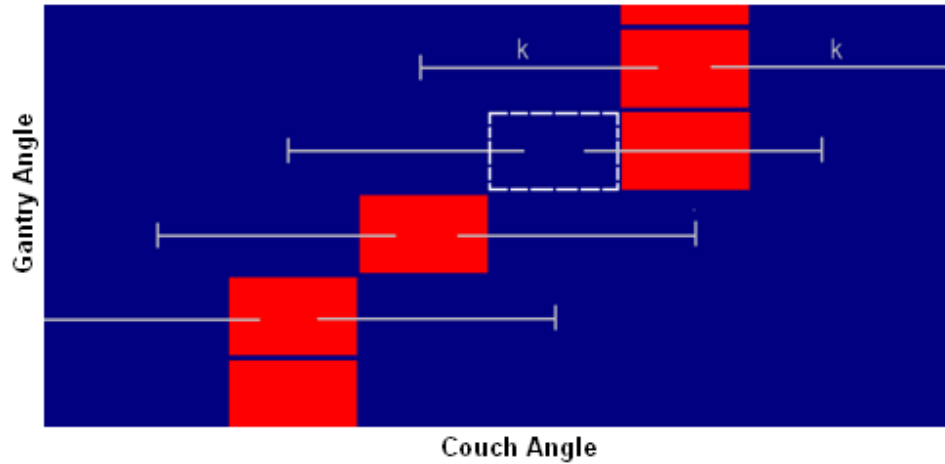


Figure 3.9: Visualization of the evaluation of nearby patient support positions with a lower overlap value. The dashed rectangle represents a former interpolated point. The point to its right is an adjusted coordinate with a lower overlap value.

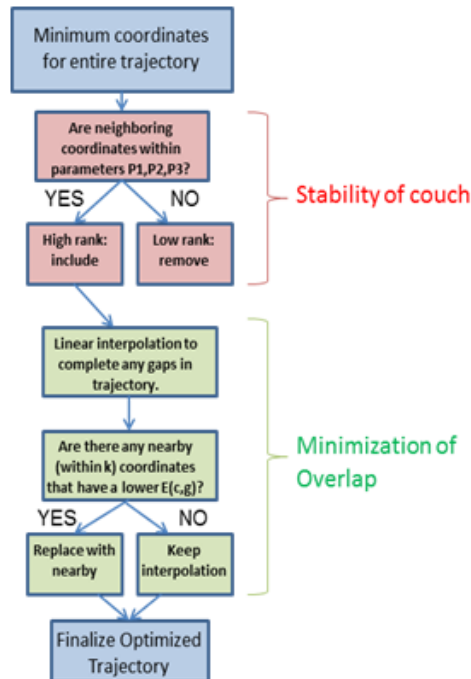


Figure 3.10: Flowchart describing trajectory optimization.

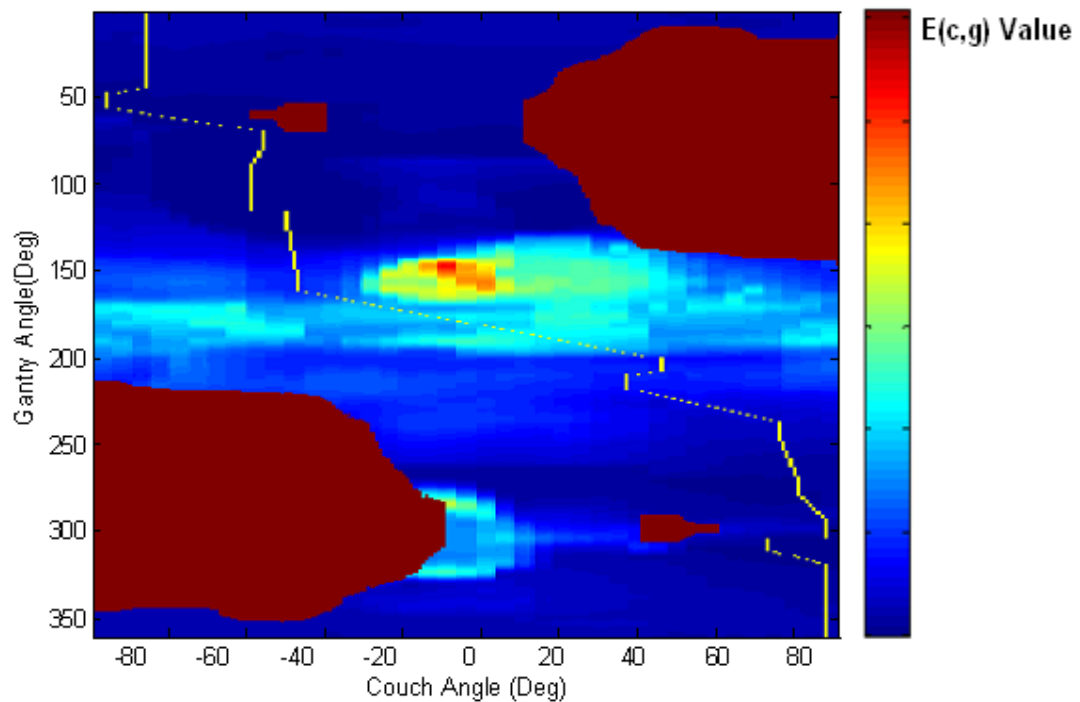


Figure 3.11: An example of a completed treatment trajectory, indicated as yellow lines, overlaying the patient-specific overlap map.

3.4.2 Output Parameters

As output, the algorithm displays:

- Patient specific weighted geometric overlap map of all OARs.
- A visualization of all of the absolute minimum coordinates.
- A visualization of the minimum coordinates included in the optimized trajectory.
- An overlay of the final optimized trajectory with the geometric overlap map.

In addition, a matrix is created which includes the final coordinates of an optimized trajectory.

As additional output parameters, the algorithm also provides:

- Percentage of absolute minimum coordinates used in the final optimized trajectory.

- Percentage of accumulated overlap score that the smoothing process contributes to trajectory overlap.
- Percentage of accumulated overlap score of a treatment with patient support at a 0° position for an entire 360° gantry rotation, i.e. - no patient support motion for the same patient. This is used for comparison of overlap in fixed couch treatments.
- The approximate time added to move the patient support system to all locations within the trajectory.

All of these output parameters and display windows allow the user to make a judgment on whether the final output trajectory designed by the input parameters meets the specific needs and priorities of the intended optimization. This means deciding if the amount of couch motion is suitable in terms of time of delivery. The algorithm can be iterated repeatedly while altering any of the input thresholds or parameters until the user's trajectory is appropriate. The algorithm takes only seconds to run, and the time of delivery can be calculated from the output travel time of the couch rotation within the treatment trajectory.

3.4.3 Restrictions for Import into Eclipse

The output of the trajectory design algorithm is a dynamic trajectory involving simultaneous couch and gantry motion for a full gantry rotation of 360° , however it is also fully capable of multiple rotations. This trajectory is optimized according to user-specified priorities regarding overlap between the OARs and the PTV, the treatment delivery time, and the scale of the couch motions. This trajectory can be imported to a treatment planning system capable of performing dose modulation and collimation adjustments to a radiotherapy trajectory containing simultaneous couch and gantry rotation.

Unfortunately, Eclipse has a number of restrictions that will not allow the fully optimized trajectory to be input for VMAT optimization, including not supporting simultaneous gantry and couch motion. To overcome the restriction of simultaneous motion in order to be accepted by the VMAT optimization algorithm, the optimized trajectory must be divided into subsections, which take any couch motion and divide it into discrete subarcs of gantry motion containing fixed-couch position subarcs. At the extreme, a plan could be broken into 360 subarc fields of length one degree of gantry motion (individual control points) and combined to be a single plan. However, this division of the trajectory into sub-fields would violate restrictions set by the VMAT optimization algorithm in the version of Eclipse (v.11) available at the NSCC. The restrictions are: the plan cannot contain more than ten arcs and the arcs can be no less than 30.1° of gantry rotation. The trajectory output by the algorithm must thus be additionally simplified to comply with these restrictions in order to be VMAT optimized.

The simplified trajectory, as generated by another program, is a plan that features ten arcs (the maximum accepted by the algorithm), eight of which are of gantry length 30.1° (with a 0.1° overlap in the range of gantry motion between these arcs) and two of which must be 60° , in order to complete the 360° gantry motion. By summing all the $E(c,g)$ values over the length of an arc at each couch position the minimum total for all the possible couch positions is chosen. The new trajectory is a radiotherapy plan with ten arcs containing ten separate fixed-couch positions, which are selected based on the weighted overlap map generated by *Equation 3.5*. The newly optimized plans represent the highest degree of granularity possible for use within the VMAT optimization algorithm. See *Figure 3.10* for an example of such a trajectory.

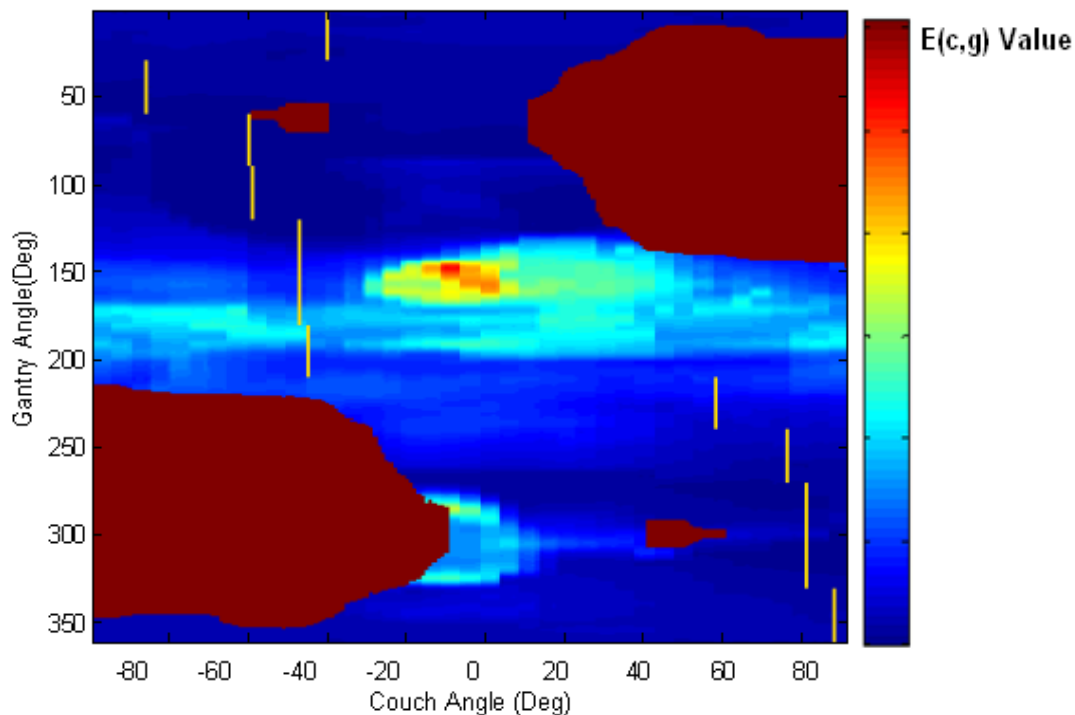


Figure 3.12: Simplified trajectory indicated as yellow lines, with the maximum couch motion able to comply with the Eclipse restrictions on VMAT Optimization.

3.5 Comparison of Conventional Trajectory to Optimized Trajectory

The technique is being tested via calculation on cranial cancer treatment plans due to the proximity of critical structures to the target volume. The geometry of cranial cases is such that the range of motion is maximized for full 4π approach of beams. The criteria for inclusion as a test patient in this study are cranial cases with more than a single fraction, in other words SRT patients. Thirty test-patients were chosen for the test-patient population based on personal communication with a statistician in the Department of Radiology, Queen Elizabeth II Health Sciences Centre. Twenty-nine of these patients were cranial cases, and one of them was extra-cranial hard palate but was treated with an SRT delivery. The PTV of the extracranial case was located such that the OARs were similar as for a cranial SRT case.

Once a clinical case has been identified, that patient's CT set, plan, and structure set are exported, anonymized using DicomCleaner (PixelMed Publishing) software, and then re-imported into Eclipse as a test patient. The test patient is given an ID number corresponding to the order in which they were analyzed. The anonymized radiation therapy plan DICOM file (RTPlan.dcm) and contoured structure information (RTStruct.dcm) are imported to MATLAB. The PTV is chosen from the list of contoured structures. An iterative loop is then run which analyzes the PTV and each of the OARs in the structure file and generates an overlap map similar to that seen in *Figure 3.3*. Each of these overlap maps is then applied the collision zones as measured for the cranial treatment position. The overlap maps for each OAR are then weighted according to *Equation 3.6* and combined to form a total weighted overlap map for all of the OARs. The total overlap map is then used to determine the ten subarcs (eight of 30.1° , two of 60° of gantry motion) each with unique couch positions that cover a total of 360° gantry rotation in the map with the least amount of overlap. This corresponds to the maximum amount of motion allowed by Eclipse for a plan to still be valid for acceptance by the VMAT optimization algorithm.

The customized plan is then imported to the test patient in Eclipse, along with the previously delivered clinical plan with conventional trajectory. The radiation prescription, plan normalization method, and VMAT optimization objectives were taken from the clinically delivered plan and applied to the optimized trajectory plan. The optimized trajectory test plan was then compared to the initial conventional treatment trajectory plan. At the NSCC, the conventional trajectory plans used one to four non-coplanar arcs, depending on location of PTV and OAR arrangement. The standard

template for conventional trajectory arc-based SRT includes a 360° arc (couch angle = 0°), two 180° arcs (couch angles = 45° and 315°), and an arc that traverses 150° to 355° (couch angle = 90°). All plans used a 6MV photon beam. The VMAT optimization is applied in three iterations. The duration of time for the optimization is similar between conventional and optimized trajectories. For each OAR, maximum and mean dose for both the conventional and optimized trajectories are compared. PTV coverage for both plans is set such that the 90% isodose curves cover 99.5% of the PTV volume. The dose homogeneity [22] and dose conformity [23] of the PTV are then compared between the conventional and optimized trajectories to measure the coverage of the target volume with respect to the prescription dose. The dose homogeneity is a ratio of the difference in dose to 5% of the target volume and 95% of the target volume to the prescription dose (*Equation 3.7*). The conformity metric examines the volume of the target covered by 95% of the prescription dose and divides this by the volume of the target (*Equation 3.8*).

$$HI = 100\% \times \frac{D_5 - D_{95}}{D_P} \quad (3.7)$$

$$CI = \frac{V_{90\%D}}{V_{PTV}} \quad (3.8)$$

The majority of the OARs in the patient sets tabulated below were contoured with a planned organ-at-risk volume (PRV) of 3 mm surrounding the structure. The description of these structures is inclusive of this margin. This PRV was used for all brainstem and chiasms and the majority of optical tracts and nerves. The majority of the eyes and lens' were contoured without the PRV margin. This additional margin was added in contouring stages for delivered treatment, not as a methodology in this work.

CHAPTER 4 RESULTS AND ANALYSIS

4.1 Sparing of Dose to OARs

The maximum and mean doses for each of the most critical OARs in the patient anatomy represented in percentage of the prescription dose are illustrated below (*Figures 4.1 and 4.2*) to illustrate an example of the information given from Eclipse one of the thirty calculated test-patients. This test patient was chosen as a best case example in order to highlight the degree to which our trajectory optimization can improve a dose distribution and spare the OARs. *Appendix A* features sagittal slices of the dose distributions comparing the conventional and optimized trajectories for all test patients. In addition, *Figures 4.3 and 4.4* show the percent reduction in maximum and mean dose, respectively, to each OAR after trajectory optimization averaged across all patients.

In order to consistently represent each of the patient cases equivalently, the dose reduction is represented in percent of prescription dose as opposed to absolute for *Figures 4.1 – 4.4*. Representing these values in absolute dose would skew the results as the prescription doses for treatments vary significantly among the thirty-patient population.

The error bars are the standard error of mean due to the population being less than one hundred [20]:

$$SE = \frac{\sigma}{\sqrt{N}} \quad (4.1)$$

$$\sigma = \sqrt{\frac{1}{N} \sum_{i=1}^N (x_i - \mu)^2} \quad (4.2)$$

where σ is the sample standard deviation, N is the sample size, and μ is the mean.

Figure 4.5 shows the percent change in the maximum dose averaged across all OARs for each test patient after trajectory optimization. To establish some metric for the overall effect of applying the optimized trajectory, the change in dose for every OAR in a patient anatomy was averaged to gauge whether or not, as a whole, the effect of the technique was a reduction or increase. While this metric is susceptible to outlying values skewing this average, these values are normalized to the OAR doses from the clinically delivered plan with the conventional trajectories in order to attempt to manage this bias. Each bar in the plot indicates one patient and a positive percent reduction (bar above the x-axis) indicates an improved sparing to all OARs on average in that patient plan.

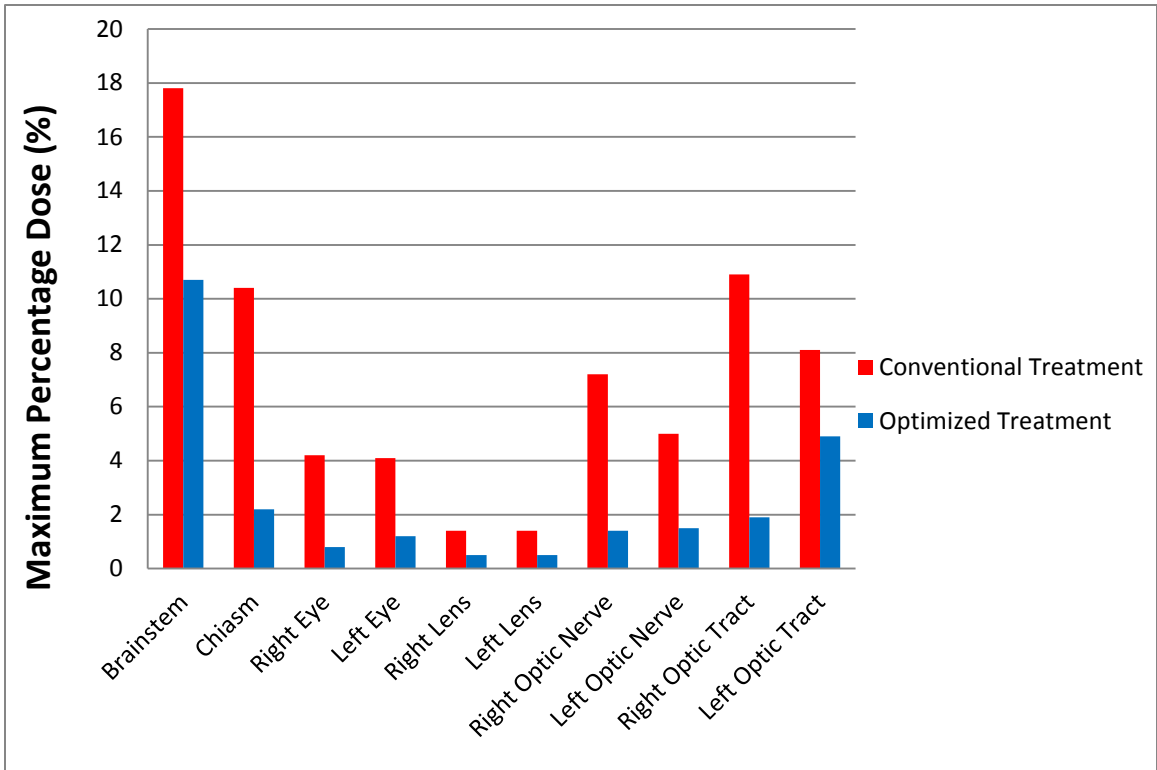


Figure 4.1: Maximum dose for a cranial test patient shown for both conventional and optimized trajectories.

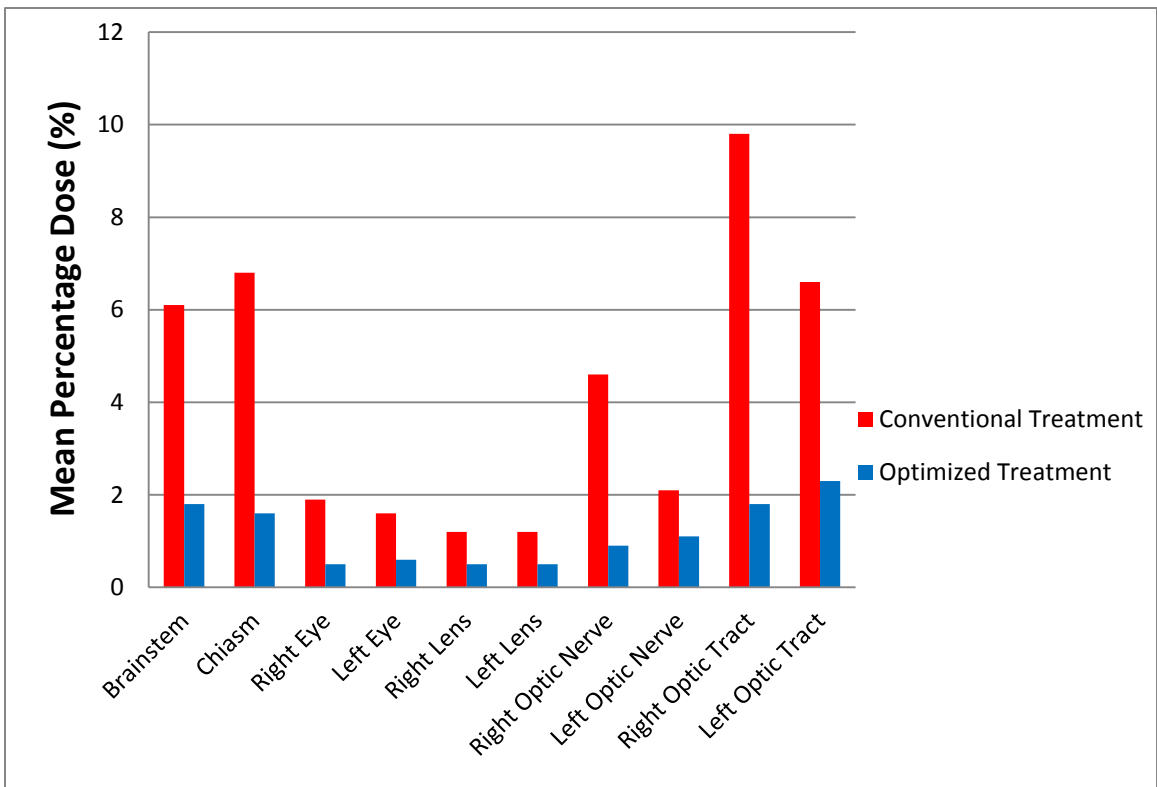


Figure 4.2: Mean dose for a cranial test patient shown for both conventional and optimized trajectories.

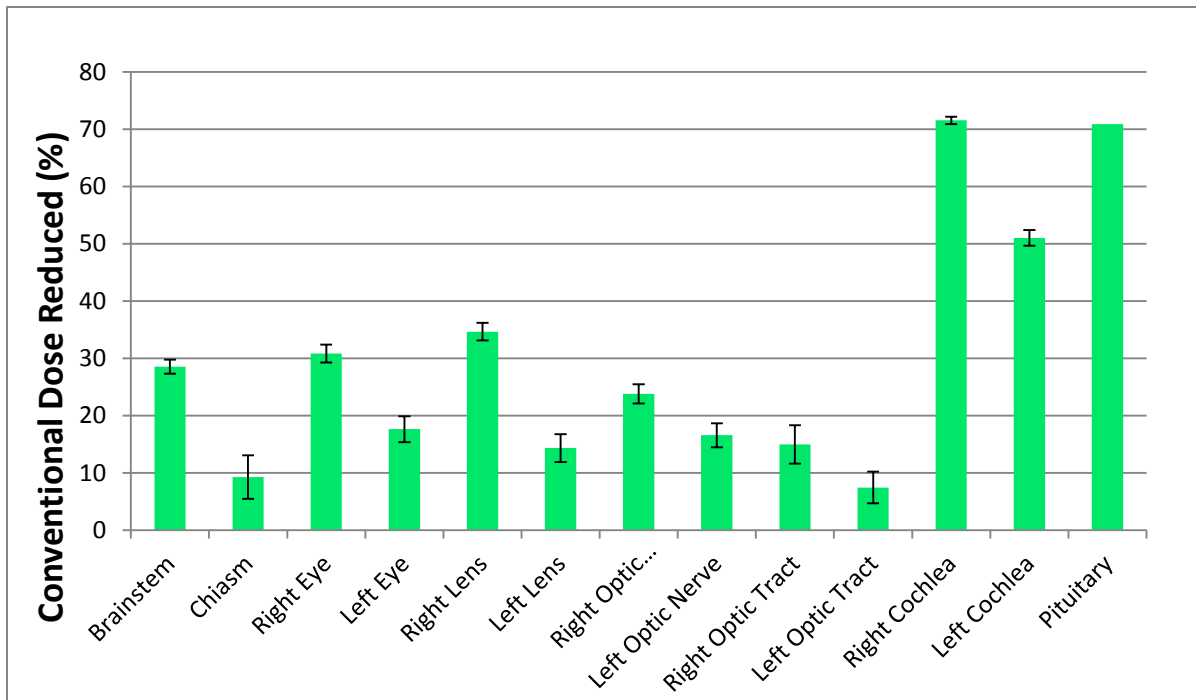


Figure 4.3: Mean dose reduction for entire patient population (N = 30). The lack of error bar on the pituitary data is due to the fact that only one case had a contoured pituitary.

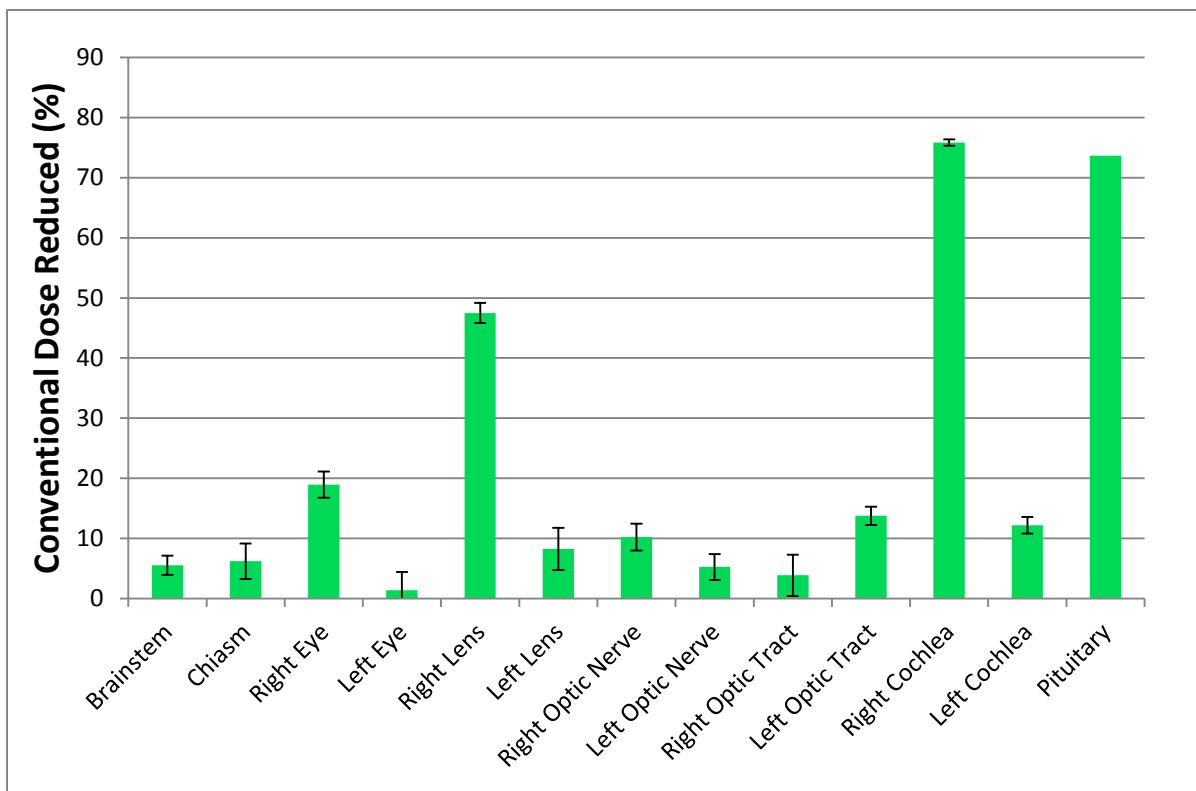


Figure 4.4: Maximum dose reduction for entire patient population (N = 30). The lack of error bar on the pituitary data is due to the fact that only one case had a contoured pituitary.

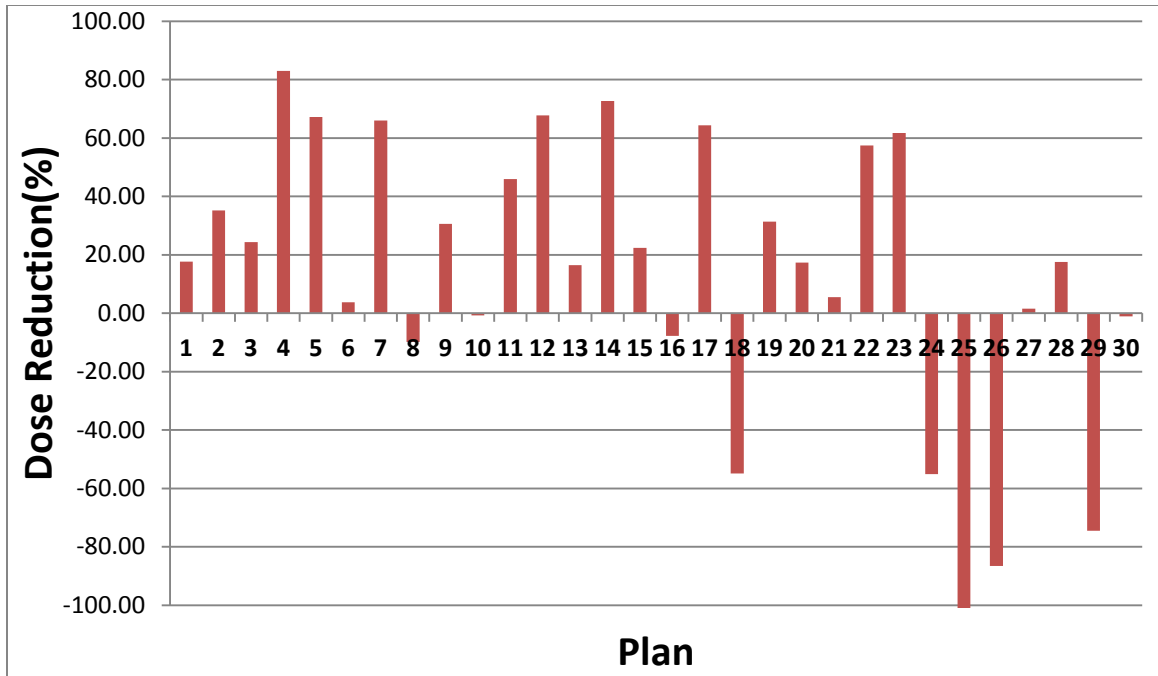


Figure 4.5: Average maximum doses across all OARs for all the plans in the patient set.

If we examine the cases in this plot that were not immediate successes (those with negative percent dose reduction, i.e. dose to OARs on average increase after trajectory optimization in either the maximum dose values, as shown in *Figure 4.5*, or mean dose values (not shown), we hope to identify a characteristic within this subset of the patient population that may require the use of a different set of dose constraints to maintain target coverage and minimize dose to OARs.

Assuming that the subset of the population with percent changes below the horizontal axis possess a characteristic which requires further analysis, we can examine these subsections of the population separately. Examining the reduction to dose from conventional to optimized trajectories in the same way as conducted in *Figures 4.3 and 4.4*, we can generate the plots in *Figure 4.6, 4.7, 4.8 and 4.9*. *Figure 4.6 & 4.7* are the reduction values in the OARs for the patient population (N = 20) which were

immediately successful using the dose constraints taken from publications [2] and [3].

Figure 4.8 & 4.9 are the reduction values in the OARs for the patient population ($N = 10$) which were not successful using these dose constraints.

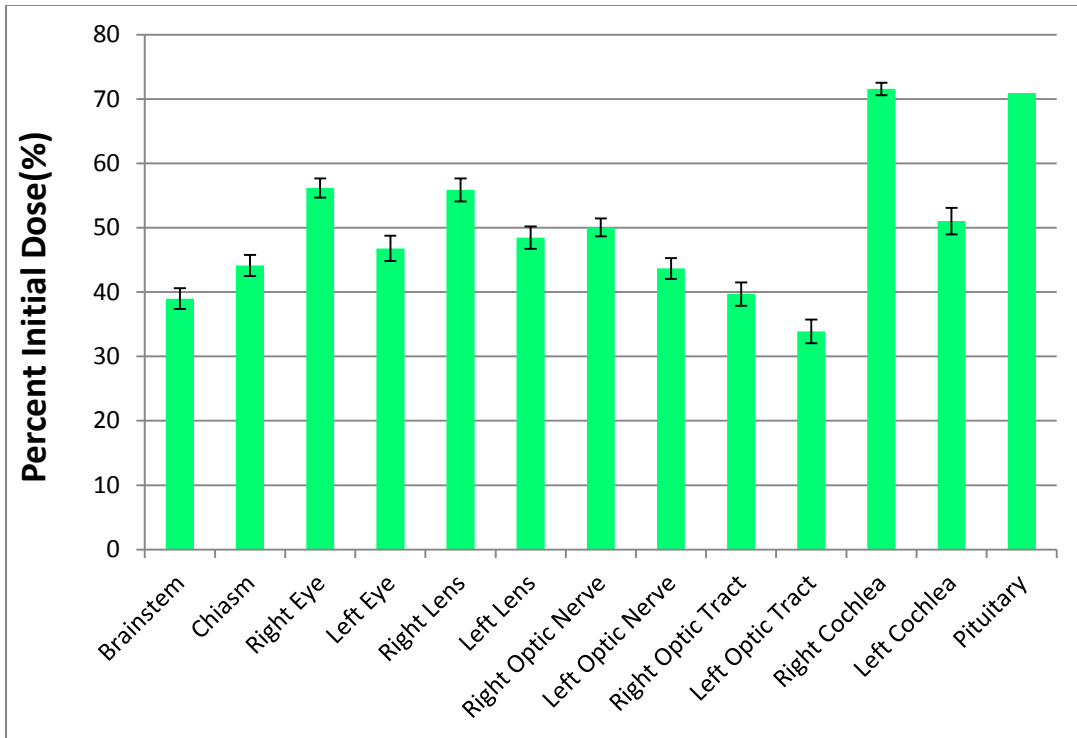


Figure 4.6: Mean dose reduction for subset of cases which were immediately successful during implementation of technique. (N = 20)

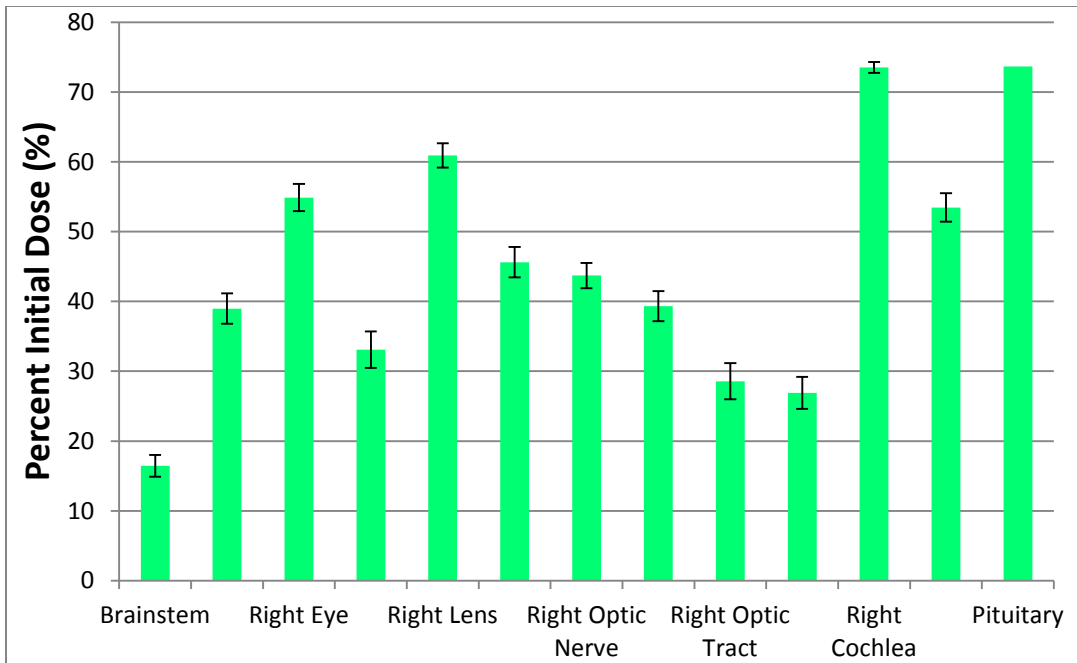


Figure 4.7: Maximum dose reduction for test-patient population subset of patients which were immediately successful upon implementation of technique. (N = 20)

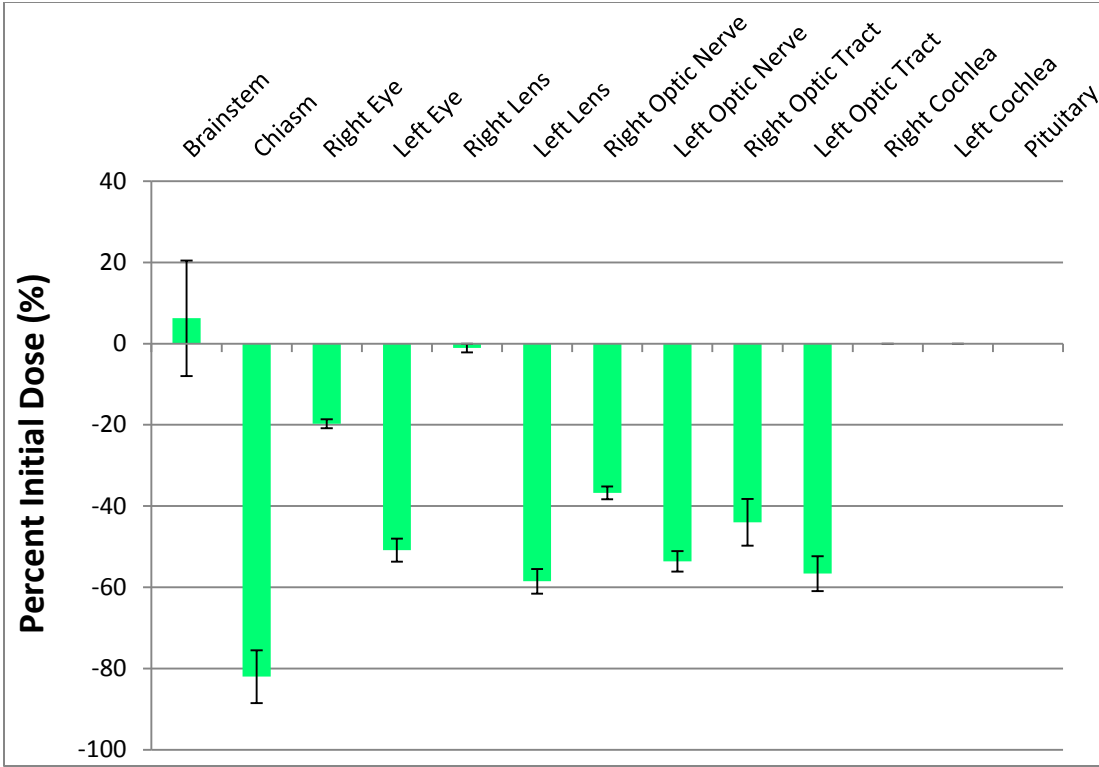


Figure 4.8: Mean dose reduction for subset of cases which were worsened improved during implementation of technique. (N = 10)

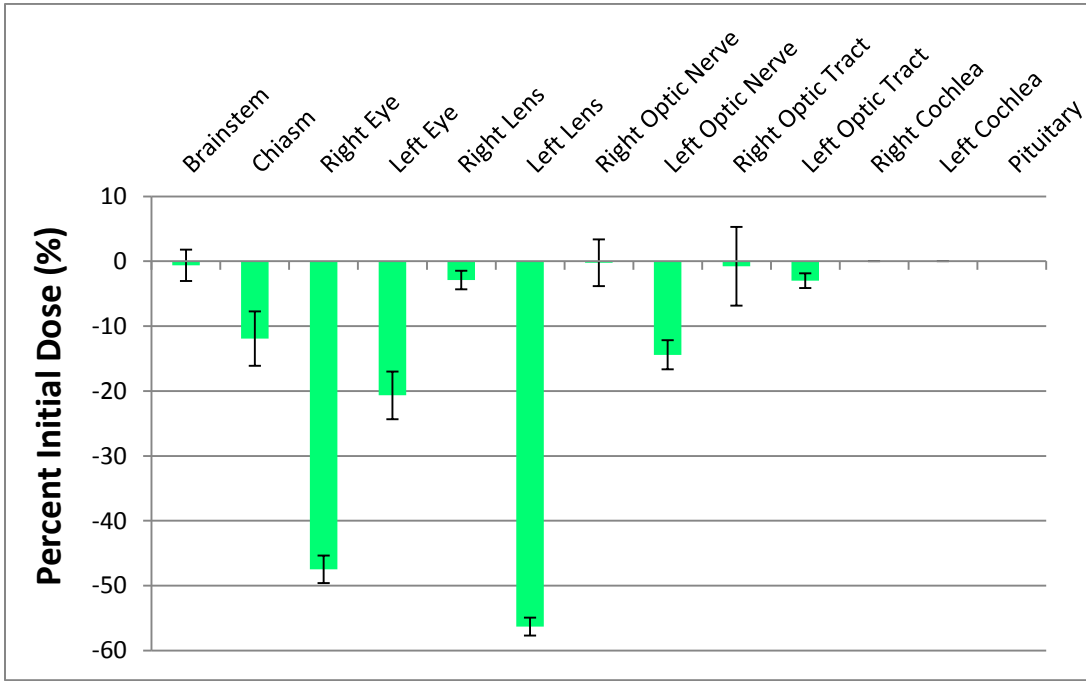


Figure 4.9: Maximum dose reduction for subset of cases which were worsened during implementation of technique. (N = 10)

In order to determine if there is a statistically significant difference between the OAR dose in the optimized trajectory plan as compared to the conventional trajectory plan, a Wilcoxon rank-sum test [20] was applied to the maximum (*Table 4.1*) and mean dose (*Table 4.2*) data for the full (N = 30) patient population. This test was chosen due to the fact that it is valid for any distribution, normal or not, as opposed to the two-sampled *t*-test. In addition, this non-parametric alternative is much less sensitive to single outliers than the *t*-test, which is based solely on the order in which observations from the two samples fall. The test does assume that the data are paired and come from the same population and that each pair is chosen randomly, which is true for our case. [20]

Table 4.1: *p*-values for each of the maximum doses to OARs as calculated by the Wilcoxon rank-sum test (N = 30).

OAR	<i>p</i>-value
Brainstem	0.15
Chiasm	0.086
Right Eye	0.00012*
Left Eye	0.1
Right Lens	1.10E-05*
Left Lens	0.003*
Right Optic Nerve	0.001*
Left Optic Nerve	0.015*
Right Optic Tract	0.02*
Left Optic Tract	0.013*
Right Cochlea	2.60E-06*
Left Cochlea	0.15

*statistically significant at $p < 0.05$.

Table 4.2: p -values for each of the mean doses to OARs as calculated by the Wilcoxon rank-sum test (N = 30).

OAR	p -value
Brainstem	0.0062*
Chiasm	0.0023*
Right Eye	0.00045*
Left Eye	0.0005*
Right Lens	0.000052*
Left Lens	0.005*
Right Optic Nerve	0.004*
Left Optic Nerve	0.0075*
Right Optic Tract	0.0022*
Left Optic Tract	0.019*
Right Cochlea	0.0035*
Left Cochlea	0.18

*statistically significant at $p < 0.05$.

In addition, the same rank sum test was generated for the subsection patient population of immediately successful cases (Tables 4.3 and 4.4).

Table 4.3: p -values for each of the maximum dose OARs as calculated by the Wilcoxon rank-sum test (N = 20).

OAR	p -value
Brainstem	0.42
Chiasm	0.018*
Right Eye	0.00021*
Left Eye	0.067
Right Lens	0.00030*
Left Lens	0.0036*
Right Optic Nerve	0.006*
Left Optic Nerve	0.059*
Right Optic Tract	0.0052*
Left Optic Tract	0.0066*
Right Cochlea	0.0020*
Left Cochlea	0.15

*statistically significant at $p < 0.05$.

Table 4.4: p -values for each of the mean dose OARs as calculated by the Wilcoxon rank-sum test ($n = 20$).

OAR	p -value
Brainstem	0.05*
Chiasm	0.011*
Right Eye	0.00094*
Left Eye	0.0073*
Right Lens	0.00066*
Left Lens	0.0049*
Right Optic Nerve	0.012*
Left Optic Nerve	0.05*
Right Optic Tract	0.00049*
Left Optic Tract	0.00036*
Right Cochlea	0.035*
Left Cochlea	0.18

*statistically significant at $p < 0.05$.

4.2 Dose Homogeneity and Conformity to Target Volume

The result of this assessment for all patients in the patient set ($N = 30$) resulted in a mean dose homogeneity of $5.48\% \pm 0.76\%$ for conventional trajectory plans and $6.14\% \pm 0.67\%$ for optimized trajectory plans (Wilcoxon rank-sum test $p = 0.780$). The mean dose conformity was 1.11 ± 0.02 for conventional trajectory plans and 1.18 ± 0.03 for the optimized trajectory plans (Wilcoxon rank-sum test $p = 0.964$).

4.3 VMAT Optimization Effect on Dose Sparing

The VMAT optimization functions to minimize unwanted dose to healthy tissues, to ensure coverage of dose to the specified target volume, and to enforce dose homogeneity in the target volume. As this is also the objective of the optimized trajectory, the result of dose sparing may be the result of the versatility of the VMAT optimization algorithm and not the optimized trajectory. While the same dose objectives were applied to both treatments, the apertures featured in these trajectories offer different BEV conditions for the VMAT optimization to address. As such, the optimized trajectory could be supplying this VMAT optimization with a trajectory which may facilitate

effective sparing OARs through the VMAT optimization process itself, but not inherently geometrically improved in terms of overlap.

To investigate this possibility, an optimized trajectory plan was calculated without any OAR dose objectives in the VMAT optimization, allowing the algorithm to prioritize PTV coverage alone. Thus, differences in OAR sparing should be attributed primarily to the differences in arc trajectories. Normal tissue optimization was kept on during this optimization.

This method was only conducted for one randomly chosen cranial test-patient cases. DVH comparisons of the conventional trajectory treatment plan, the optimized trajectory plan with VMAT dose objectives for the OARs, and the optimized trajectory plan without VMAT dose objectives for the OARs objectives are shown in *Figures 4.8, 4.9, and 4.10* for the left eye, the right eye, and the coverage of the target volume for that cranial cancer case. The HI and CI for these plans are presented in *Table 4.5*. Sparing for all OARs is shown in *Figure 4.11* for this test case.

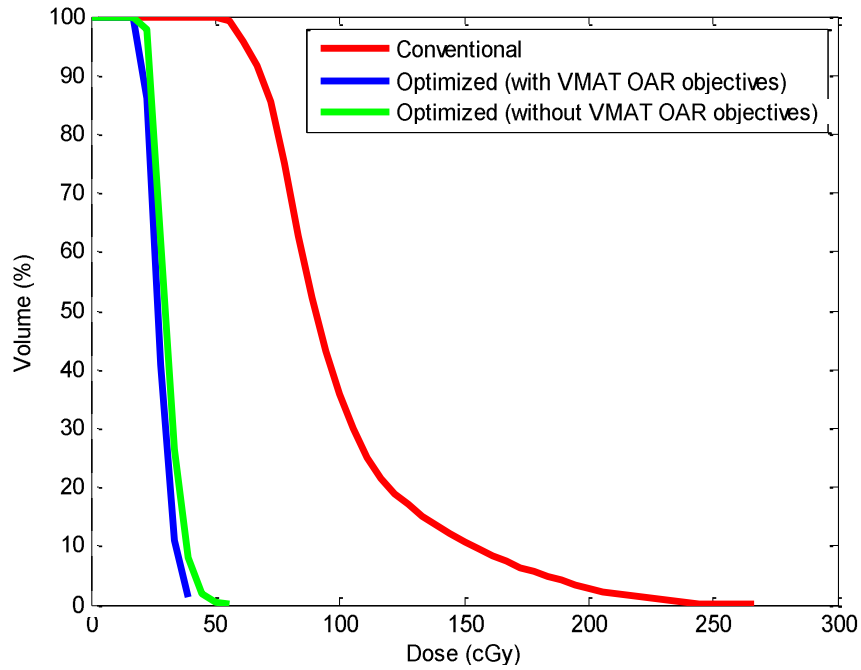


Figure 4.10: DVH for the right eye. Blue curve indicates the dose according to the optimized trajectory with 30° subarcs, red curve indicates conventional trajectory, and green curve is the same as the optimized trajectory, but with all VMAT dose sparing objectives removed.

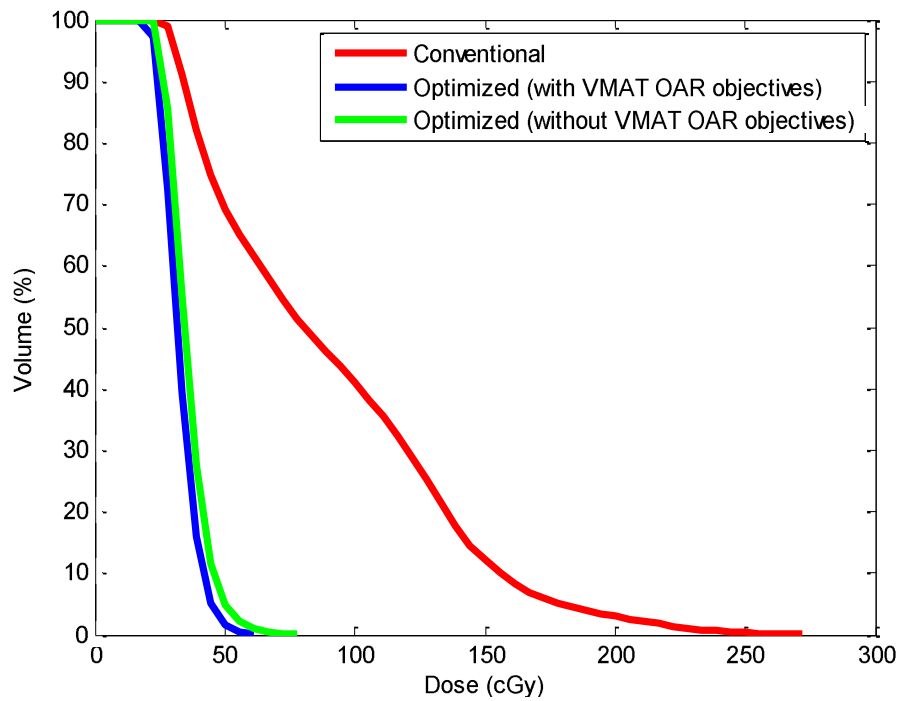


Figure 4.11: DVH for the left eye. Blue curve indicates the dose according to the optimized trajectory with 30° subarcs, red curve indicates conventional trajectory, and green curve is the same as the optimized blue trajectory, but with all VMAT dose sparing objectives removed.

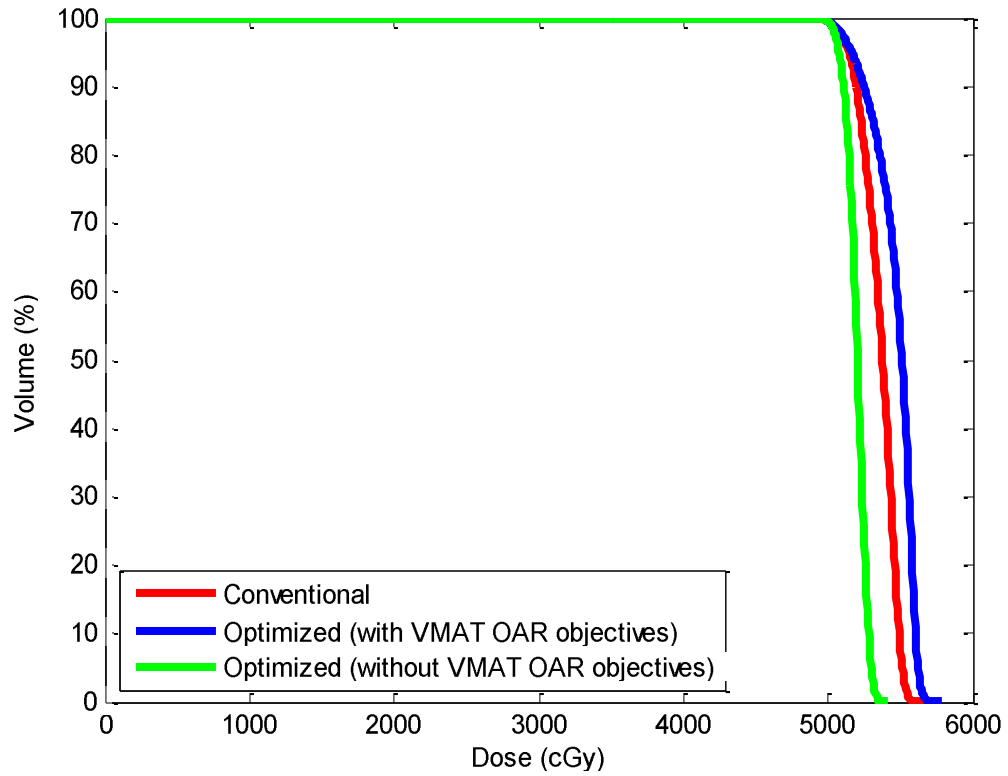


Figure 4.12: DVH for the PTV. Blue curve indicates the dose according to the optimized trajectory with 30° subarcs, red curve indicates conventional trajectory, and green curve is the same as the optimized trajectory, but with all VMAT dose sparing objectives removed.

Table 4.5: Values for dose homogeneity and conformity indices for the conventional trajectories, optimized trajectories with OAR sparing objectives, and optimized trajectory with the OAR sparing objectives removed

PLAN	HI	CI
Conventional	7.36	1.05
Optimized (with VMAT OAR objectives)	9.14	1.07
Optimized (without VMAT OAR objectives)	4.94	1.47

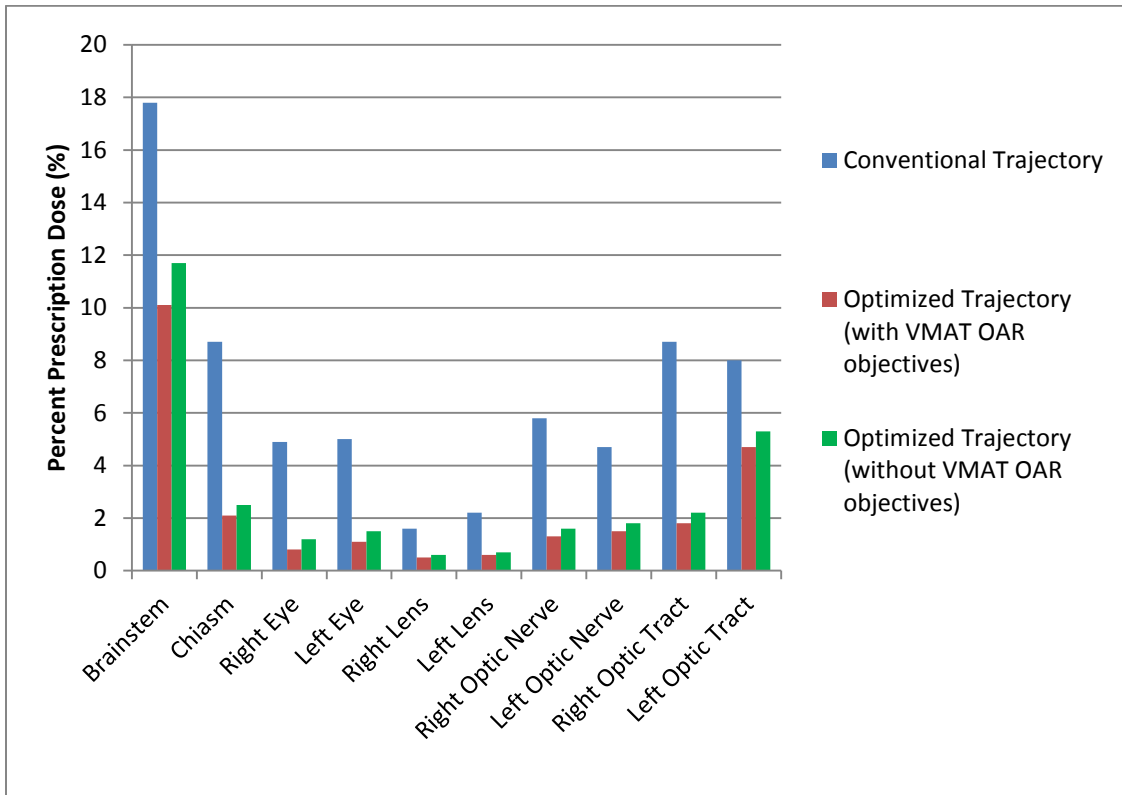


Figure 4.13: Maximum dose values for all OARs in the test patient structure for conventional trajectory, optimized trajectory and optimized trajectory without OAR objectives in the VMAT optimization. This data is for the same patient as shown in Figure 4.1.

CHAPTER 5 DISCUSSION

5.1 Sparing of Dose to OARs

For the majority of patients analyzed we can observe that the optimized trajectory results in a dose reduction to each OAR as compared to the conventional trajectory. The Wilcoxon analysis indicates an excellent correlation ($p < 0.05$) of rejection of the null hypothesis (that both samples are equivalent) for the majority of the OARs examined in the patient population. Although a few of the OARs (brainstem, chiasm, left eye) have p -values greater than 0.05, over this patient population when examining the maximum dose, the mean dose has excellent correlation for all but one of the OARs (left cochlea). In addition, this result improved further when examining the cases that do not require further review (i.e. modification of organ weighting values). When examining the averages for all OARs across all patients, the doses have lowered for all sensitive structures in cranial SRT patients for both mean and maximum dose. Represented in percentage of initial doses, to control the variability among prescription doses, the implementation of this technique increases the protection of sensitive organs by preferentially selecting treatment angles which limit overlap between PTV and OAR. When using published doses constraints to define organ weighting, the majority of our patient set improved in sparing quality. Referring to *Figures 4.3 and 4.4*, the average maximum dose was found to decrease by 12% and average mean dose by 19% with implementation of an optimized trajectory. With the removal of cases that were not immediate successes, referring to *Figures 4.6 and 4.7* (keeping in mind these cases require further analysis in order to weight the OARs appropriately and create trajectories which suit their clinical scenario) these numbers increase to 40% and 46%, respectively.

The cases which were not included in the group of patients within the population that showed improvement ($N = 10$) are plotted in terms of average change in dose as a result of implementation of the technique in *Figures 4.8 and 4.9*. From these plots we can see that all but one of these OARs shows negative improvement or no change at all in these cases with implementation of the technique. Also, based on the error bars within these plots, there is not a high variability in the worsening of these OARs. This means that these plans worsened across all OARs when the technique was applied, and was not simply the result of a single OAR lowering the average reduction in *Figure 4.5*. When we examine the cases that require further review, we find that in all of these cases ($N = 10$) the PTV was anterior to the brainstem and posterior to the eyes. This suggests that with this particular scenario of PTV placement, the OAR weighting needs to be altered to include this increased risk of dose. In *Equation 3.6*, a lower dose constraint could be used for a value of D_{tot} to increase the overlap weighting for OARs at higher risk of exposure. This is likely the cause of the failure of some OARs to indicate significant correlation ($p > 0.05$) during the Wilcoxon-Rank Sum Test. We speculate that once the dose constraints are modified to more accurately represent the circumstances of the anatomical arrangement, this scenario will also be improved by the technique.

5.2 Comparison of Results to *Yang et al*

When looking at the improvement in dosimetric results to OARs according to the metric used in *Yang et al.* (subtracting the dose differences in percent prescription dose) we can see that our technique reduced doses to OARs going from conventional VMAT trajectory to the optimized trajectory by a larger value for the brainstem, eyes, lenses, and cochleae (columns four and five in *Table 5.1*). This is especially so in the comparison to

the maximum doses to the eyes which worsened on average with the application of the trajectory optimization technique in Yang *et al.* Additionally, our results are for a patient population of thirty randomly chosen cranial cases, while there were only ten in Yang *et al* [1]. The sparing is worse for chiasm and optic nerves in our technique. The average reduction to OARs was 1.9 for our technique and 1.6 in Yang *et al.*

Table 5.1: Average dose values for OARs compared to those available in Yang *et al* [1]. All dose values are in percent prescription dose.

	Conventional Trajectory	Optimized Trajectory	Improvement	Improvement (Yang <i>et al</i> [1] data)
Brainstem Dmax	50.3 ± 7.2	47.5 ± 7.1	2.8	1.1
Brainstem Dmean	16.3 ± 3.4	13.6 ± 3.5	2.7	2.3
Chiasm Dmax	25.2 ± 6.5	23.6 ± 6.4	1.6	1.6
Chiasm Dmean	16.3 ± 4.5	14.9 ± 4.6	1.4	2.6
Eye Dmax	6.9 ± 2.1	6.3 ± 0.8	0.5	-0.3
Lens Dmax	2.8 ± 0.5	2.0 ± 0.3	0.8	0.5
Optic Nerve Dmax	20.2 ± 11.6	18.6 ± 2.7	1.6	2.3
Optic Nerve Dmean	9.9 ± 2.7	8.7 ± 2.7	1.2	2.9
Cochlea Dmax	20.2 ± 4.2	16.3 ± 3.0	3.9	1.4
Cochlea Dmean	14.9 ± 3.0	12.6 ± 3.2	2.3	1.9
Average			1.9	1.6

Furthermore, this comparison should be additionally normalized for the existence of variations in the doses to OARs in the conventional VMAT trajectories. Percent reduction value changes in magnitude when we consider what value the OAR had initially. The values from *Table 5.1* are properly normalized to account for this value in *Table 5.2*.

Table 5.2: Average dose values for OARs compared to those available in Yang *et al* [1]. All dose values are in percent prescription dose normalized to the conventional dose.

	Improvement	Improvement (Yang <i>et al</i>[1] data)
Brainstem Dmax	5.6	1.1
Brainstem Dmean	16.6	4.0
Chiasm Dmax	6.2	2.0
Chiasm Dmean	8.7	4.0
Eye Dmax	7.9	-1.3
Lens Dmax	27.0	9.4
Optic Nerve Dmax	7.7	3.9
Optic Nerve Dmean	12.1	8.6
Cochlea Dmax	19.2	2.6
Cochlea Dmean	15.5	4.7
Average	12.7	1.6

Normalizing these improvements in terms of reduction of the conventional dose delivered represents the percent change in doses properly. From this we can see that our technique was superior in reducing doses to sensitive tissues for our patient population, across all OARs that were available for comparison from those tabulated in Yang *et al* [1]. Our selection of patient population was guided solely by the use of stereotactic radiotherapy in a cranial cancer case. We do not, however, know the details of the indications used to select the patients used in Yang *et al*. This creates some inconsistencies in this comparison as they may have had a patient population with more difficult cases to plan in terms of sparing of OARs.

5.3 Dose Homogeneity and Conformity to Target Volume

The implementation of the technique appeared to have little effect on the homogeneity of the target volume, and even less of an effect on the conformity of the target volume. While the majority of optimized plans had a slightly worsened

homogeneity, there is good correlation as shown with the Wilcoxon analysis. Any differences seen in homogeneity and conformity are not relevant in comparison to the dose sparing to sensitive organs. This is a promising confirmation that the technique, while very effective in decreasing doses to OARs in cranial cancer cases, does not compromise the objectives of the radiotherapy treatment of the target volume.

5.4 VMAT Optimization Effect on Dose Sparing

The results in *section 4.3* indicate that the effects in dose sparing improvement seen in this particular cranial patient cannot be attributed to the VMAT optimization. When the OAR dose objectives were removed for the VMAT optimization and the VMAT algorithm was asked to only focus on target homogeneity, the sparing effects did not significantly change. This indicates that in this particular case, the motion of the trajectory was responsible for the majority of the differences in doses to sensitive tissues. This improvement is the result of utilizing the information gained by the geometric overlap map and implementing it to a patient specific treatment. The VMAT optimization's OAR sparing objectives are responsible for a negligible portion of the OAR sparing.

In terms of the homogeneity of the target coverage, it seems that when the VMAT optimization was allowed to prioritize this coverage, this homogeneity improves (referring to *Table 4.5*, HI decreased from 7.36 to 4.94) in comparison to the conventional trajectory. This is a logical observation because the optimization now has the freedom to improve the coverage without the need to make any alterations based on sparing of OARs. However, when all sparing objectives are removed, it appears that conformity of target coverage worsened to a value of 1.47. This is likely due to the lack of OAR constraints, as the presence of OAR constraints would have forced the high dose

isodoses to conform closer to the PTV in order to meet dose gradient constraints between the PTV and the OARs.

The findings shown in *Figure 4.13* are in no way an indication that a conformally, PTV-shaped beam aperture, such as those seen in dynamic conformal arc (DCA) treatments, would suffice as a substitute for VMAT treatment. All objectives regarding homogeneity of target coverage are still used in this optimization and result in the improved homogeneity index shown in *Table 4.5*. If a DCA plan was used in its place, the homogeneity would be far worse for this treatment plan, as DCA does not control for dose homogeneity.

Even though this is only one test case, it is reasonable to expect this result to the other test patients with similar anatomical arrangements if the optimization trajectory in the other test patients has minimized overlap to a similar degree. If a test patient does not have minimum overlap of the same degree, then it is reasonable to assume the exclusion of OAR sparing objectives may not produce be to the same degree of success as this test patient.

CHAPTER 6 CONCLUSION AND FUTURE WORK

6.1 Conclusion

The creation of radiotherapy trajectories based on the minimization of overlap between OARs and PTV is an effective means to increase dose sparing in the majority of cranial cancer treatment. In a test-patient population study of thirty cranial SRT patients, the average mean dose reduction to OARs was approximately 19% and the average maximum dose reduction to OARs was approximately 12% of the initial dose given in the treatment of these patients. The majority of cases showed reduction of dose to OARs upon utilization of this trajectory optimization technique with the standard published organ constraints used for weighting in the overlap maps, however a small subset of patients require reweighting and further analysis. Considering only patient cases that were deemed immediately successful with the general OAR weighting, the mean dose reduction increased to 46% and the maximum dose reduction increased to 40%. The trajectory optimization and sparing of OARs has little to no impact on homogeneity and conformity of dose coverage to the target volume.

The effects of sparing the OARs can be attributed directly to the trajectory designed via the overlap reduction model and trajectory algorithm, as can be seen by removing OAR dose objectives from the VMAT optimization for a test case, the result being a dosimetrically better treatment plan when compared to a conventional trajectory treatment plan and also dosimetrically equivalent to the plan with OAR dose objectives included.

We have made improvements to the geometric overlap equation initially illustrated by Yang *et al* in 2011. These include the reduction of the size of the collision

zones in the overlap map to correspond to reasonable assessment of expected collision as opposed to avoiding an entire quadrant of the overlap map, the creation of a factor to account for the presence of a foreground vs. background overlap and appropriately weight the overlap score value, and the OAR weighting scheme according to published dose constraints concerning the OARs within the treatment region of the patient. Each of these have proven to be effective enhancements in the creation of a cost equation approach to avoiding sensitive structures. In addition, a unique algorithm was developed for navigation of the overlap map in order to generate an optimized trajectory of delivery of arc-based SRT plans. In direct comparison of our results to those from Yang *et al*, we show that the addition of these factors was beneficial in the reduction in dose to sensitive structures. The results illustrated for our thirty-patient population, particularly those for which the general dose constraints seem to be an appropriate method of organ weighting, indicate substantial advancements to a novel delivery technique.

6.2 Future Work

From the results of this study it is clear that a fraction of the patient population analyzed benefited from the implementation of this technique. However, a number require possible further refinement in construction of the overlap map in order to achieve the same results. The OAR weighting scheme was chosen according to published dose constraints regarding maximum dose, however this seems to only work for a fraction of patients planned with optimized trajectories for SRT. Identifying the anatomical arrangements of PTV with respect to OAR for patients suitable for this weighting scheme, as well as identifying other possible organ weightings suitable for a variety of

cases is a vital next step. A patient population that is homogeneous in terms of diagnosis would help to understand the effects of altering the OAR dose constraints.

In addition, the optimization algorithm was built without specificity to treatment site. This optimization algorithm provided with the appropriate OAR dose weighting could readily be applied to several anatomical sites. One restriction that is foreseen in this additional application is the potential for much greater collision zones in the overlap map. The physical arrangement for treatment of cranial cases allows the use of the end of the couch, which benefits the limitation of couch and gantry collision. Other treatment sites that warrant investigation include head-and-neck, lung stereotactic body radiotherapy (SBRT), pancreas SBRT, and liver SBRT. Based on initial investigations, the use will be limited in head-and-neck due to the large size of head-and-neck PTVs which severely limit the possible degrees of couch motions that are available for a trajectory.

The newly available Developer Mode on Varian TrueBeam linacs allows the creation of customized XML radiotherapy plans and for the experimental implementation of some of the optimized trajectories described in this work. Developer Mode allows users to execute treatment plans with multiple simultaneous axes of motion on the linac, including gantry and couch. The newly available Veritas [21] program can be used to create XML plans from DICOM format and simplify their delivery, or can be used to aid in the creation of plans. Additionally, Eclipse now incorporates the ability to run user-defined programs, which could incorporate the types of algorithms described here. In order to implement this type of technique or any associated trajectory using Varian software, Eclipse treatment planning software must first enable the ability to perform a VMAT optimization on a treatment trajectory without restrictions involving length of

subarc or the presence of couch motion. With these new advancements, the increased use of this type of iterative optimization process for increased couch motion becomes increasingly feasible.

BIBLIOGRAPHY

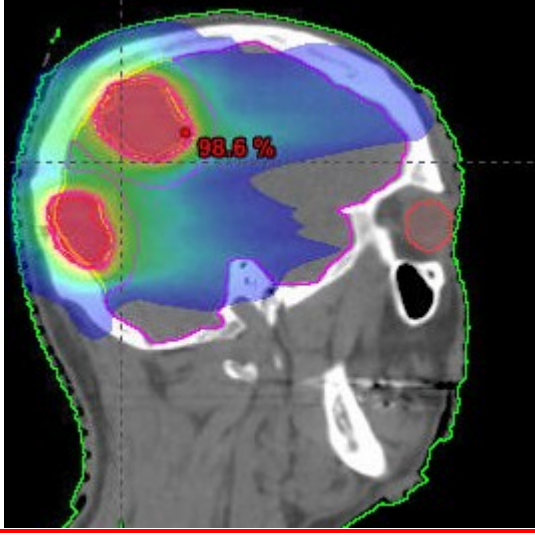
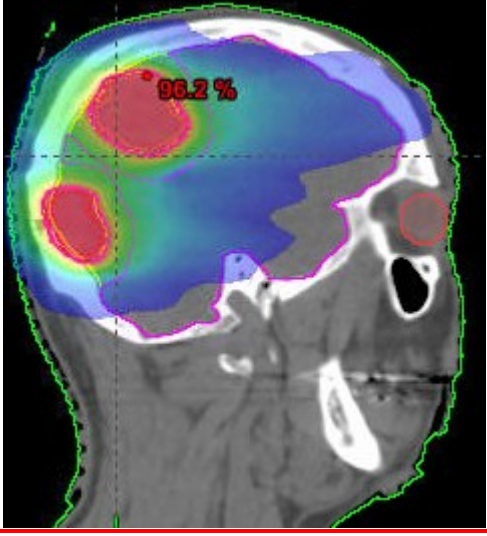
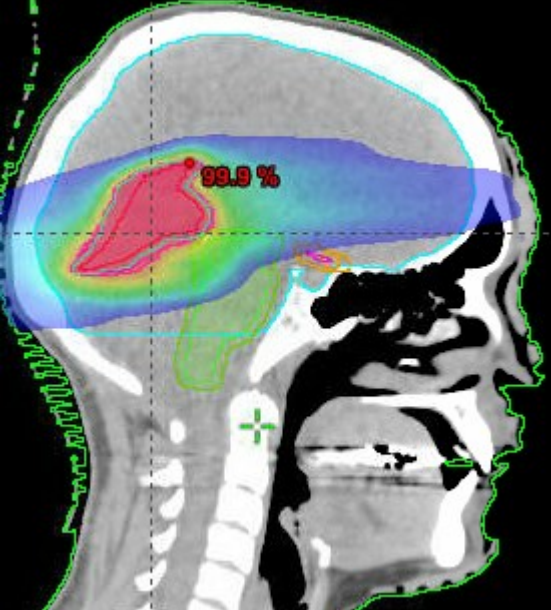
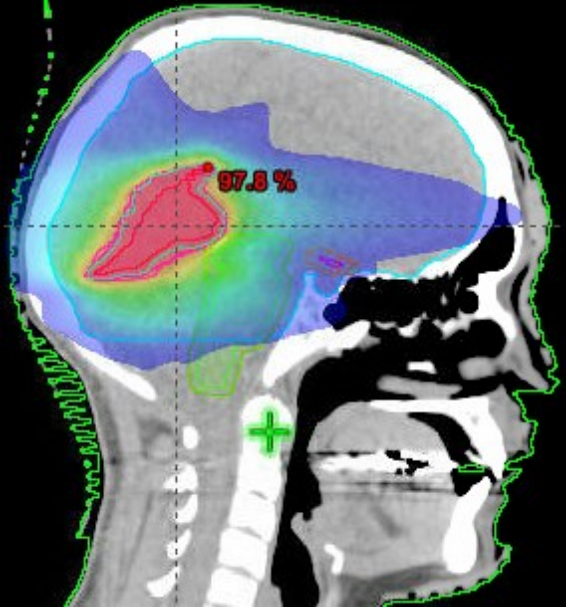
1. Yang et al. "Choreographing Couch and Collimator in Volumetric Modulated Arc Therapy." *International Journal of Radiation Oncology, Biology, Physics* 80, no. 4 (July 15, 2011): 1238–47. doi:10.1016/j.ijrobp.2010.10.016.
2. Bentzen, Søren M., Louis S. Constine, Joseph O. Deasy, Avi Eisbruch, Andrew Jackson, Lawrence B. Marks, Ten Haken, Randall K., and Ellen D. Yorke. "Quantitative Analyses of Normal Tissue Effects in the Clinic (QUANTEC): An Introduction to the Scientific Issues." *International Journal of Radiation Oncology * Biology * Physics* 76, no. 3 (March 1, 2010)
3. Hall, Eric J., and Amato J. Giaccia. *Radiobiology for the Radiologist*. Lippincott Williams & Wilkins, 2006.
4. E.B. Podgorsak, *Radiation Oncology Physics: A Handbook for Teachers and Students*. (IAEA, 2005).
5. F.H. Attix. *Introduction to Radiological Physics and Radiation Dosimetry*. Wiley-VCH, 2004.
6. F.M. Kahn. *The Physics of Radiation Therapy, 4th Edition*. Lippincott Williams and Wilkins, 2003.
7. Canadian Cancer Society Website. General cancer statistics for 2013. <http://www.cancer.ca/>, 2014.
8. Smyth, Gregory, Jeffrey C Bamber, Philip M Evans, and James L Bedford. "Trajectory Optimization for Dynamic Couch Rotation during Volumetric Modulated Arc Radiotherapy." *Physics in Medicine and Biology* 58, no. 22 (November 21, 2013): 8163–77. doi:10.1088/0031-9155/58/22/8163.
9. Rodrigues, Anna, Fang-Fang Yin, and Qiuwen Wu. "Dynamic Electron Arc Radiotherapy (DEAR): A Feasibility Study." *Physics in Medicine and Biology* 59, no. 2 (January 20, 2014): 327–45. doi:10.1088/0031-9155/59/2/327.
10. Fahimian, Benjamin, Victoria Yu, Kathleen Horst, Lei Xing, and Dimitre Hristov. "Trajectory Modulated Prone Breast Irradiation: A LINAC-Based Technique Combining Intensity Modulated Delivery and Motion of the Couch." *Radiotherapy and Oncology: Journal of the European Society for Therapeutic Radiology and Oncology* 109, no. 3 (December 2013): 475–81. doi:10.1016/j.radonc.2013.10.031.

11. Popescu, Carmen C, Wayne A Beckham, Veronica V Patenaude, Ivo A Olivotto, and Maria T Vlachaki. "Simultaneous Couch and Gantry Dynamic Arc Rotation (CG-Darc) in the Treatment of Breast Cancer with Accelerated Partial Breast Irradiation (APBI): Feasibility Study." *Journal of Applied Clinical Medical Physics / American College of Medical Physics* 14, no. 1 (2013): 4035
12. Shaitelman, Simona F, Leonard H Kim, Di Yan, Alvaro A Martinez, Frank A Vicini, and Inga S Grills. "Continuous Arc Rotation of the Couch Therapy for the Delivery of Accelerated Partial Breast Irradiation: A Treatment Planning Analysis." *International Journal of Radiation Oncology, Biology, Physics* 80, no. 3 (July 1, 2011): 771–78. doi:10.1016/j.ijrobp.2010.03.004.
13. Van Heteran et al. Patent No.: US 8,588,369 B2 – Radiation System with Rotating Patient Support.
14. Varian Medical Systems Inc., *Eclipse Algorithms Reference Guide*, December 2011.
15. Otto, Karl. "Volumetric Modulated Arc Therapy: IMRT in a Single Gantry Arc." *Medical Physics* 35, no. 1 (January 1, 2008): 310–17. doi:10.1118/1.2818738.
16. Parsons, David (Personal Communication, May 2013.)
17. Cancer Research UK Website: The history of radiotherapy, 2014.
<http://www.cancerresearchuk.org/cancer-info/cancerandresearch/all-about-cancer/what-is-cancer/treating-cancer/history-of-radiotherapy/radiotherapy3>
18. Chin, Lawrence S. *Principles and Practice of Stereotactic Radiosurgery*. Springer 2008.
19. NRCC Report PIRS-701: The EGSnrc Code System: Monte Carlo Simulation of Electron and Photon Transport, I. Kawrakow and D.W.O. Rogers; Nov 7, 2003.
20. Fay Michael P., Proshan, Michael A. "Wilcoxon-Mann-Whitney or t-test? On assumptions for hypothesis tests and multiple interpretations of decision rules." *Statistics Surveys Volume 4 (2010) 1-39*. April 2010.
21. P Mishra, J Lewis, T Etmektzoglou, M Svatos, Brigham & Women's Hospital, Harvard Medical School, Boston, MA, Varian Medical Systems, Palo Alto, CA, 2013
<http://radiotherapyresearchtools.com/veritas/>
22. Oliver, Mike, Jeff Chen, Eugene Wong, Jake Van Dyk, and Francisco Perera. "A Treatment Planning Study Comparing Whole Breast Radiation Therapy against Conformal, IMRT and Tomotherapy for Accelerated Partial Breast Irradiation." *Radiotherapy and Oncology: Journal of the European Society for Therapeutic*

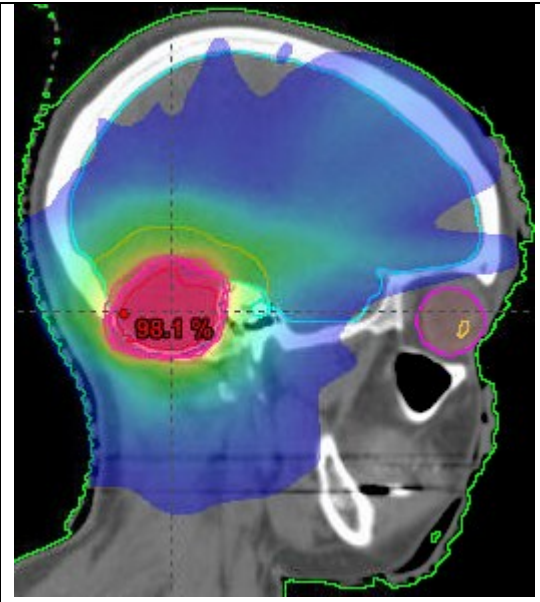
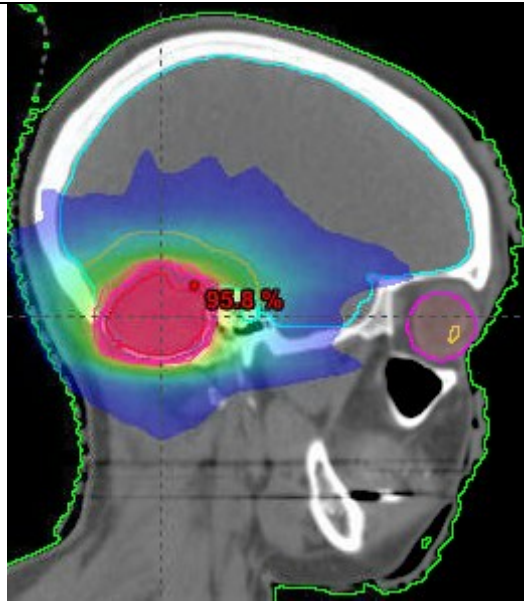
Radiology and Oncology 82, no. 3 (March 2007): 317–23.
doi:10.1016/j.radonc.2006.11.021.

23. Wu, Qiuwen, Radhe Mohan, Monica Morris, Andrew Lauve, and Rupert Schmidt-Ullrich. “Simultaneous Integrated Boost Intensity-Modulated Radiotherapy for Locally Advanced Head-and-Neck Squamous Cell Carcinomas. I: Dosimetric Results.” *International Journal of Radiation Oncology*Biology*Physics* 56, no. 2 (June 1, 2003)
24. Almond, Peter R, Biggs, Peter J., Coursey, B.M., Hanson, W.F., Huq, M. Saiful, Nath, Ravinder, Rogers, D.W.O. “AAPM’s TG-51 protocol for clinical reference dosimetry of high-energy photon and electron beams. *Medical Physics, Volume 26, September 1999.*
25. Veldeman L, Madani I, Hulstaert F. et al. Evidence behind use of intensity-modulated radiotherapy: A systematic review of comparative clinical studies. *Lancet Oncology* 2008; 9(4):367–375. Erratum in: *Lancet Oncology* 2008; 9(6):513. [PubMed Abstract]
26. Cancer Council South Australia Website. Radiotherapy linear accelerator. 2014
<http://www.cancersa.org.au/information/a-z-index/radiotherapy-for-skin-cancer>
27. C. J. Karzmark, “Medical Electron Accelerators.” *Medical Physics* 20, no. 3 (May 1, 1993)
28. McNair, A. “ICRU Report 33 - Radiation Quantities and Units Pub: International Commission on Radiation Units and Measurements, Washington D.C. USA Issued 15 April 1980, pp.25.” *Journal of Labelled Compounds and Radiopharmaceuticals* 18, no. 9 (September 1, 1981): 1398–1398. doi:10.1002/jlcr.2580180918.
29. Varian Truebeam System Manual, 2012-2013
www.variantruebeam.com/pdf/TrueBeam_Brochure.pdf

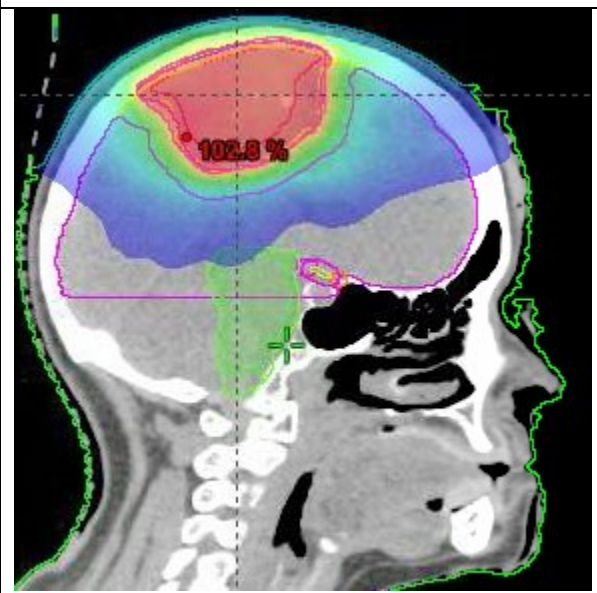
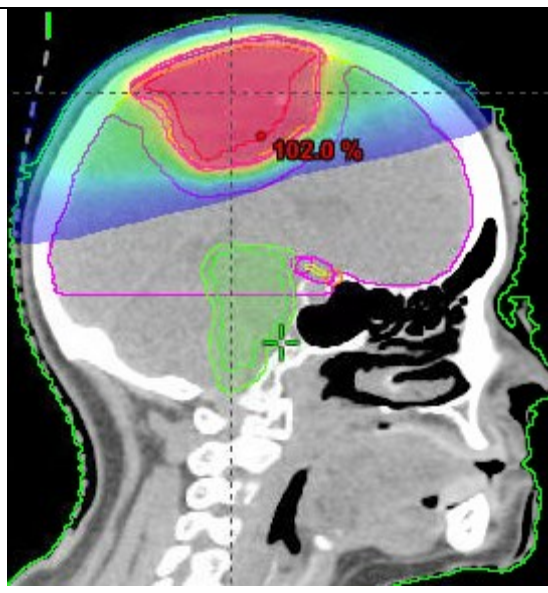
APPENDIX A Comparison of Dose Distributions

Case	Optimized Trajectory	Conventional Trajectory
T20136		
T20137		

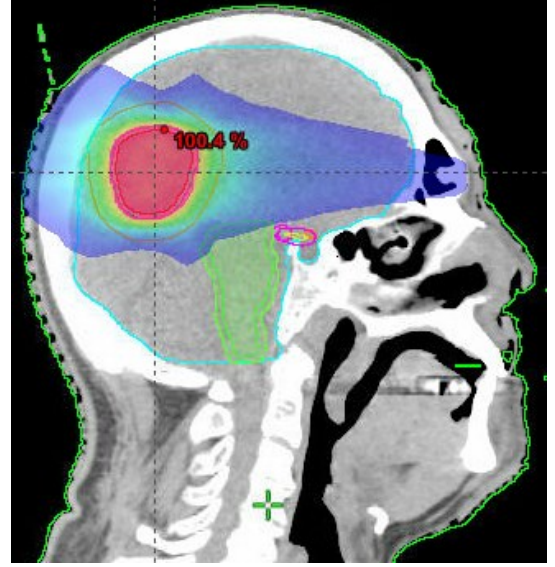
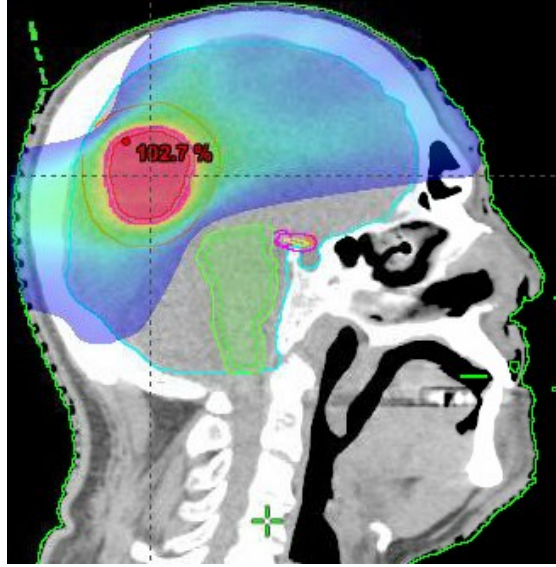
T20138



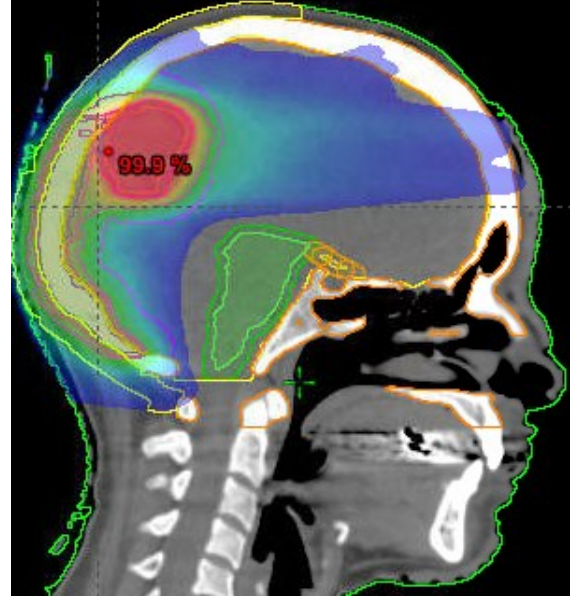
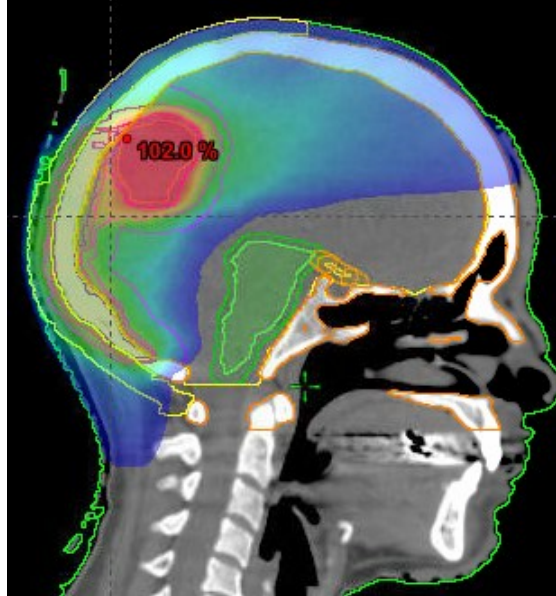
T20139

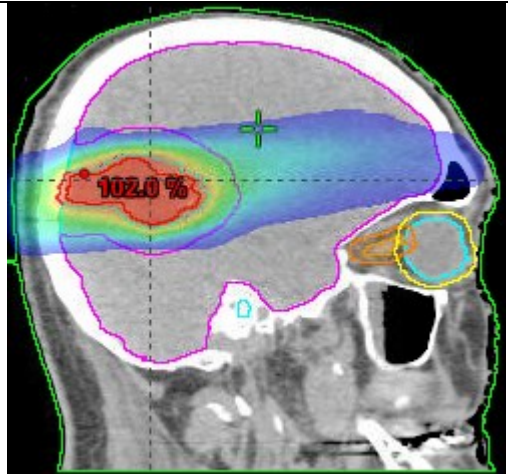
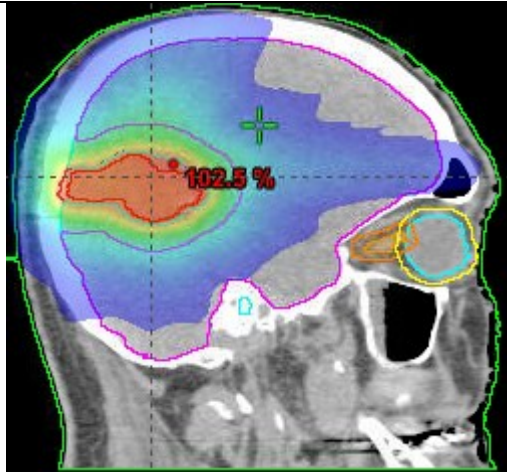
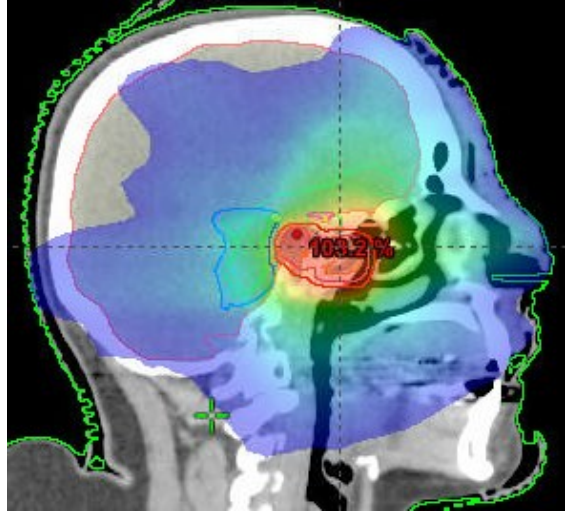
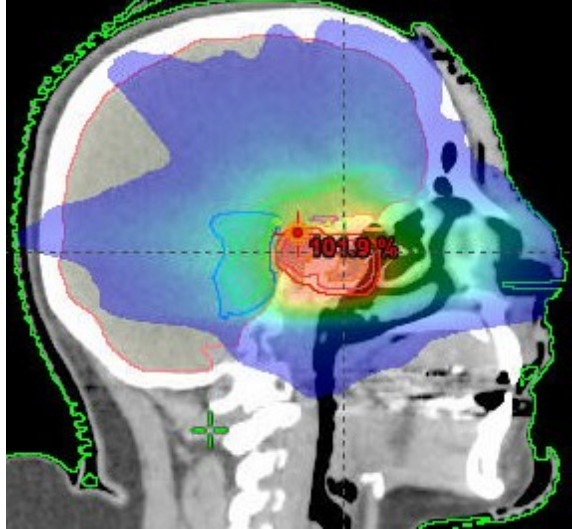
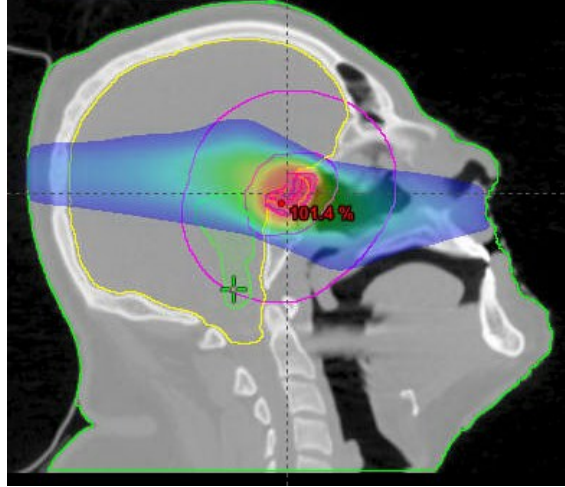
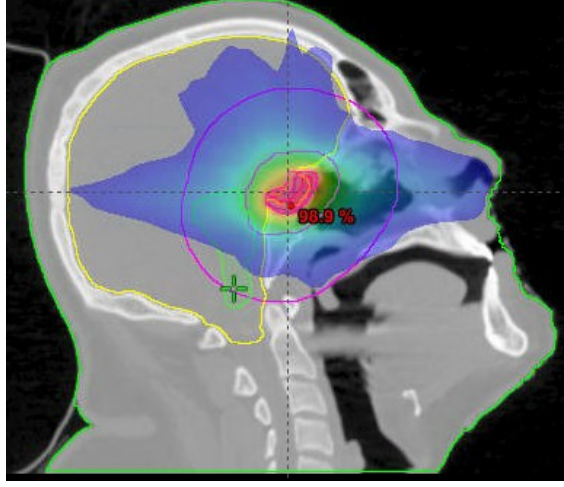


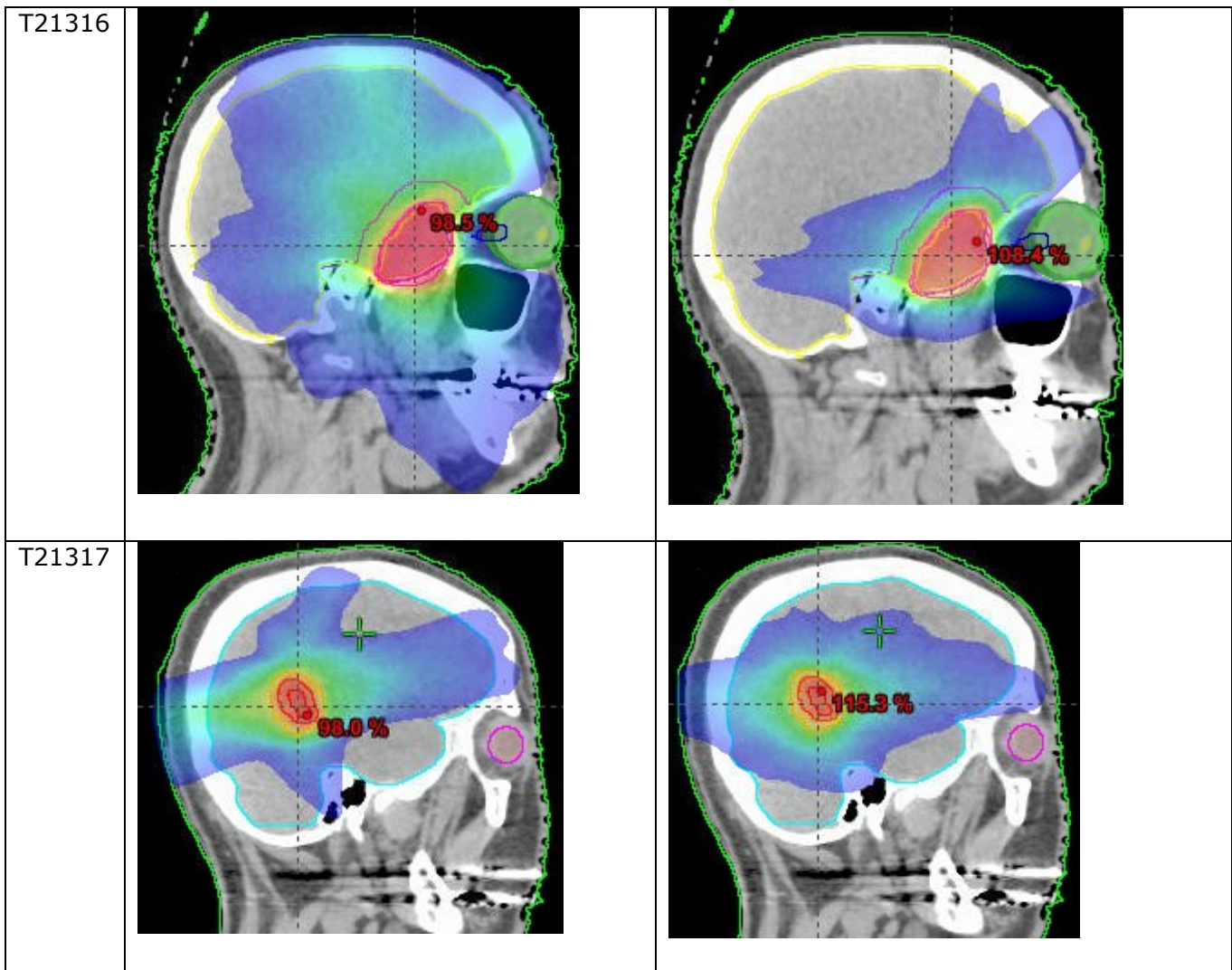
T21310



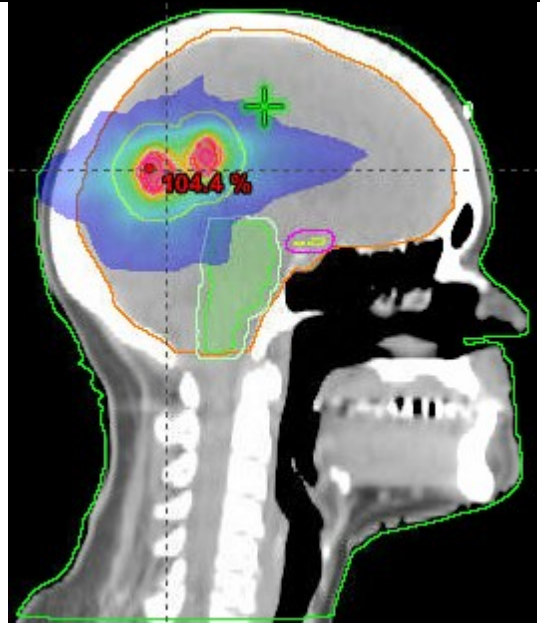
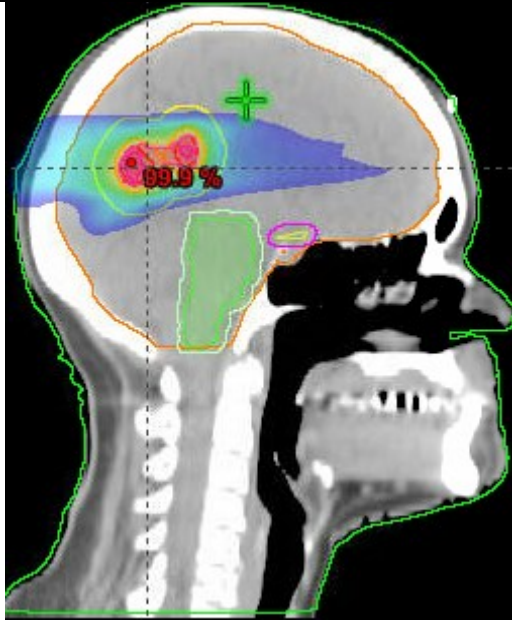
T21312



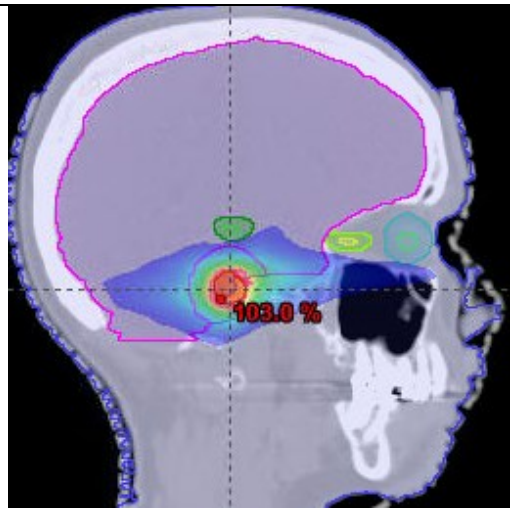
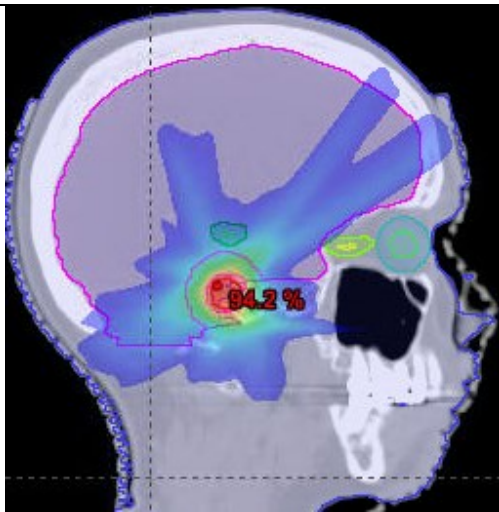
T21313		
T21314		
T21315		



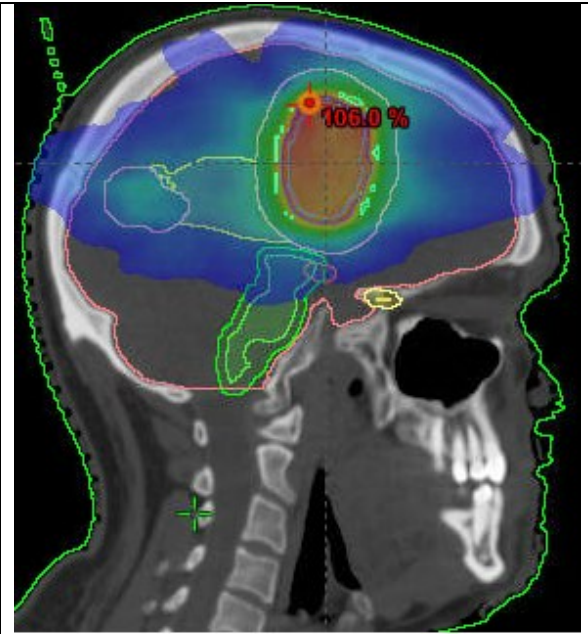
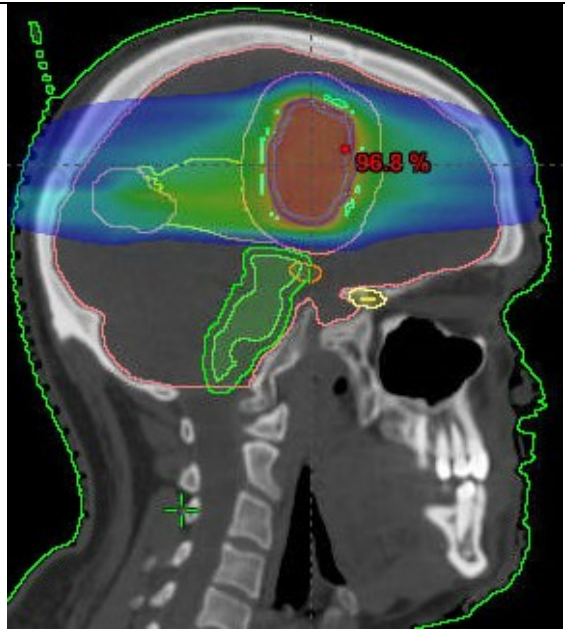
T21318



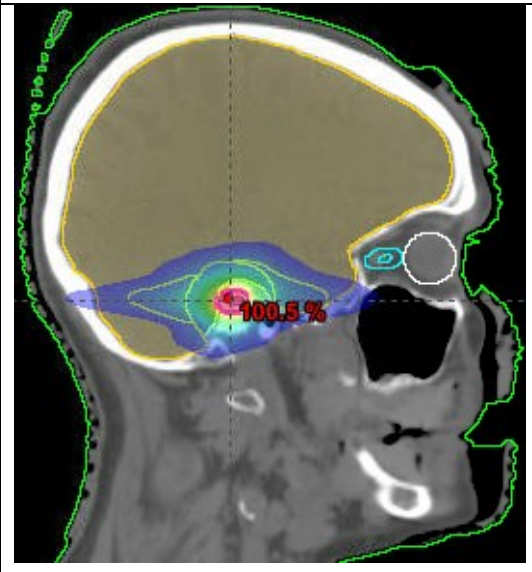
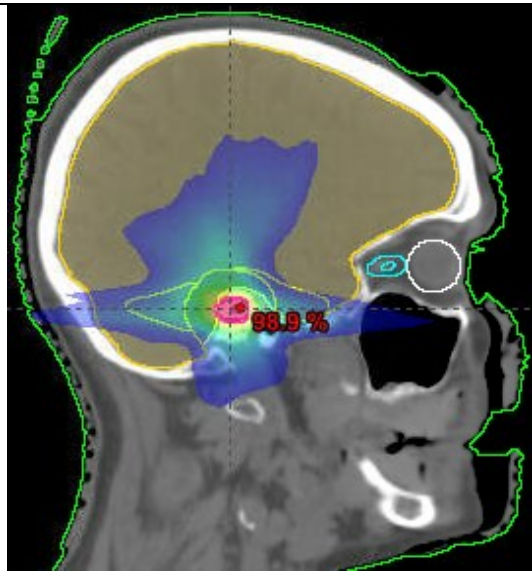
T21319

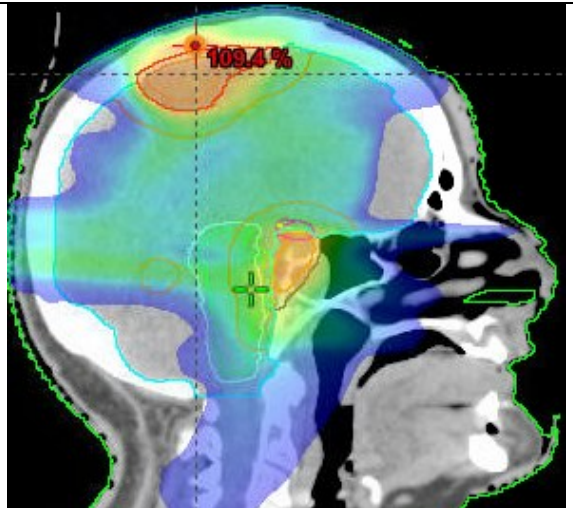
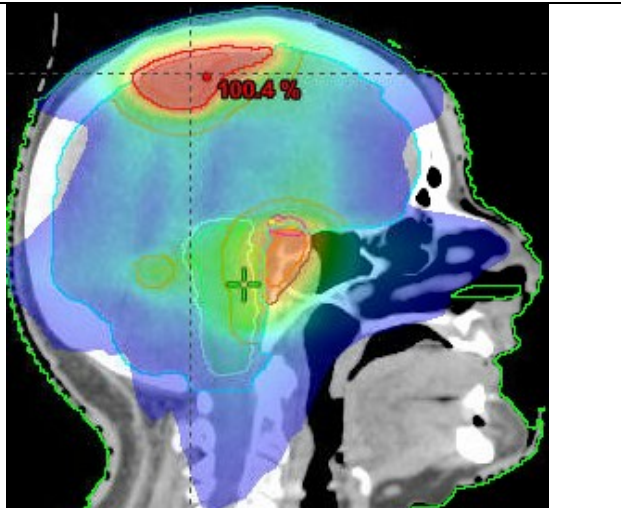
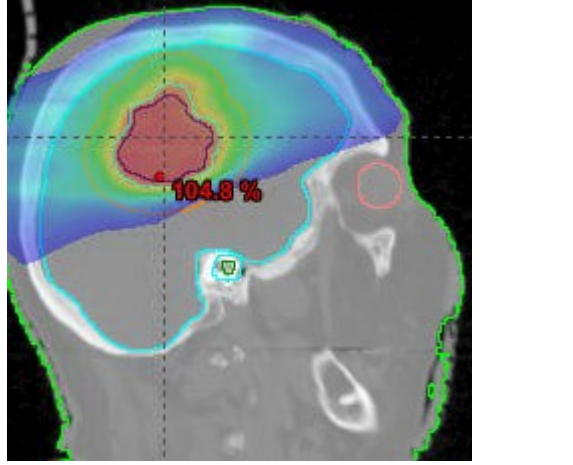
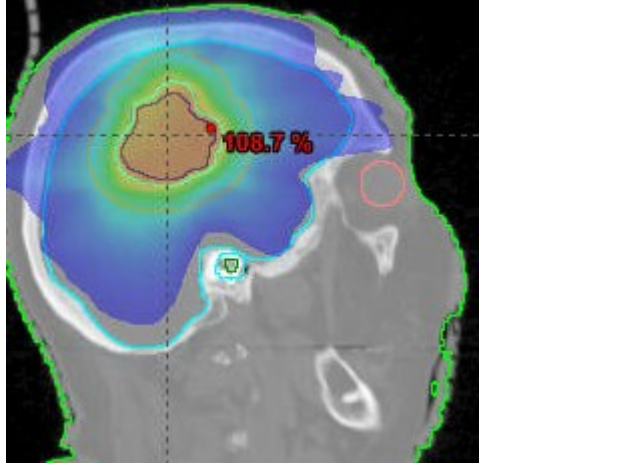
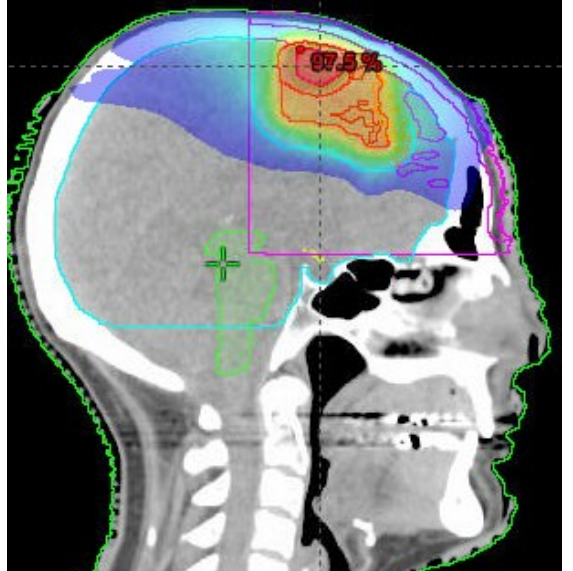
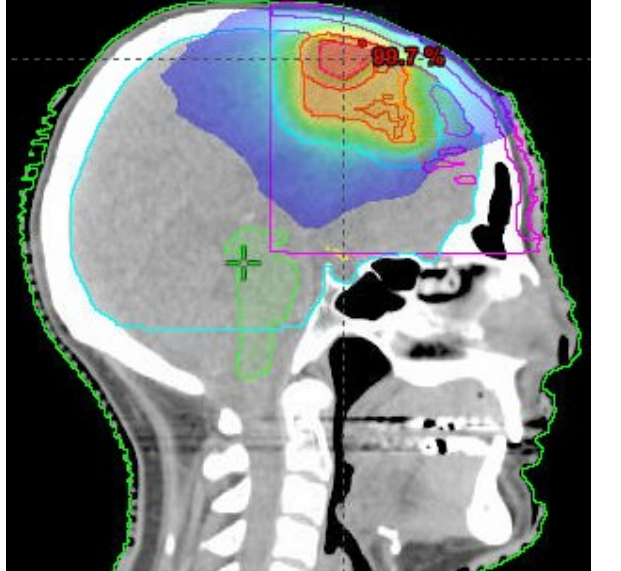


T21320

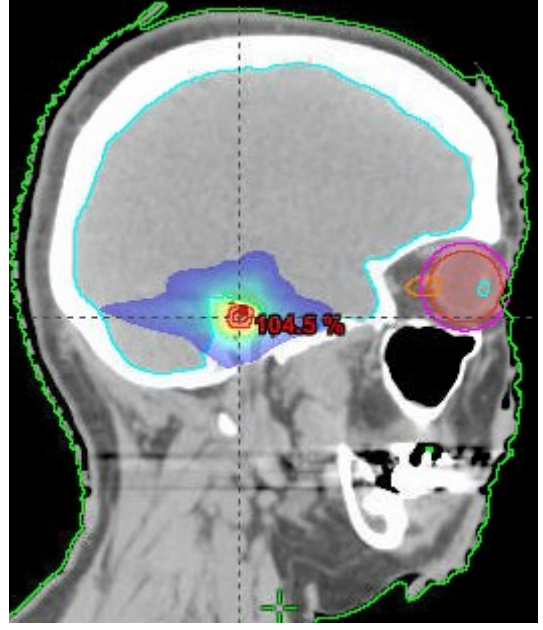
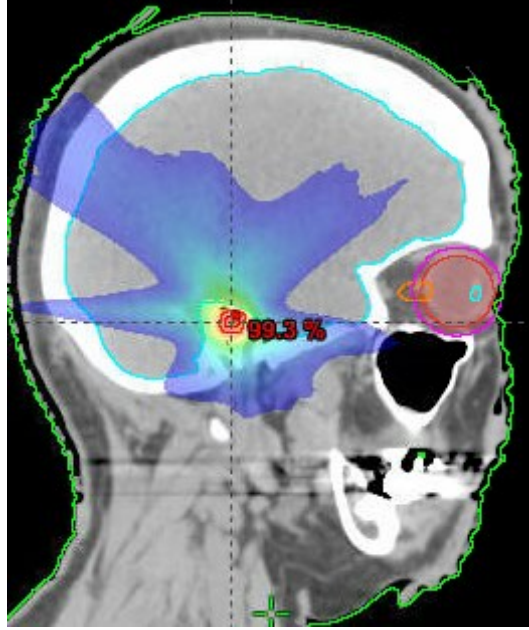


T21321

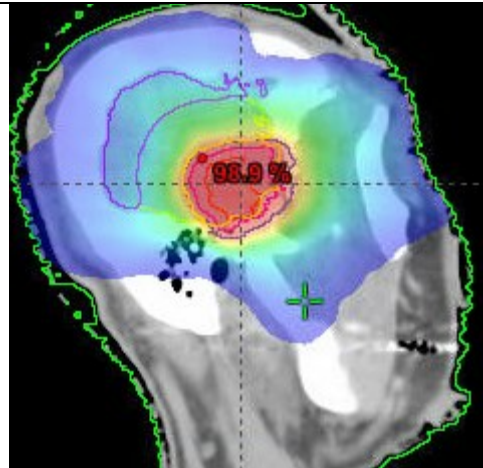
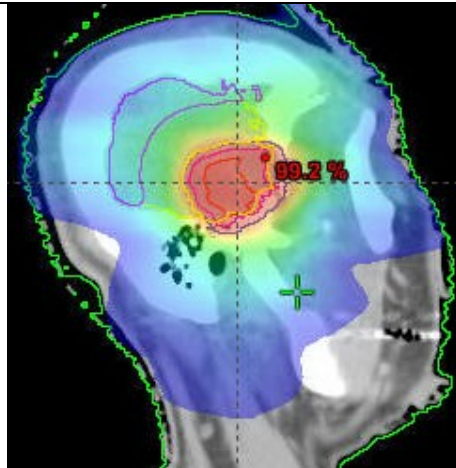


T21322		
T21323		
T21324		

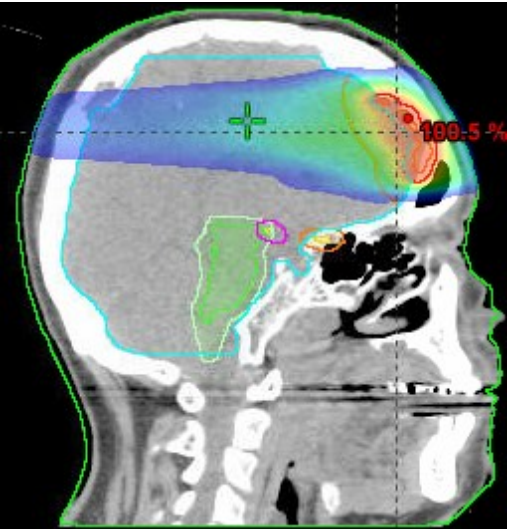
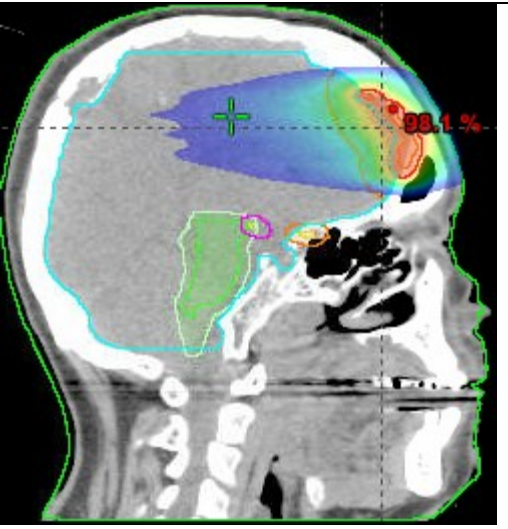
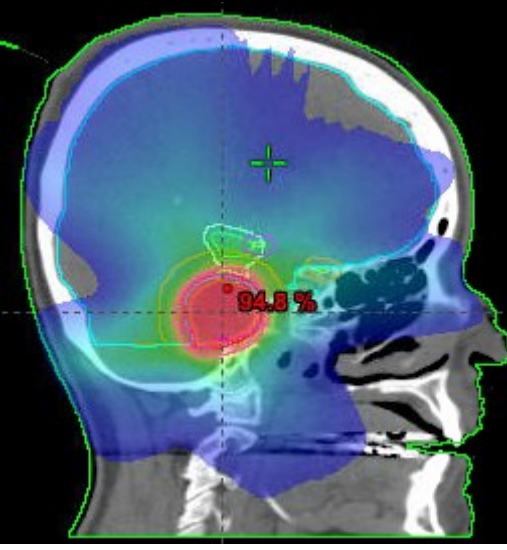
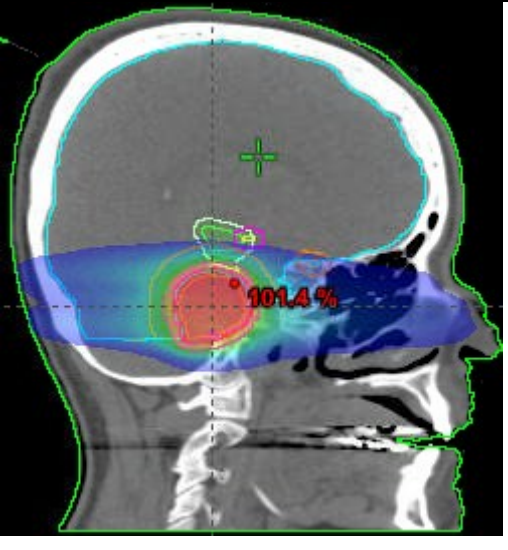
T21325

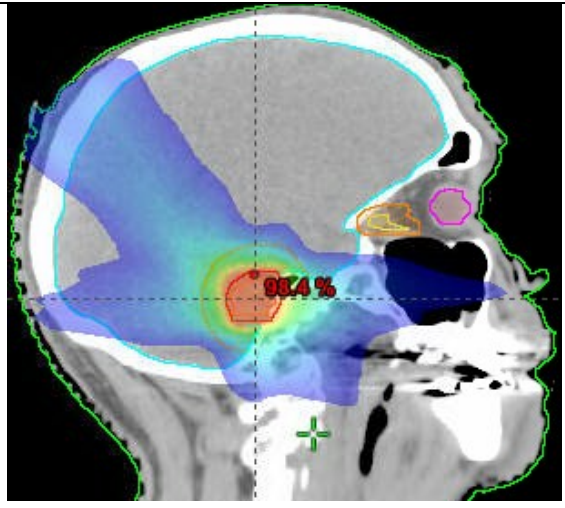
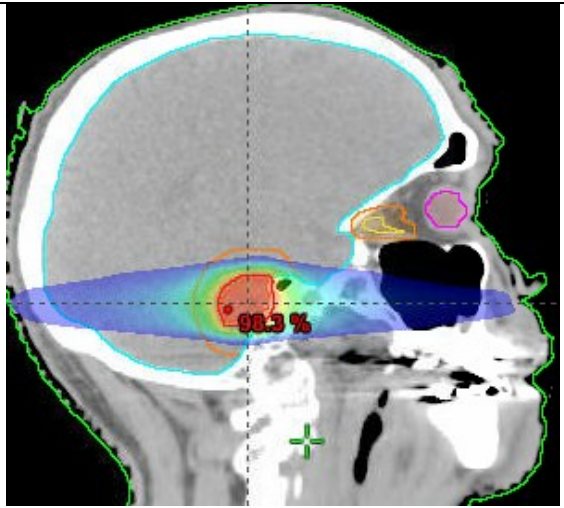
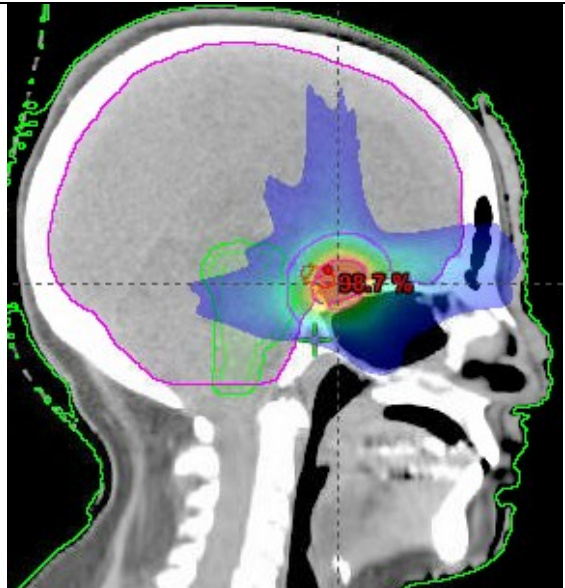
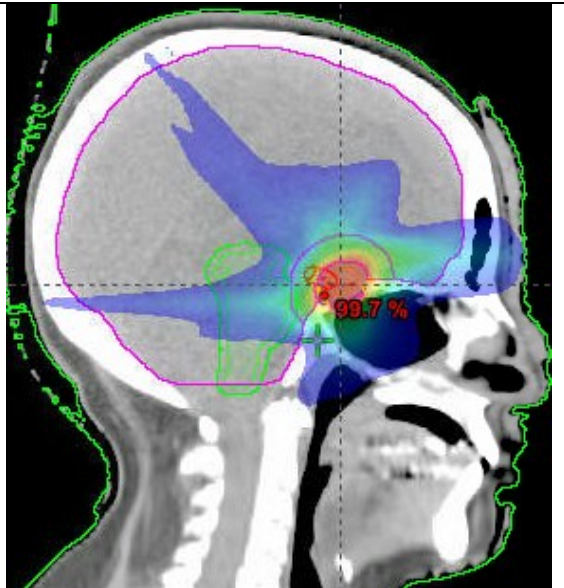
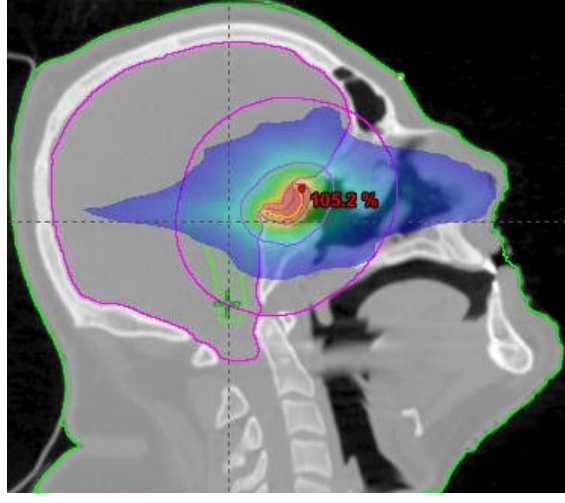
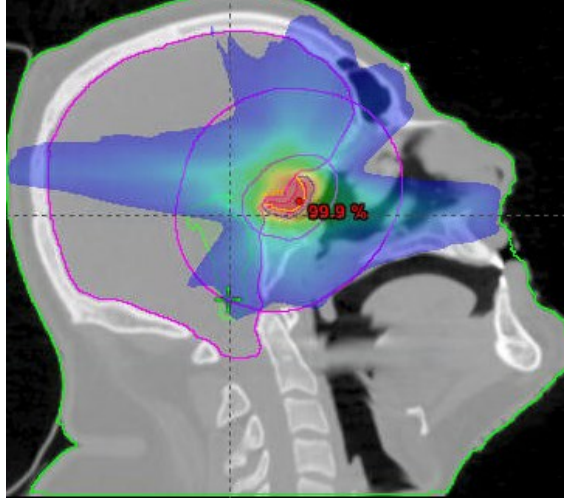


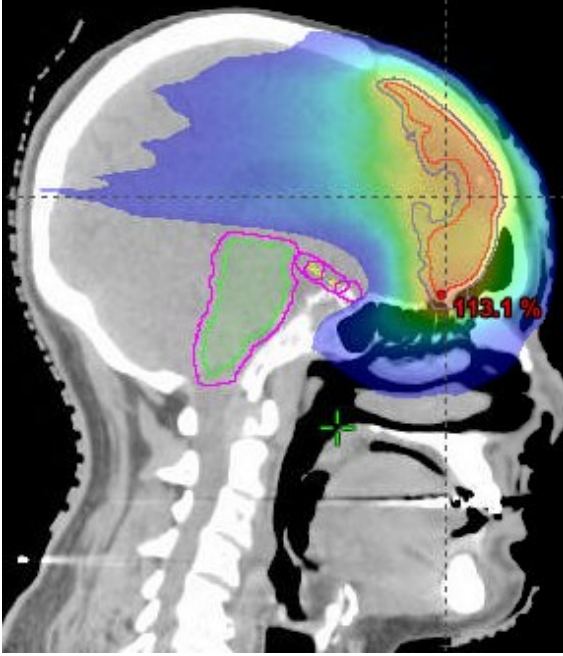
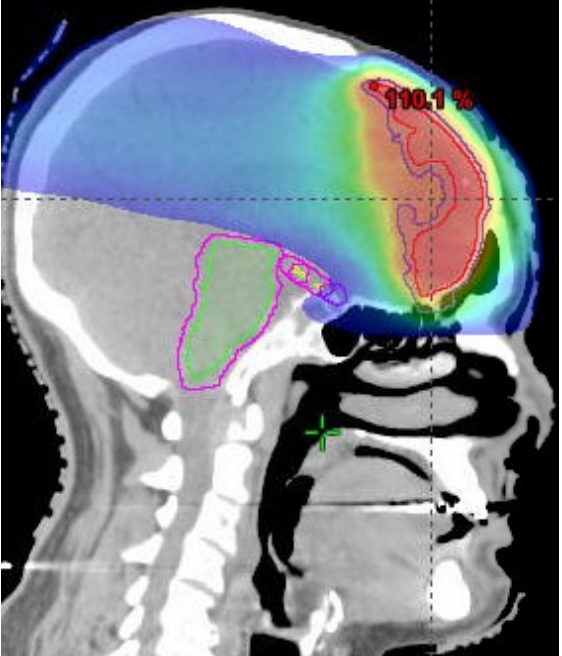
T21326



T21327		
T21328		
T21329		

T21330		
T21331		

T21332		
T21333		
T21334		

T21335		
T21336	